TR-O-0074

45

非線形ダイナミックスを利用した新機能素子の研究

會田　田人

1994. 4. 15

ATR光電波通信研究所

Novel Functional Devices using Nonlinear Dynamics

非線形ダイナミックスを利用した新機能素子の研究

Tahito Aida

會田　田人

Contents

Chapter I

General Introduction

Theoretical and experimental studies on nonlinear delayed feedback (DF) systems such as nonlinear optical cavities have shown the existence of a large variety of multistable bifurcated oscillation modes leading to chaos [1]-[4]. Ikeda *et al.* [5] clarified the hierarchical tree structure of the bifurcation of the oscillation modes excited in a nonlinear optical ring cavity and suggested the applicability of the multistable modes for data storage.

Following up this suggestion, Davis *et.al.* theoretically proposed that selective excitation of the multistable modes, useful for optical signal generation and memory, is possible by two complementary methods. The one is seeded bifurcation (SB) switch [6] and the other chaotic search/switch (CS) [7]. The SB switch is a direct, deterministic selection of a mode by injecting a seed signal. The CS is an approach to selection of mode using chaotic mode transitions, which is complementary to the SB switch and results in stochastic selection of a mode which satisfies a given constraint. These proposals have for the first time given the concrete images for making use of chaos and physical experiments for the proposals have been expected to test the feasibility.

This report mainly summarizes the experimental works done by T. Aida and P. Davis from 1988 to 1993 in ATR to test the feasibility of the functions proposed. The success of the experiments is owing mainly to the good performance of the electro-optical hybrid DF system, which has much larger delays, and thus more modes, and better controllability of system parameters than previous systems.

In Chapter II, we first describe the design of the DF system for the experiments, in particular the reason why we employed the combination of infrared (1.3μm) optical communication components and waveguide modulator, and discuss the typical stability of the bifurcated higher-harmonic oscillations of a non-ideal DF system with large delay. We then describe the experiments of SB switch, in which the feasibility of memory function using multistable nonlinear oscillation modes is confirmed [8].

In Chapter III, we propose a new configuration of an optical loop memory using multistable nonlinear oscillation modes, and demonstrates the basic functions for memory, 'write' and 'erase', using optical pulse sequences in an electro-optical nonlinear ring resonator[9].

In Chapter IV, we demonstrates the CS experiments, in which the effectiveness of making use of chaotic mode transitions for searching and switching among a large number of multistable modes is confirmed. The coding of multistable and chaotic oscillation modes and the quantitative characterization of chaotic mode transitions are also described, related to the CS experiments [10][11][12].

In Chapter V, we describe a digital electronic system, designed for a real-time simulator for systematic study of dynamics of nonlinear DF systems, and to test the applicability of such a digital electronic system itself as a signal generator [13].

References

[1] K.Ikeda, "Multiple-valued stationary state and its instability of the transmitted light by a ring cavity system," Opt. Commun., vol.30, pp.257-261, Aug. 1979.

[2] K.Ikeda and K.Kondo, "Successive higher-harmonic bifurcations in systems with delayed feedback," Phys. Rev. Lett. vol.49, pp.1467-1470, Nov. 1982.

[3] H.M.Gibbs, Optical Bistability : Controlling Light with Light, Orlando, Academic Press Inc., 1985, pp.257-280

[4] Réal Vallée and C. Delisle, "Mode description of the dynamical evolution of an acousto-optic bistable device," IEEE J. Quantum Electron., vol.QE-21, pp.1423-1428, Sept. 1985

[5] K.Ikeda and K.Matsumoto, "High-dimensional chaotic behavior in systems with time-delayed feedback," Physica 29D, pp.223-235, 1987.

[6] P.Davis and K.Ikeda, "Switching between multistable oscillations and applications in signal generator and memory," Technical Digest of the 16th International Conference on Quantum Electronics, ThC-3, pp.634-635, Tokyo, Jul. 1988

[7] P.Davis, "Application of Optical Chaos to Temporal Pattern Search in a Nonlinear Optical Resonator," Jap. J. Appl. Phys. vol.29, pp.L1238-L1240, Jul. 1990.

[8] T.Aida and P.Davis, "Oscillation modes of laser diode pumped hybrid bistable system with large delay and application to dynamical memory," IEEE J. Quantum Electron., vol.28, pp.686-699, 1992.

[9] T.Aida and P.Davis, "Storage of optical pulse data sequences in loop memory using multistable oscillations," Electron. Lett., vol.27, pp.1544-1546, 1991.

[10] T.Aida and P.Davis, "Applicability of bifurcation to chaos : Experimental demonstration of methods for switching among multistable modes in a nonlinear resonator," OSA Proc. on Nonlinear Dynamics in Optical Systems, N.B.Abraham, E.M.Garmire and P.Mandel,eds., vol.7, pp.540-544, 1991.

[11] T.Aida and P.Davis, "Adaptive mode selection using chaotic mode transitions in a nonlinear optical resonator," Conf. Laser and Electro-Optics, Baltimore, MD, May 1993, paper CWJ59, p.332

[12] T.Aida and P.Davis, "Oscillation mode selection using bifurcation of chaotic mode transitions in a nonlinear ring resonator," submitted to IEEE J. Quantum Electron.

[13] T.Aida, N.Otani and P.Davis, "Digital Implementation of a Nonlinear Delayed-Feedback System," to be published in IEEE Trans. Circuits Syst., vol. CAS-41, Mar. 1994

Chapter II

Oscillation Modes of Laser Diode Pumped Hybrid Bistable System with Large Delay and Application to Dynamical Memory

Abstract

An electro-optical bistable system with a very large delay was constructed of state of the art optical communication components and the self-oscillation phenomena of the system were investigated from the point of view of application as dynamical memory. Very large numbers of multistable self-oscillation modes were observed, including 2nd order bifurcations of the 265th harmonic. The dynamical memory function was demonstrated by locking 2nd order bifurcated modes to external clock oscillations and performing WRITE and READ of binary data sequences in the waveforms of the bifurcated modes. From the dynamical stability of the oscillations used for memory, and of the mode switching, it was concluded that the nonlinear bifurcation phenomena in this system are applicable for large capacity memory and signal processing. Spurious preferential excitation of particular harmonic modes that occurred in the system was related to the fine structure in the transfer spectrum of the open loop associated with spurious resonances in the electro-optical (E-O) modulator used as nonlinear element. It was demonstrated that missing harmonics could be recovered by pumping with small sinusoidal signals of the corresponding frequencies.

1 Introduction

Since the delay-induced oscillation and instability in the delayed feedback (DF) system predicted by Ikeda[1][2] was for the first time experimentally confirmed in an electro-optic hybrid bistable device with computer delay[3], theoretical and experimental investigations of oscillation modes and their stability have been made with various DF system implementations [2]-[14]. The nature of the oscillation leading to chaos has been investigated in numerical simulations, and also in experiments in DF systems with small delay [8][9] and DF systems with large delay [2][3].

The main difference between the cases of large delay and small delay is the variety of the modes of oscillation. For a large effective delay, where the delay time is much larger than the response time, there is a fundamental oscillation mode which exhibits period-doubling bifurcation and there are also multiple harmonic oscillation modes each of which exhibits a sequence of bifurcations leading to chaos [2][13][14]. On the other hand, for a small effective delay, where the delay time is comparable to the response time, neither harmonic oscillations nor clear period-doubling bifurcation of the fundamental are observed before reaching the chaotic regime [8][9].

Ikeda *et al.* have clarified the bifurcation structure of oscillation modes of a DF system and suggested potential applicability as a memory device, utilizing the multi-stable modes of oscillation [14]. Following up this suggestion, Davis *et al.* proposed a method called Seeded Bifurcation (SB) switch for selective excitation of oscillation modes corresponding to binary coded input data, which could be used to realize a versatile digitally controlled optical signal generator or a memory device [15][16].

We have constructed an electro-optical (E-O) hybrid DF system, in which very large effective delays of up to about 520 are possible, using state of the art components for optical communication [17]. This system has much larger delay, and thus more modes, and better controllability of system parameters than previous systems[3][7]-[9][12].

Selective excitation of modes in a DF system by the SB switch method not only makes possible a memory function but also allows more systematic investigation of modes and their stability than was previously possible. There is still no rigorous theory for the existence of the many bifurcated harmonic modes that have been

found in numerical and physical experiments, and there is still much to be understood about their stability. Previous experiments have shown that spurious small nonlinearities in the system can significantly affect the stability of multistable modes [7]. In our experiments, in addition to the experimental demonstrations of the SB switch and the memory application, we have investigated the typical stability of the bifurcated higher-harmonic oscillations of a non-ideal DF system with large delay.

In section II we first review the principles of the dynamical memory, including coding of multistable oscillation modes, method of the SB switch and capacity of the memory. We then in section III discuss the design of the DF system, in particular the reason why we employed the combination of infrared (1.3μm) optical communication components and waveguide modulator. We present in section IV a quantitative characterization of the DF system, specifically the open and closed loop characteristics. In section V we present the test of the application to memory function. In section VI we discuss discrepancies in oscillation phenomena of the DF system from the ideal model. Finally we summarize this paper and discuss the prospects of high-speed, all-optical operation of the dynamical memory.

2 Principle of dynamical memory

In this section we briefly review the principle of the dynamical memory [16]. The important points are the method to utilize multistable oscillation modes for memory states with binary coding and the method to select a mode corresponding to a particular binary code.

2.1 Coding of multistable oscillations

Oscillations with multistable modes applicable to dynamical memory are seen in many systems with delayed nonlinear feedback. The dynamics of such a system are described by the following class of delay-differential equations [13].

$$T_m \frac{dx(t)}{dt} = -x(t) + f(x(t - T_r); \mu), \tag{1}$$

where μ is the bifurcation parameter, and T_m and T_r are the response time and the delay time of the nonlinear feedback, respectively. The function f has a nonlinearity with at least one maximum or minimum to show period-doubling, as μ is increased.

For an optical cavity with a dispersive medium, a typical model of the system, $f(x;\mu)$ takes the following form,

$$f(x;\mu) = \mu(1 + 2Bcos(x - x_o)), \tag{2}$$

where μ is proportional to the incident optical power, and dissipation $B(< 1)$ and bias x_o are constant [13].

Classes of oscillation modes excited in a system described by equations (1) and (2) can be classified with harmonic number n and bifurcation order m [14]-[16]. For bifurcated harmonics $(n > 1, m > 1)$ there are multiple oscillation modes in the (n, m) class, "isomers", with different peak modulation patterns[1]. The dynamical memory described in this paper utilizes a set of isomers of $(n, m = 2)$ class oscillation as memory states.

Figure 1 shows an example of $(n = 7, m = 2)$ mode and its coding. In each T_r interval there are n sub-intervals, where the signal varies slowly, i.e. $T_m \frac{dx(t)}{dt} \approx 0$. It follows from equation (1) that the signals in sub-intervals separated by T_r are approximately related by the following recurrence relation reduced from equation (1)

$$x(t) \simeq f(x(t - T_r); \mu). \tag{3}$$

Such recurrence relations are known to exhibit period-doubling bifurcation [19]. After the m-th period-doubling bifurcation, the signal in each sub-interval, a peak or valley of the oscillation, takes on one of 2^m levels, that is 2^{m-1} peak levels and 2^{m-1} valley levels. Different oscillation modes have different sequences of levels, that is different peak and valley modulation patterns.

The recurrence relation between $x(t)$ and $x(t - T_r)$ can be expressed by a diagram in figure 2(a) for the case of second order (m=2) bifurcation [19]. There are four peak and valley levels in $m = 2$ bifurcated oscillation. We assign 2-bit labels, I_i = 00,01,10, or 11, to the peak and valley levels, where i is an integer indicating a time interval. Then the waveform can be represented by a sequence of I_i, $(\cdots, I_{i-1}, I_i, I_{i+1}, \cdots)$. Now, I_{i+n} is determined by I_i in accordance with equation (3). Therefore, we can completely identify an isomer of the $(n, m = 2)$ class oscillation with an n-element code $\boldsymbol{I} = (I_1, I_2, \cdots, I_n)$ representing the signal levels in a T_r

[1]Let us briefly explain the correspondence between the (n, m) notation and the notation used by Vallée *et al.*[18]. They describe "periodic waveforms" and "frequency locked waveforms" labeled by ${}^qP2^m$ and ${}^q_jL2^m$, respectively. These modes correspond to different isomers in the (n, m) class where $q = (n + 1)/2$.

interval. The peak and valley levels separated in interval T_r appear in the cyclic sequence determined by equation (3), $\cdots, 01, 10, 00, 11, 01, 10, 00, \cdots$, and repeat with period $4T_r$, as seen in figure 2(b).

We can also completely identify a $(n, m = 2)$ waveform by assigning 1-bit binary labels $J_i = 0$ or 1 to the peak levels in a $2T_r$ interval. There are n peak levels in a $2T_r$ interval, and the oscillation is coded by an n-element peak code

$$\boldsymbol{J} = (J_1, J_2, \cdots, J_n), \tag{4}$$

This peak code $\boldsymbol{J}$ can be easily read by thresholding the output signal. The peak levels in a T_r interval are related to the valley levels in the former T_r interval by equation (3), as shown in figure 1. The relation between $\boldsymbol{I}$ and $\boldsymbol{J}$ is summarized by the following equations.

For the elements of $\boldsymbol{I}$ indicating peak levels,

$$I_{2i-1} = 1 \; J_i \quad \text{when} \quad 2i - 1 \leq n, \tag{5}$$

for $i = 1, 2, 3, \cdots, n$. Where the second bit (the left bit) "1" means peak level.

For the elements of $\boldsymbol{I}$ indicating valley levels,

$$I_{2i-n-1} = 0 \; (1 - J_i) \quad \text{when} \quad 2i - 1 > n, \tag{6}$$

for $i = 1, 2, 3, \cdots, n$. Where the second bit (the left bit) "0" means valley level.

As is clear from the cyclic sequence of the first bit (the right bit) of I_i, the $\boldsymbol{J}$ code is followed by the inverted $\boldsymbol{J}$ code in the next $2T_r$ interval. With an external reference clock to identify the phase of the oscillation we can distinguish 2^n isomers in an $(n, m = 2)$ class. That is, with an external reference clock to distinguish bit patterns which would otherwise be identical under a translation in time, the number of different memory states is 2^n. With no reference clock, the number of distinguishable $(n, m = 2)$ modes is reduced, but at least $2^{n-1}/n$. For example in the case of the $(n = 3, m = 2)$ class, without identification of the phase of the oscillation, there are only two distinguishable isomers in the class - the two modes shown in figures 2(d) and (e). We can assign six different $\boldsymbol{J}$ codes to the first isomer, $(1, 1, 1), (1, 1, 0), (1, 0, 0), (0, 0, 0), (0, 0, 1)$, and $(0, 1, 1)$, and two codes to the second isomer, $(1, 0, 1)$ and $(0, 1, 0)$.

2.2 Writing

Writing information into the oscillation waveform is done by a selective excitation of the isomer of the $(n, m = 2)$ class corresponding to input binary data. In this paper, the WRITE is done by switching from a stationary state at $\mu = \mu_{off}$ to an $(n, m = 2)$ oscillation state at $\mu = \mu_{on}$ while injecting a seed signal, of length T_r, corresponding to the desired oscillation waveform. This is a type of seeded bifurcation (SB) switch [16]. We introduce a seed code $\boldsymbol{S}$ for the seed signal. The seed determines the peak and the valley levels in a T_r interval of the target oscillation, so the seed code

$$\boldsymbol{S} = (S_1, S_2, \cdots, S_n), \tag{7}$$

where S_i is a 2-bit binary label, just corresponds to the $\boldsymbol{I}$ code of the target oscillation.

If the input data is given in the form of $\boldsymbol{J}$ code, it is necessary to convert $\boldsymbol{J}$ to the seed code $\boldsymbol{S}$. The conversion from $\boldsymbol{J}$ to $\boldsymbol{S}$ is done using equations (5) and (6). Figure 3 shows a schematic example of the SB switch of $(n = 7, m = 2)$ class with the codes $\boldsymbol{S}$, $\boldsymbol{J}$ and $\boldsymbol{I}$, in which we can see the relations between the codes.

3 Design of a delayed feedback system with very large delay

The two main requirements of a DF system to be used in a dynamical memory experiment are the following.

One is stability of a large variety of multiple bifurcated high harmonic oscillation modes excited in the DF system. In particular we require stability of $(n, m = 2)$ class oscillations with large n. This is for large capacity memory. The other requirement is controllability of parameters for changing the feedback gain and injecting signals into the DF system loop. This is to facilitate control of the selective excitation of the modes using the seeded bifurcation method, the SB switch. A DF system satisfying the above requirements should have the following characteristics.

The DF system should have a large effective delay. The bit capacity of the system increases with harmonic number n. Higher harmonics can be excited by increasing the effective delay T_r/T_m. A large effective delay can be achieved by employing a long delay line and fast response components.

The frequency characteristic of the DF system should have a wide bandwidth. A class $(n, m = 2)$ oscillation has a principal frequency component (carrier frequency) of $n/(2T_r)$. A modulation frequency of $n/(4T_r)$ is required to distinguish neighboring "1" and "0" peaks. Thus, the frequency band spread at least $\pm n/(4T_r)$ around $n/(2T_r)$ is necessary to support all the isomers of $(n, m = 2)$ class oscillation. Moreover, the frequency characteristic should be smooth in this band to obtain comparable stability for the different isomers which have different peak modulation patterns and thus different frequency components.

The DF system should be designed so that the bifurcation giving rise to the $(n, m = 2)$ oscillations to be used as memory states, is achieved at low input optical power. Input power, of the order of milliwatts, is desirable for control of the SB switch with a laser diode (LD) pump. In addition, the range of bifurcation parameter μ, where μ is proportional to the input optical power, should be wide enough for the oscillations to be stable with respect to input power and loop gain fluctuations.

In the DF system, the range of parameter μ supporting higher order bifurcations decreases with increase of bifurcation order m only at a rate of order of the Feigenbaum constant, $\delta_\infty \approx 4.67$ [20], which is less than an order of magnitude. With this scaling factor stability of μ parameter to support $m = 2$ bifurcation seems to be achievable in a practical system. According to Vallée's estimation with a stochastic-difference equation and experimental results for an A-O hybrid system, the third order (m=3) bifurcation is obscured by multiplicative noise of order of 10^{-2} and additive noise of order of 10^{-3} [12]. So, the signal to noise ratio of the system should be more than 20dB to support $m = 2$ bifurcation. This must be balanced with the other requirement of a wide bandwidth, as a wider bandwidth in practice means a higher noise level.

Given the above design considerations, at present, a hybrid DF system seems to be a better choice than an all optic DF system. In order to observe the period-doubling bifurcation in an all-optic resonator, a nonlinear phase shift of more than π within a round trip is demanded [1]. The main problem with an all-optic system is that there is a lack of material with high dispersive nonlinearity and need of high input optical power, i.e. YAG or CO_2 lasers, to obtain the required phase shift [21]-[23].

The hybrid DF system which we employed is an E-O hybrid ring resonator, essen-

tially consisting of a laser diode (LD), an E-O intensity modulator with waveguide Mach-Zehnder (MZ) structure, a single mode optical fiber delay line and high-speed video amplifiers as shown figure 4. Optical components of the E-O hybrid resonator are components for optical communication at 1.3μm wavelength. The configuration is described in more detail in Appendix I.

In the E-O hybrid DF system, the nonlinearity is due to the sinusoidal modulation characteristic of the electro-optical (E-O) modulator. The half-wave voltage of the modulator corresponds to the voltage causing the π-shift of phase in the optical signal in one arm of the M-Z structure inside the modulator. In order to observe the period-doubling bifurcation in the E-O hybrid DF system, a voltage swing of more than the half-wave voltage is required. This condition is described as

$$P_i L_m (1 - \frac{1}{E_r}) L_o R Z_i A_e \geq V_\pi, \tag{8}$$

where V_π is the half-wave voltage of the E-O modulator. P_i is the input optical power. L_m is the insertion loss of the E-O modulator. E_r is the extinction ratio of the E-O modulation. L_o is the propagation loss in FC-connectors and optical fiber. R is the photosensitivity of the PIN diode. Z_i is the input impedance of the first stage amplifier. A_e is the total electric voltage gain. The components of the E-O hybrid system were chosen so as to satisfy this condition and also satisfy the requirements mentioned earlier, namely, large effective delay, wide bandwidth, low input optical power, and controllability for the SB switch. The half-wave voltage of a waveguide E-O modulator is typically 6V, while that of a bulk E-O modulator is about ten times larger. The power of the optical input to a waveguide modulator is limited by the optical damage threshold, which is typically about 10mW for infrared light, while only 0.01mW for 0.63μm (He-Ne laser) light. At the 1.3μm wavelength, optical fiber with negligibly small propagation loss can be used as a delay line. This use of a waveguide modulator and 1.3μm wavelength infrared light, allows a combination of long optical delay line and electrical amplifiers with lower gain and thus faster response, resulting in very large value of effective delay compared to previous experimental works. Specifically, effective delay up to 520 has been realized, with T_r equal to 5.2μsec in a 1km delay line, and T_m equal to about 10nsec. This is an order of magnitude larger than the effective delay in previous experiments [6]-[12]. The effective delay was varied by introducing an electrical low pass filter (LPF).

Moreover, the choice of optical components allows a laser diode (LD) to be employed for the light source. With this configuration, the order of the input optical power P_i from the LD required to cause the period-doubling bifurcation is estimated as follows. The values substituted into equation (8) are $V_\pi = 6$V, $L_m = 0.355$ ($\equiv -4.5$dB), $E_r = 100$ ($\equiv 20$dB) as typical extinction ratio or $E_r = 3.16$ ($\equiv 5$dB) as degraded extinction ratio, $L_o = 0.708$ ($\equiv -1.5$dB), $R = 0.87$A/W, $Z_i = 50\Omega$, and $A_e = 708$ ($\equiv 57$dB). With these values $P_i \geq 0.784 \times 10^{-3}$ for E_r estimated at 20dB or $P_i \geq 1.135 \times 10^{-3}$ for E_r estimated at 5dB are obtained. Therefore, the period-doubling bifurcation is expected to occur around the input optical power of 1mW, which can be achievable with LD power. The LD can be directly and rapidly modulated, resulting in easy and quick control of the system gain parameter to facilitate the SB switch.

4 Experimental results: Observations on oscillation behavior

In this section we describe the open and closed loop characteristics of the DF system. By measuring the open loop characteristics we could confirm that the operation of the DF system is roughly consistent with the theoretical model and obtain the values of the system parameters. The main concern in checking the closed loop behavior confirmation of the stability of the oscillation modes to be used for memory states.

4.1 Open loop characteristics

The open loop characteristics of the DF system were measured by opening the loop at port (c), driving the E-O modulator with an external voltage V_i and measuring the feedback voltage V. It was confirmed that the behavior was roughly consistent with the following model equation,

$$T_m \frac{dV(t)}{dt} = -V(t) + V_o + \mu F(V_i(t - T_r)), \tag{9}$$

where V_o is an accumulated offset bias voltage measured at the port (c), F is the E-O modulation characteristic of the E-O modulator, and μ is the effective feedback loop gain. μ is proportional to the input optical power P_i from the LD, and is given by

$$\mu = P_i L_m L_o R Z_i A_e. \tag{10}$$

The parameters T_m, T_r and function F were measured, based on the equation (9). By driving voltage V_i at the E-O modulator with a rectangular wave, parameters T_r and T_m, respectively, were obtained as delay time and decay time of the V signal. T_r was 5.2μsec. T_m was 6nsec without the LPF and could be increased for example to 10nsec, 42nsec, $\cdots$, by adjusting the LPF. F was determined as the relation between V and V_i, when V_i was modulated by a slowly-varying triangular wave with constant input optical power P_i. Figure 5 shows the measured F curve, which shows some discrepancy from the ideal sinusoidal curve. This discrepancy is due mainly to the low extinction ratio of the input light from the LD.

The frequency characteristic of the open loop gain was obtained as the transfer spectrum $|G(\omega)|$ for constant input optical power P_i. Transfer spectra for the system with and without low pass filter (LPF) are shown in figure 6. The frequency characteristic without the LPF was flat as shown in figure 6(a) with a slight peak before falling off above 70MHz, a characteristic of the wide bandwidth amplifiers. After introduction of the LPF the transfer spectrum decreased monotonically with frequency as shown in figures 6(b)-(d). This is roughly consistent with the relaxation characteristic expected in a system described by equation (9).

The large signal open loop behavior was investigated by driving the E-O modulator with V_i of large amplitude rectangular wave of frequency ranging from 50KHz to more than 1MHz. Typically, the output, $V(t)$, was also rectangular. However, when harmonics coincided with certain frequencies (e.g.,$\cdots$, 1.12MHz, 2.537MHz,$\cdots$), small ripples with those frequencies were observed to appear on $V(t)$ as shown in figure 7. This behavior is not expected from the model. The ripples could be observed in the modulated optical output of the E-O modulator. Many small abrupt changes of about 1dB have been observed in the transfer spectrum of the open loop gain as shown in figures 6(a)-(d), and some of the frequencies where these occur have been confirmed to coincide with the ripple frequencies. We think that this phenomenon might result from spurious resonance of the E-O modulator due to piezo-electric vibration of the $LiNbO_3$ substrate [24]. So there appears to be another mechanism in the system in addition to equation (9). Although this spurious property of the E-O modulator may not significantly impair performance in its conventional use for high-speed digital modulation, it can significantly affect low-frequency modulation and, as explained below, this turns out to have a non-trivial

influence on the closed loop behavior of the nonlinear resonator.

4.2 Closed loop characteristics

For the closed loop configuration we replace $V_i(t-T_r)$ for the open loop with $V(t-T_r)$. Therefore, figure 5 can be regarded to be a recurrence relation between signals $V(t)$ and $V(t-T_r)$ separated in time by the interval of time T_r required by the signal to propagate through the feedback loop. The closed loop characteristic of the DF system is modeled by the following delay differential equation,

$$T_m \frac{dV(t)}{dt} = -V(t) + V_o + \mu F(V(t-T_r)). \tag{11}$$

This can be rewritten in the form of equation (1) with x replaced by V.

Figure 8 shows the closed loop resonance characteristic for effective delay $T_r/T_m \approx 124$ obtained at a point just before the onset of self-oscillation. This was obtained using a network analyzer to measure a small signal transfer spectrum between the port (b) for signal injection and the port (a) for signal detection. The resonance peaks appear at about 95.3KHz and its odd harmonic frequencies, and the peak heights of the spectrum decrease with increase of frequency. This is consistent with the results of the linear stability analysis (see Appendix II), which gives the frequencies of small amplitude oscillations as

$$f_n \simeq \frac{n}{2T_r}(1 - \frac{T_m}{T_r}). \tag{12}$$

where n is an odd integer.

We confirmed that equation (12) derived for small amplitude oscillations also gave the principal frequency components of the large amplitude oscillations when $T_m \ll T_r$. Figure 9 shows the good agreement between the frequencies of the fundamental mode f_1 for values of T_r/T_m ranging from 18 to 520 and the values given by equation (12).

With increase in μ, the oscillation modes exhibit a sequence of bifurcations, leading to chaos. Figure 10 shows the waveform of an (n,m)=(1,2) oscillation for $T_r/T_m \approx$124. The stable peak and valley levels of the n=1 oscillation for m=0,1,2 over a range of the input optical power P_i are seen as a bifurcation diagram in figure 11. As explained in section II, these stable peak and valley levels are understood from the recurrence relation between signal levels separated in time by T_r

$$V(t) \simeq V_o + \mu F(V(t-T_r)). \tag{13}$$

The m=2 order bifurcation occurs at the input optical power P_i of about 0.87mW, which is roughly consistent with the value of 1mW estimated in section III. For $T_r/T_m \approx$124 bifurcated harmonic modes up to m=2 and n=21 were observed to stably oscillate. Stable (265,2) mode oscillations were observed as the highest stable bifurcated harmonic mode when $T_r/T_m \approx$520. Figures 12(a) and (b), respectively, show an example of waveform and spectrum of one of the (265,2) modes. From these experimental results we confirmed that a huge variety of multiple stable modes sufficient for the dynamical memory experiment can be excited in the DF system by the LD power.

A preference in the excitation of harmonics was exhibited by the system. Though modes with large harmonic number were observed, not all the intermediate values of odd n were observed, as would be expected on the basis of numerical experiments [13]. For example in our experimental setup with $T_r/T_m \approx 124$, only the modes with n=1 and n=21 could be spontaneously excited by just increasing input optical power P_i. This phenomenon will be discussed in more detail later in section VI.

It can be seen from figure 11 that the range of input power corresponding to $(1,2)$ oscillation is about 0.04mW. The parameter range for the existence of the m-th order bifurcated mode decreases as m increases. For a one dimensional map such as equation (3) [19], where μ_m denotes the μ values for the m-th order bifurcation point, the Feigenbaum scaling factor [20] has been defined as

$$\delta_m = \frac{\mu_m - \mu_{m-1}}{\mu_{m+1} - \mu_m}. \tag{14}$$

We defined μ_m for the n-th harmonic as the minimum value of input power where the (n,m) mode was stable. Figures 13 (a) and (b) respectively show bifurcation diagrams for the n=1 and n=21 modes. From the diagrams we found $\delta_2 \approx$3.3 for n=1 and $\delta_2 \approx$2.3 for n=21. These values are of the same order as those estimated by Vallée *et al.* for a system with A-O modulator, δ_2=4.5 for n=1 and δ_2=5.2 for n=3 [12].

As seen in the bifurcation diagram in figures 13 (a) and (b), bifurcations for $m \geq 3$ were indistinct. Higher order bifurcations are expected to be obscured by noise if noise levels exceed certain values [25]. In our system dominant noise sources were the LD noise, shot noise of the PIN diode and noise of the first stage video amplifier. Of these the LD noise was the major noise source. For 1mW input optical power, the ratio of the total noise to the input optical power was about -18.5dB ($\equiv 1.4 \times 10^{-2}$).

This noise behaved as a multiplicative noise for the system. In our experiment, bifurcations up to second order were stable but the third order bifurcation could not been seen with this noise level. Our result was consistent with Vallée's result for multiplicative noise [26].

Though the noise ratio in our system could have been improved by using an LD with an optical isolator, it was sufficient for the demonstration of the dynamical memory function that the m=2 oscillation modes were stable.

5 Experiments on dynamical memory

Having confirmed the stability of the $m = 2$ modes, we next examined the feasibility of using these modes as memory states. First, we demonstrated that frequency-locking of the (21,2) oscillations could be done to obtain phase stability. We then executed writing and reading of 21-bit binary data sequences based on the scheme described in section II. Figure 16 shows two examples of writing 21-bit binary data to a (21,2) mode, and figure 18 shows an example of reading.

5.1 Locking

The appearance of resonance and frequency-locking phenomena in a DF system as the result of input modulation has been previously reported [27][28]. For the purpose of the dynamical memory function we checked that bifurcated modes could be locked to external oscillations. We confirmed that the phase of an $(n, m = 2)$ mode could be locked to that of an external reference clock by weakly modulating the LD with a sinusoidal signal at a frequency near $n/(2T_\tau)$, the carrier frequency of the free-running $(n, m = 2)$ mode oscillation. Figure 14 shows frequency locking curves for (7,2) and (21,2) modes with the modulation depth of 0.4%. The locking ranges increase roughly in proportion to the modulation depth as shown in figure 15. Different isomers were found to have comparable locking ranges.

5.2 Writing

The WRITE procedure is a selective excitation of the $(n, m = 2)$ mode corresponding to an input n-bit binary word in the form J code. The WRITE is done by the SB switch described in section II. Parameter μ is changed by increasing input optical

power (LD power). The seed signal is injected by modulation of bias voltage V_o.

It was necessary to determine two voltage levels, corresponding to μ_{off} and μ_{on}, to be used in driving the LD. It was also necessary to determine four voltage levels of the V_o seed signal corresponding to the four levels of the stable oscillation waveform at μ_{on}.

The SB switch signals were generated in the following manner. Input data in the form of $\boldsymbol{J}$ code was converted to $\boldsymbol{S}$ code according to the equations (5) and (6). Then the $\boldsymbol{S}$ code sequence was converted to a V_o seed signal of length T_r. The AFG generated the signals for the modulation of V_o and the LD. A personal computer (PC) automatically controlled execution of the sequence of data conversion and input signal generation so that a 21-bit data sequence keyed in from the PC keyboard was written into the memory.

Figure 16 shows two examples of 21-bit data WRITE. The change of input optical power P_i corresponds to change of μ from μ_{off} to μ_{on}. The pattern of the seed signal V_o determines the (21,2) mode which is excited. It can be seen that the stable asymptotic oscillation is similar to the initially excited oscillation, in which 21 bits of binary data are encoded.

In general, in the presence of noise, the shape of the seed signal injected into the loop should be as close as possible to that of the waveform of the desired oscillation mode. However, a degree of tolerance in the seed signal is possible due to the dynamical stability of the oscillation modes. In our system we found tolerance of more than $\pm 50\%$ in the difference of the two peak(or valley) levels and about $\pm 50\%$ of T_r/n in length of the seed signal. Figure 17 shows an example of writing, when the shape of the seed signal had discrepancies of -30% in peak levels and +30% in valley levels. Due to the dynamical stability of the mode, the input data was not lost, although there was a long transient before the signal settled to the asymptotic waveform. Too critical setting of the shape of seed signal results in long switching times.

As shown in figure 12 stable harmonic $(n, m = 2)$ modes up to n=265 have been observed in this system when $T_r/T_m \approx 520$. However, our experimental setup for injecting seed signal at present cannot handle seed signals for n=265. The writing of data into the dynamical memory with bit capacity of 265 bits remains a task for the future.

5.3 Reading

The READ operation is done by thresholding peak levels of the oscillation at the output detector (DET in figure 4). Figure 18 shows an example of reading 21-bit binary data from a (21,2) mode oscillation locked to an external reference clock. The timing pulse Pt, used for identifying the first bit of the cyclic 42-bit pattern (21-bit pattern, followed by the inverted 21-bit pattern), was generated by 1/42 frequency division of the external reference clock.

5.4 Erasing

Erasing of the data is done simply by switching input power from the value corresponding to μ_{on} back to the value for μ_{off}. The value for μ_{off} should be set to be nearly zero for quick decay within the 1-bit time (T_r/n). Figure 19(a) shows an example of erasing of (21,2) mode. With a larger non-zero value of μ_{off}, a transient of a few T_r in length was observed, as shown in figure 19(b). Critical setting of μ_{off} near the bifurcation point of m=1 could cause near-critical slowing down, resulting in long erasing time.

5.5 Stability

It was observed that the modes were most stable when the input optical power was set to an optimum level ranging roughly from midway between the m=2 and m=3 bifurcation points to just below the m=3 bifurcation point. As can be seen from the bifurcation diagrams in figure 13, this requires determination of the input optical power and loop gain with less than about $\pm 2\%$ control error. Appendix III contains a discussion of some control considerations specific to our particular system. Note that, in principle, if the detector threshold level for reading binary data is set midway between levels of peak and valleys originating with m=2 bifurcation, onset of m=3 or higher order bifurcations initially does not significantly affect the stability of the binary data, because they only cause higher order modulations of the waveform.

6 Observations on preferential excitation of harmonics

In this section we discuss a major discrepancy of the system from the model. The model described by the delay-differential equation (11) shows a staircase dependence of stable harmonics on μ [13][14], in the sense that when μ is increased, there are transitions between odd harmonic modes in the sequence 1, 3, $\cdots, n, n+2, \cdots$. However, the behavior of the experimental system differs from the ideal model in regard to the stability of harmonic modes. The staircase was incomplete, with a preference for oscillation at certain harmonics. Figure 20 (a) shows plots of primary oscillation frequency versus μ for $T_r/T_m \approx$124, obtained by sweeping input optical power P_i ($\propto \mu$) up and down. There was a jump directly from n=1 to the high harmonic n=21, and a return directly to n=1 from n=21.

Missing intermediate harmonic oscillations were excited using the SB switch method to systematically investigate their stability. A 7th harmonic branch, n=7, was found by SB switch. All other intermediate harmonic branches were unstable in the sense that stable oscillations could not be found even by SB switches with very careful choice of seed, though n=3 and n=5 oscillations had rather long life-times. Table 1 summarizes the stability of harmonics excited in the resonator for $T_r/T_m \approx 124$. This preferential harmonic excitation could not be understood from the experimentally obtained small signal resonance characteristic in figure 8.

Each missing harmonic could be recovered by pumping into the loop from port (b) a small sinusoidal signal at a frequency near that of the missing harmonic. An example of the recovery of n=11th harmonic is shown in figures 20(b)-(g). Figure 21 shows a corresponding phase diagram of mode excitation drawn in the space of input optical power versus pump intensity. The region where the 11th harmonic appeared to stably oscillate became larger with increase of pump intensity. For the case for $T_r/T_m \approx$124 we confirmed that all missing odd harmonics, and their $m = 2$ bifurcations, for n up to n=27 could be recovered by the pumping.

As described in section IV, small sharp variations of about 1dB were observed in the transfer spectrum of the open loop gain (figures 6(a)-(d)). These seemed to result from spurious resonances, especially piezo-electric vibration of the $LiNbO_3$ substrate, in the E-O modulator [24]. These small variations in the open loop

gain could affect the stability of the oscillation modes, resulting in the preferential harmonic excitation. Derstine *et al.* also observed that stability of harmonic modes was extremely sensitive to spurious nonlinearities in the E-O device [7].

In order to test this hypothesis, we examined the relation between the fine structure of the open loop gain and the strengths of pump signals which were necessary to make the harmonics stable. Figures 22(a) and (b) show the transfer spectrum of the open loop gain expanded around the frequency 25MHz near the 265th harmonic, and threshold pump intensities, respectively, for $T_r/T_m \approx 520$. In this range of frequencies, differences in the the open loop gain could be regarded to result only from the fine structure, because the systematic decrease of the open loop gain with frequency increase originating from the relaxation characteristic was negligible, as seen in figure 6(b). For $T_r/T_m \approx$520, the 265th harmonic was the highest harmonic which could be observed without pump signal, and other harmonics near the 265th harmonic could be made stable with pump signals. The threshold pump intensity, which is necessary to make each harmonic stable, is indicated in figure 22(b). The larger the open loop gain the smaller the threshold pump intensity. These observations seemed to confirm that, for large effective delay, excitation of harmonics was very sensitive to the loop gain and even less than 1dB difference in the loop gain affects the excitation of harmonics in the closed loop.

The delay-induced oscillations in the closed loop have many frequency components, which can couple to spurious resonances in the E-O modulator. Therefore, the existence of complex fine structure in the open loop transfer spectrum might correspond to promotion or suppression of specific harmonics, thus resulting in the preference in harmonic excitation.

A smooth frequency characteristic of the system is required so that such preference of harmonic excitation can be avoided. However it is worth noting that from a certain point of view, it could be advantageous to introduce such frequency-selective mechanisms [12] in the system, in order to increase the stability of particular harmonic modes used as memory states.

7 Conclusion

A delayed-feedback system with a very large effective delay was designed for the experimental test of a novel memory function utilizing large numbers of multi-stable

nonlinear modes of oscillation.

The requirements of the system demanded for the experiment are made the following. Large effective delay is necessary to excite high harmonic oscillations. Smooth monotonicity of the frequency characteristic of the system is necessary to ensure uniform stability among different memory states. And controllability of the optical input power and loop gain is necessary to facilitate the SB switch control.

Large effective delays of up to 520 were realized by employing state of the art components for 1.3μm optical communication as the key components of the system. This made it possible to obtain a large variety of stable modes. The behavior of the system was confirmed to be roughly consistent with that exhibited by a model delay-differential equation and previous experimental systems with shorter delays. Order m=2 bifurcations of high harmonic modes were found to be stable. The highest harmonic oscillation modes observed to be stable were those with harmonic number n=21 for effective delay of $T_r/T_m \approx$124 and those with harmonic number n=265 for $T_r/T_m \approx$520.

It was found that the stability of the harmonic modes for large effective delay was very sensitive to spurious resonances in the system, which resulted in preferences in the excitation of harmonics. Missing harmonics and their m=2 bifurcations could be stabilized by pumping small sinusoidal signals into the feedback loop. The presence of spurious resonances, which might be caused by piezoelectric vibration of $LiNbO_3$ substrate of the E-O modulator, was indicated by small sharp features in the transfer spectrum of the open loop gain. A correspondence between the loop gain and the threshold intensity of the pump signal needed to make a mode stable confirmed that the small sharp features, though even less than 1dB in magnitude, significantly affected the stability of the harmonic modes.

In an experimental test of the dynamical memory function, WRITE and READ of up to 21 bits of binary data using coded oscillation modes locked to an external reference clock was successfully executed. In the WRITE process, tolerance of more than $\pm$50% in the difference in peak (or valley) levels and about $\pm$50% of T_r/n in length of seed signal could be allowed, due to the dynamical stability of the oscillation modes.

The m=2 mode, at least, should be stable enough for functional applications, if the signal to noise ratio of the system is more than 20dB. This noise ratio is an

achievable value in practical systems.

The stability of the loop gain, that is the stability of the input optical power, demanded to maintain the stability of the memory mode ($m = 2$ bifurcation) was about $\pm 2\%$. This is the most demanding aspect of the system design, but it is not an impractical value.

Due to the intrinsic stability of the modes used, the dynamical memory, though of simple structure, realizes a function similar to that of a conventional delay line memory with regeneration. The intrinsic stability of data stored as stable nonlinear oscillation modes is an important advantage of this dynamical memory compared to a conventional delay line memory which stores data as a cyclic pulse pattern in a delay line with a separate regeneration mechanism to compensate pulse decay and suppress intensity and phase noise.

The dynamical memory can in principle be realized in all optical nonlinear resonators with simple structure, such as optical fiber loops [21] and solid-state optical resonators [29], though the performances of all optical systems reported so far have not reached a level which is practical for the implementation of the dynamical memory, due mainly to the need for large optical power. In this context, a low threshold nonlinear sagnac switch [30], which consists of a combination of an optical fiber and a high gain erbium doped fiber amplifier, seems to be a good candidate for realizing a practical all optical dynamical memory with fast response.

It is envisioned that this type of dynamical memory will be suited to specific uses such as temporary ring storage or fiber logic functional units in future high-speed optical fiber networks [31][32]. The possibility of cascading, using the output of one resonator to seed another, and majority logic operations, by superposition of seed signals, are also of great interest from the point of view of future all optical signal processing applications.

Appendix I

Some details of the experimental setup which are used in this paper are described in this appendix. The setup consists essentially of a controller of the SB switch and a DF system with very large effective delay. The former, an arbitrary function generator LeCroy 9100 (AFG) controlled by a personal computer (PC), generates signals for the SB switch. The latter is a hybrid electro-optic ring-resonator. The details of the components are as follows.

The LD (Mitsubishi FU-11SLD-N) can be directly modulated as fast as 600Mbits/sec. Direct modulation of the LD allows easy control of the feedback loop gain, which is proportional to the input optical power. The electro-optic (E-O) intensity modulator (Ericsson PGS6211) is a $LiNbO_3$ waveguide of Mach-Zehnder configuration with about 4.5dB insertion loss and a half-wave voltage of about 6 volts. The optical fiber delay line is a 1.3μm single mode optical fiber with 0.2dB/km propagation loss. The length of the fiber is 1000m, corresponding to 5.2μsec propagation delay. The photo-detector (Mitsubishi FU-13PD-N) is a pin photo diode for long-wavelength infrared light, with photosensitivity of 0.87A/W and bandwidth of 1.5GHz. All of the optical components are connected using FC-connectors which introduce negligible fluctuation of propagation loss in the optical path. The amplifiers are high-speed video amplifiers with 3dB bandwidth from DC to more than 150MHz. Total electronic gain in the feedback loop is 57dB. The input and output ports of all these electronic devices are adjusted to 50Ω impedance so that waveform distortion originating from impedance mismatching, which might cause irregular change in the frequency characteristic of the loop, is minimized. The response time of the feedback T_m is increased from about 10nsec to more than 270nsec by introducing capacitors in parallel in the loop to act as a low pass filter (LPF) as shown in figure 4.

A DC offset bias voltage V_o' is added at the input port of the first stage amplifier to select an appropriate range of the nonlinear E-O modulation.

Appendix II

We derive equation (12) from equation (11) by linear stability analysis.

$$T_m \frac{dV(t)}{dt} = -V(t) + V_o + \mu F(V(t - T_r)). \tag{15}$$

For small μ, that is low input optical power from the LD, there is a stable state of the loop corresponding to a constant intensity signal V^*, an equilibrium value of $V(t)$ as described by the following equations and inequality.

$$\frac{dV(t)}{dt} = 0, \tag{16}$$

$$V^* = V_o + \mu F(V^*), \tag{17}$$

and

$$\frac{\partial F}{\partial V}(V^*) < 0. \tag{18}$$

With increase in μ, this state becomes unstable and there arises stable self-oscillation in the loop. Near V^*, the dynamical behavior of V is understood with the following linearization of equation (11) [8].

$$V(t) = V^* + v(t), \tag{19}$$

$$T_m \frac{dv(t)}{dt} = -v(t) + \mu \frac{\partial F}{\partial V}(V^*) v(t - T_r), \tag{20}$$

where $v(t)$ is a small signal. By expressing the linear term $v(t)$ as $v(t) = \varepsilon \exp(st)$, where ε and s are the small amplitude and the complex phase of $v(t)$ respectively, the following characteristic equation is obtained,

$$sT_m = -1 + \mu \frac{\partial F}{\partial V}(V^*) \exp(-sT_r). \tag{21}$$

By comparing real and imaginary parts of equation (21) we obtain following equations as,

$$\lambda T_m + 1 = \mu \frac{\partial F}{\partial V}(V^*) \exp(-\lambda T_r) cos(\omega T_r), \tag{22}$$

and

$$\omega T_m = -\mu \frac{\partial F}{\partial V}(V^*) \exp(-\lambda T_r) sin(\omega T_r), \tag{23}$$

where $\lambda = Re(s)$ and $\omega = Im(s)$.

By dividing equation (23) by equation (22) we obtain

$$\frac{\omega T_m}{\lambda T_m + 1} = -tan(\omega T_r). \tag{24}$$

Oscillation occurs if s has a positive real part. So, $V(t)$ begins to be unstable and to oscillate around V^* at $\lambda = 0$. By substituting $\lambda = 0$, equation (24) becomes

$$\omega T_m = -tan(\omega T_r). \tag{25}$$

On the assumption that the period of oscillation is near $2T_r$ or $2T_r/n$, where n is integer, we expand right term of equation (25) around $\omega T_r = n\pi$ as,

$$\omega T_m \simeq -(\omega T_r - n\pi). \tag{26}$$

Under the condition $T_m \ll T_r$ and inequality (18), we obtain the oscillation frequency $f_n (= \omega/(2\pi))$ as

$$f_n \simeq \frac{n}{2T_r}(1 - \frac{T_m}{T_r}),\ n = odd. \tag{27}$$

Appendix III

In our experiment, poor reproducibility of the input optical power P_i level for a given loop gain was an issue. This was due mainly to the following causes.

Firstly, the loss in the optical path could change as much as ±0.5dB (±12%) with reconnection of the FC-connectors.

Secondly, it was observed that the loop gain was relatively sensitive to the temperature of the atmosphere around the 1m long polarization maintaining (PM) fiber pigtail of the input port of the E-O modulator. The light from the LD was elliptically polarized light with low extinction ratio (~5dB) which seemed to be due to the birefringence of the cylindrical lens mounted in the LD module. The LD light was fed directly to the PM fiber of the E-O modulator. The principal axis of the polarization ellipse in the PM fiber could change due to change of birefringence of the PM fiber with temperature variation of the atmosphere, resulting in intensity variation of the field component to be modulated in the E-O modulator. This could cause variation of loop gain in spite of a constant LD optical power. Under typical laboratory conditions at room temperature ±1°C, the gain varied less than 2%.

However, we believe that these are not intrinsic problems for engineering models of the dynamical memory, because they can be overcome with countermeasures, such as permanently fixing the optical connection points, shortening the PM fiber pigtail and using a fiber-type polarizer to improve the extinction ratio of the input light.

References

[1] K.Ikeda, "Multiple-valued stationary state and its instability of the transmitted light by a ring cavity system," Opt. Commun., vol.30, pp.257-261, Aug. 1979.

[2] K.Ikeda and H.Daido, "Optical turbulence : Chaotic behavior of light from a ring cavity," Phys. Rev. Lett. vol.45, pp.709-712, Sept. 1980

[3] H. M. Gibbs, F. A. Hopf, D. L. Kaplan and R. L. Shoemaker,"Observation of chaos in optical bistability," Phys. Rev. Lett. vol.46, pp.474-477, Feb. 1981.

[4] H.M.Gibbs, Optical Bistability : Controlling Light with Light, Orlando, Academic Press Inc., 1985, pp.257-280

[5] F.A.Hopf, D.L.Kaplan, H.M.Gibbs, and R.L.Schoemaker, "Bifurcation to chaos in optical bistability," Phys. Rev. A, vol.25, pp.2172-2182, Apr. 1982.

[6] M.W.Derstine, H.M.Gibbs, F.A.Hopf, and D.L.Kaplan, "Bifurcation gap in a hybrid optically bistable system," Phys. Rev. A, vol.26, pp.3720-3722, Dec. 1982

[7] M.W.Derstine, H.M.Gibbs, F.A.Hopf, and D.L.Kaplan, "Alternative paths to chaos in optical bistability," Phys. Rev. A, vol.27, pp.3200-3208, Jun. 1983

[8] M. Okada and K. Takizawa,"Instability of an electrooptic bistable device with a delayed feedback," IEEE J. Quantum Electron., vol.QE-17, pp.2135-2140, Oct. 1981

[9] J.Y.Gao, J,M.Yuan and L.M.Naruducci, "Instability and chaotic behavior in a hybrid bistable system with a short delay," Opt. Commun., vol.44, pp.201-206, Jan. 1983

[10] J.Y.Gao, L.M.Naruducci, L.S.Schulman, M.Squicciarini and M.Yuan, "Route to chaos in a hybrid bistable system with delay," Phys. Rev. A, vol.28, pp.2910-2914, Nov. 1983

[11] J. Chrostowski, R. Vallée, and C. Delisle, "Self-pulsing and chaos in acousto-optic bistability," Can. J. Phys., vol.61, pp.1143-1148, 1983.

[12] Réal Vallée and C. Delisle, "Mode description of the dynamical evolution of an acousto-optic bistable device," IEEE J. Quantum Electron., vol.QE-21, pp.1423-1428, Sept. 1985

[13] K.Ikeda and K.Kondo, "Successive higher-harmonic bifurcations in systems with delayed feedback," Phys. Rev. Lett. vol.49, pp.1467-1470, Nov. 1982.

[14] K.Ikeda and K.Matsumoto, "High-dimensional chaotic behavior in systems with time-delayed feedback," Physica 29D, pp.223-235, 1987.

[15] P.Davis and K.Ikeda, "Switching between multistable oscillations and applications in signal generator and memory," Technical Digest of the 16th International Conference on Quantum Electronics, ThC-3, pp.634-635, Tokyo, Jul. 1988

[16] P.Davis and K.Ikeda, "Bifurcation and dynamical memory," to be published in Phys. Rev. A

[17] T.Aida and P.Davis, "Experimental demonstration of novel dynamical memory function in a nonlinear elecro-optical ring resonator," Jap. J. Appl. Phys. vol.29, pp.L1241-L1243, Jul. 1990.

[18] Réal Vallée and Claude Delisle, "Periodicity windows in a dynamical system with a delayed feedback," Phys. Rev. A, vol.34, pp.309-318, Jul. 1986

[19] Robert M. May, "Simple mathematical models with very complicated dynamics," Nature, vol.261, pp.459-467, Jun. 10 1976.

[20] M. J. Feigenbaum, "Quantitative universality for a class of nonlinear transformations," J. Statistical Physics, vol.19, pp.25-52, 1978.

[21] H.Nakatsuka, S.Asaka, H.Itoh, K.Ikeda and M.Matsuoka, "Observation of bifurcation to chaos in an all-optical bistable system," Phys. Rev. Lett. vol.50, pp.109-112, Jan. 1983

[22] R.G.Harrison, W.S.Firth, C.A.Emshary, I.A.Al-Saidi, "Observation of period doubling in an all-optical resonator containing NH_3 gas," Phys. Rev. Lett. vol.51, pp.562-565, Aug. 1983

[23] R.G.Harrison, W.S.Firth, I.A.Al-Saidi, "Observation of bifurcation to chaos in an all-optical Fabry-Perot resonator," Phys. Rev. Lett. vol.53, pp.258-261, Jul. 1984

[24] private communication with N. Mekata of Fujitsu Labs. Ltd.

[25] Jacek Chrostowski, "Noisy bifurcations in acousto-optic bistability," Phys. Rev. A, vol.26, pp.3023-3025, Nov. 1982.

[26] Réal Vallée and Claude Delisle, "Noise versus chaos in acousto-optic bistability," Phys. Rev. A ,vol.30, pp.336-342, Jul. 1984.

[27] J.Y.Gao and L.M.Naruducci, "The effect of modulation in a bistable system with delay," Opt. Commun., vol.58, pp.360-364, Jul. 1986

[28] Jin Yue Gao, Guang Xu Jin, Jian Wei Sun, Xiu Zhen Guo, Zhi Ren Zhen, N.B.Abraham, and L.M.Narducci, "The effect of input modulation in a bistable system with delay," Opt. Commun., vol.71, pp.224-228, May 1989

[29] D.L.Kaplan, F.A.Hopf, M.W.Derstine, H.M.Gibbs and R.L.Shoemaker, "Periodic oscillation and chaos in optical bistability—possible guided-wave all-optical square-wave oscillators," Optical Engineering, vol.22, pp.161-165, Jan./Feb. 1983

[30] D.J.Richardson, R.I.Laming and D.N.Payne, "Very low threshold Sagnac switch incorporating an erbium doped fibre amplifier," Electron. Lett., vol.26, pp.1779-1781, Oct. 1990

[31] S.Suzuki, H.Suzuki, K.Kasahara, M.Fujiwara and T.Takeuchi, "Photonic packet switching using optical buffer memories," Technical Digest of Topical Meeting on Photonic Switching, FA-3, pp.112-114, Salt Lake City, Mar. 1989

[32] A.de Bosio, P.Cinato, B.Costa, A.Daniele and E.Vezzoni, "ATM photonic switching node architecture based on frequency switching techniques," Technical Digest of Topical Meeting on Photonic Switching, 14B-3, pp.226-228, Kobe, Apr. 1990

Table 1 Preference in harmonic mode excitation for $T_r/T_m \approx 124$.

◎ : stable (can be observed by only varying μ), ○ : stable (can be observed by choice of careful initial condition), △ : unstable(long lifetime after excitation with suitable initial condition), × : unstable(could not be observed)

Harmonic number n	1	3	5	7	9 19	21	23 .....
Stability	◎	△	△	○	×	◎	×

Figure 1: Schematic example of $(n = 7, m = 2)$ mode and its coding. In each T_τ interval there are 7 sub-intervals. In each sub-interval there is a peak or valley of the oscillation. The four different peak and valley levels are indicated by 2-bit labels, $00, 01, 10, 11$. The oscillation waveform is identified with a 7-element code $\boldsymbol{I} = (10, 01, 11, 00, 11, 01, 10)$ indicating peak and valley levels in a T_τ interval or a 7-element code $\boldsymbol{J} = (0, 1, 1, 0, 0, 1, 0)$ indicating peak levels in a $2T_\tau$ interval. The $\boldsymbol{J}$ code is followed by the inverted $\boldsymbol{J}$ code in the next $2T_\tau$ interval.

Figure 2: Coding of the oscillation waveform. (a)Diagram of the recurrence relation between $x(t)$ and $x(t-T_\tau)$ expressed by equation (3). (b)Cyclic sequence of 2-bit label I_i assigned to peak and valley levels separated in time interval T_τ . (c)Oscillation waveform of $(n = 1, m = 2)$ mode with peak code $\boldsymbol{J}$. (d),(e)Oscillation waveforms of $(n = 3, m = 2)$ mode with peak code $\boldsymbol{J}$. The first bit of label I_i enclosed by dashed line corresponds to 1-bit binary element of peak code $\boldsymbol{J}$. Peaks (valleys) are mapped to valleys (peaks) in T_τ later according to the cyclic sequence of label I_i, as indicated by dashed arrows.

Figure 3: Schematic example of the SB switch of $(n = 7, m = 2)$ mode with the codes $\boldsymbol{S}$ and $\boldsymbol{J}$. The upper signal is the seed signal and the lower signal is the oscillation waveform.

Figure 4: Experimental setup.
LD:laser diode (wavelength $\lambda \approx 1.3\mu$m, optical output power $P_o \sim$ 1mW) **E-O modulator**:Ericsson PGS6211 $LiNbO_3$ waveguide intensity modulator (halfwave voltage $V_\pi \approx$ 6V) **optical fiber**:1.3μm single mode optical fiber (length$\approx$1000m) **PIN**:pin photo diode (photo sensitivity $\approx$ 0.87A/W) **LPF**:low pass filter **ATT**: attenuator (attenuation = -6dB) **P**:power divider (insertion loss = -6dB) **AMP**:video amplifier (-3dB bandwidth$\sim$150MHz, 15dB gain in the final stage and 20dB in the other stages) **PC**:personal computer **AFG**:LeCroy9100 arbitrary function generator **SG**:timing signal generator **DET**:detector (threshold circuit)

Figure 5: Shape of the nonlinear E-O modulation characteristic. This curve shows the relation between V and V_i where $V = V_o + \mu F(V_i)$ with constant V_o and μ.

Figure 6: Transfer spectrum $|G(\omega)|$ of the open loop gain. This was measured with small amplitude sinusoidal signal V_i, where $G(\omega)$ is defined in terms of the Fourier transforms of V and V_i as $V(\omega) = G(\omega)V_i(\omega)$. : (a) without low pass filter (LPF), (b) with LPF ($T_r/T_m \approx 520$), (c) with LPF ($T_r/T_m \approx 124$), and (d) with LPF ($T_r/T_m \approx 63$).

Figure 7: An example of ripple on $V(t)$ observed when the system is driven with rectangular wave V_i in the open loop configuration for $T_r/T_m \approx 124$.

Figure 8: Small signal resonance characteristic of the nonlinear resonator for $T_r/T_m \approx 124$. (a)frequency range from 0 to 2.0MHz, and (b)from 2.0 to 4.0MHz.

Figure 9: Dependence of frequencies of fundamental mode f_1 on effective delay T_r/T_m. Solid line shows values calculated from equation (12) for n=1 and dots show experimental values.

Figure 10: Oscillation waveform of (n,m)=(1,2) mode for $T_r/T_m \approx 124$.

Figure 11: Bifurcation diagram for $T_r/T_m \approx 124$. This diagram shows bifurcation of levels of n=1 oscillation for $T_r/T_m \approx 124$ obtained by slowly varying input optical power $P_i (\propto \mu)$ at about 10Hz and observing P_i and V in the X-Y mode of the oscilloscope.

Figure 12: Oscillation of one of the (n,m)=(265,2) modes for $T_r/T_m \approx 520$. (a) waveform, and (b) power spectrum.

Figure 13: Bifurcation diagrams of (a) n=1 and (b) n=21 modes for $T_r/T_m \approx 124$. These diagrams were obtained by the same method as for figure 11. The propagation loss in the optical path and E-O modulation curve in this measurement were slightly different from those for figure 11, due to reconnection of FC-connectors in the optical path.

Figure 14: Frequency locking characteristics for $T_r/T_m \approx 124$ at the modulation depth of input optical power P_i of 0.4%. (a) (7,2) mode, and (b) (21,2) mode.

Figure 15: Dependence of frequency locking range on modulation depth of input optical power P_i, for $T_r/T_m \approx 124$.

Figure 16: Two examples of 21-bit data WRITE to dynamical memory. (i) bit sequence '110001100010000010101' (ii) bit sequence '101010101010101010101'.
(a) The change of μ from μ_{off} to μ_{on} corresponds to change of input optical power P_i. The increase of the input optical power ΔP_i was about 0.25mW. (b) $V_o(t)$ modulated by the seed signal, (c) the excited oscillation $V(t)$, one of the (21,2) modes. (d) The stable asymptotic state of the oscillation $V(t)$, observed a long time ($\geq 10^6 T_r$) after WRITE.

Figure 17: An example of transient waveform observed in the WRITE procedure when the shape of the seed signal has discrepancies of -30% in peak levels and +30% in valley levels from the optimum levels. The optimum levels were slightly different from those for figure 16, due to reconnection of FC-connectors in the optical path.

Figure 18: Example of 21-bit data READ from dynamical memory locked to an external reference clock. Pt: Timing pulse (period $4T_r$), V': Stable oscillation (proportional to V), Dt: Binary data read from V' by thresholding.

Figure 19: Two examples of the erasure of a (21,2) mode. Erasing begins T_r after switching μ back to μ_{off}, due to the delay line. (a) Erasing when the value of μ_{off} was set to be nearly zero. (b) Erasing when μ_{off} was a larger non-zero value. A switching transient of a few T_r in length is observed.

Figure 20: Dependence of oscillation mode on input optical power P_i and pump intensity for $T_r/T_m \approx 124$. (a) Oscillation modes without pumping signal, and (b)$\sim$(g) oscillation modes for increasing intensity of pumping signal at 1.0482MHz showing recovery of n=11 mode. (1,1),(1,2),(11,1),$\cdots$ denote oscillation mode classifications (n,m) and (C) denotes chaotic oscillation. The propagation loss in the optical path and E-O modulation curve in this measurement were slightly different from those for figure 11, due to reconnection of FC-connectors in the optical path.

Figure 21: Phase diagram of mode excitation obtained from figure 20 drawn in input optical power P_i - pump intensity space.

Figure 22: Relation between transfer spectrum of the open loop gain and threshold pump intensity required to stabilize missing harmonics. (a) Transfer spectrum $|G(\omega)|$ of the open loop gain for $T_r/T_m \approx 520$ expanded around the frequency of the 265th harmonic, and (b) threshold pump intensity required to stabilize the corresponding harmonic. The 265th harmonic spontaneously oscillates, and the 261th harmonic oscillates after initial excitation with pump signal.

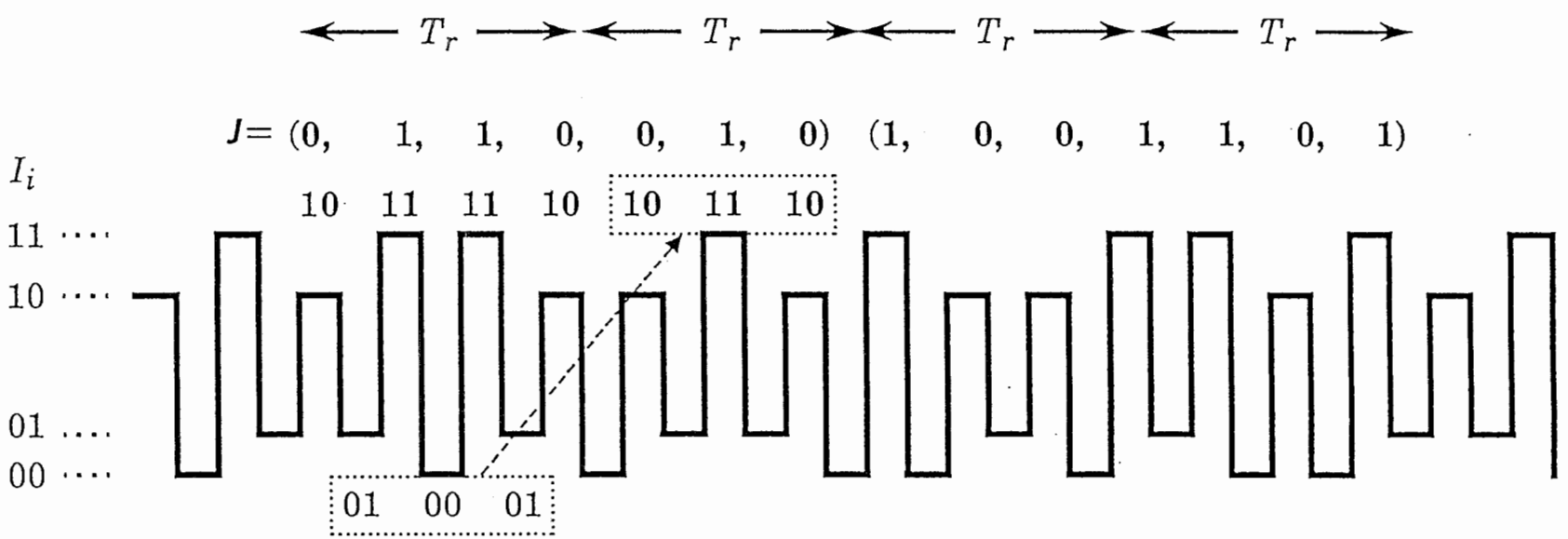

Figure 1: Schematic example of $(n = 7, m = 2)$ mode and its coding. In each T_r interval there are 7 sub-intervals. In each sub-interval there is a peak or valley of the oscillation. The four different peak and valley levels are indicated by 2-bit labels, $00, 01, 10, 11$. The oscillation waveform is identified with a 7-element code $\boldsymbol{I} = (10, 01, 11, 00, 11, 01, 10)$ indicating peak and valley levels in a T_r interval or a 7-element code $\boldsymbol{J} = (0, 1, 1, 0, 0, 1, 0)$ indicating peak levels in a $2T_r$ interval. The $\boldsymbol{J}$ code is followed by the inverted $\boldsymbol{J}$ code in the next $2T_r$ interval.

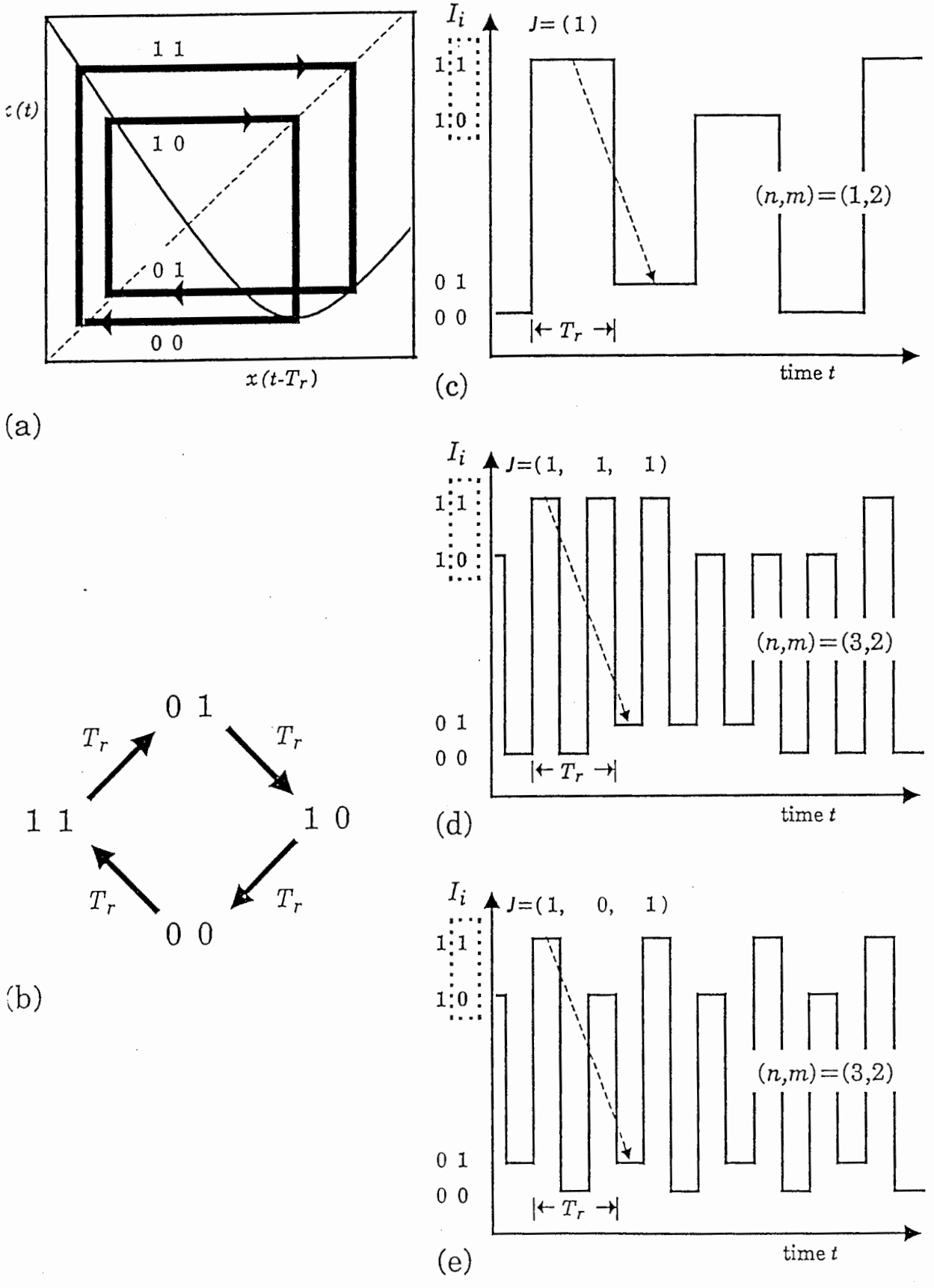

Figure 2: Coding of the oscillation waveform. (a)Diagram of the recurrence relation between $x(t)$ and $x(t-T_r)$ expressed by equation (3). (b)Cyclic sequence of 2-bit label I_i assigned to peak and valley levels separated in time interval T_r . (c)Oscillation waveform of $(n=1, m=2)$ mode with peak code $\boldsymbol{J}$. (d),(e)Oscillation waveforms of $(n=3, m=2)$ mode with peak code $\boldsymbol{J}$. The first bit of label I_i enclosed by dashed line corresponds to 1-bit binary element of peak code $\boldsymbol{J}$. Peaks (valleys) are mapped to valleys (peaks) in T_r later according to the cyclic sequence of label I_i, as indicated by dashed arrows.

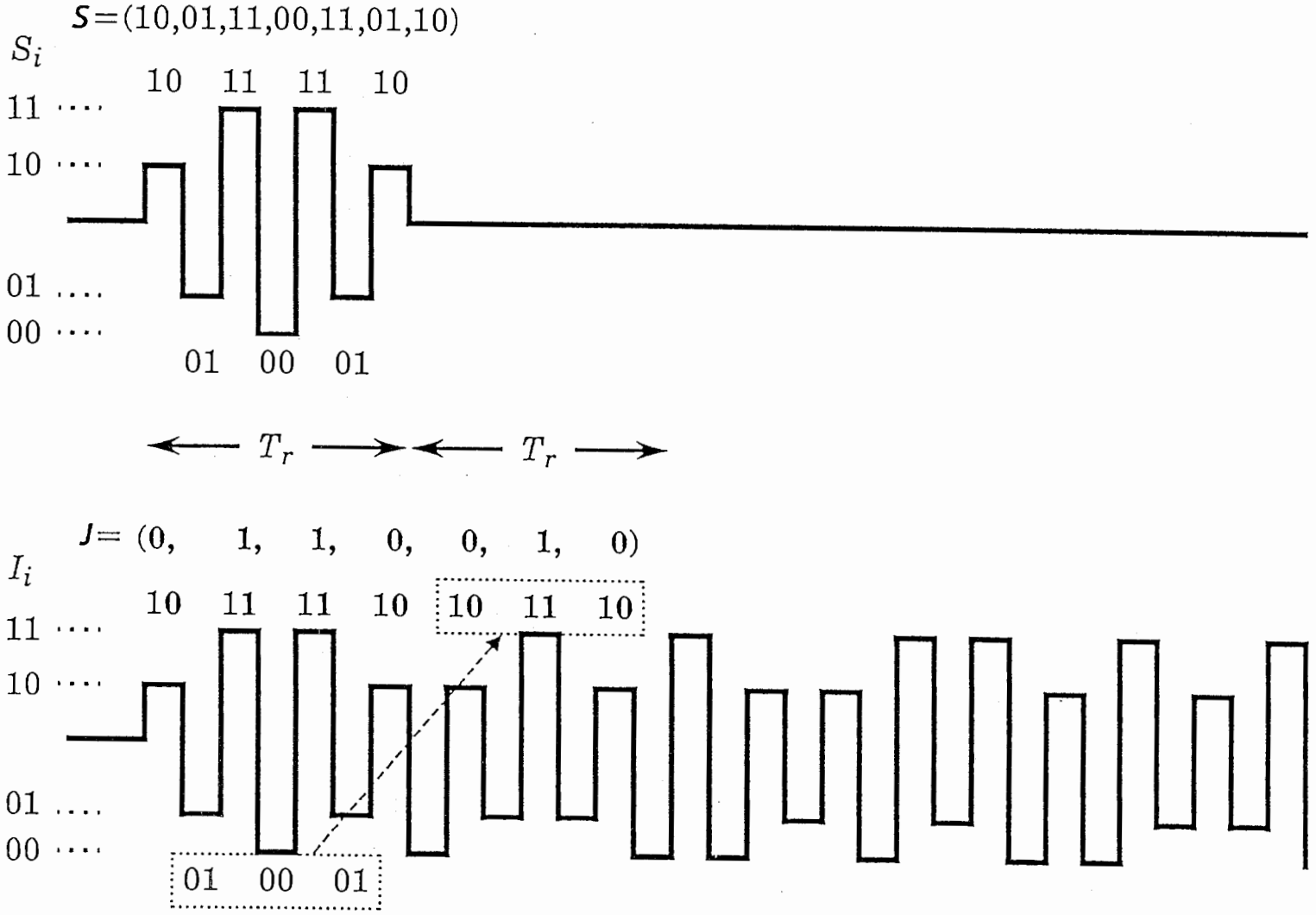

Figure 3: Schematic example of the SB switch of $(n = 7, m = 2)$ mode with the codes $\boldsymbol{S}$ and $\boldsymbol{J}$. The upper signal is the seed signal and the lower signal is the oscillation waveform.

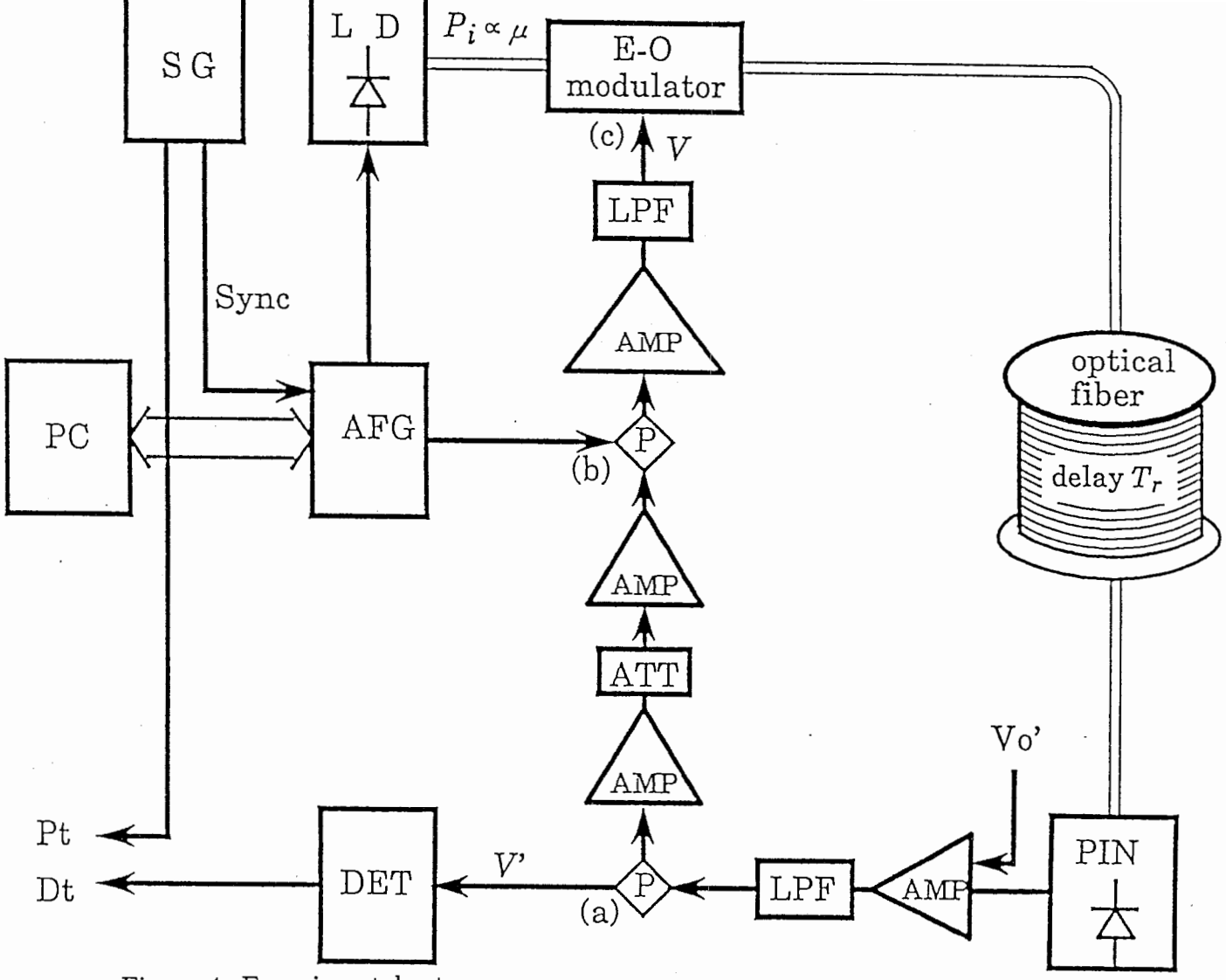

Figure 4: Experimental setup.
LD:laser diode (wavelength $\lambda \approx 1.3\mu$m, optical output power $P_o \sim$ 1mW) **E-O modulator**:Ericsson PGS6211 $LiNbO_3$ waveguide intensity modulator (halfwave voltage $V_\pi \approx$ 6V) **optical fiber**:1.3μm single mode optical fiber (length≈1000m) **PIN**:pin photo diode (photo sensitivity ≈ 0.87A/W) **LPF**:low pass filter **ATT**: attenuator (attenuation = -6dB) **P**:power divider (insertion loss = -6dB) **AMP**:video amplifier (-3dB bandwidth~150MHz, 15dB gain in the final stage and 20dB in the other stages) **PC**:personal computer **AFG**:LeCroy9100 arbitrary function generator **SG**:timing signal generator **DET**:detector (threshold circuit)

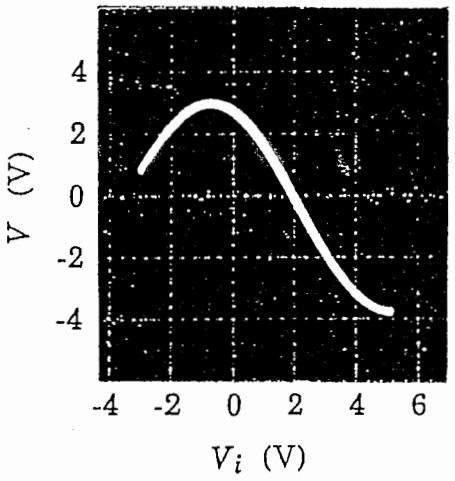

Figure 5: Shape of the nonlinear E-O modulation characteristic. This curve shows the relation between V and V_i where $V = V_o + \mu F(V_i)$ with constant V_o and μ.

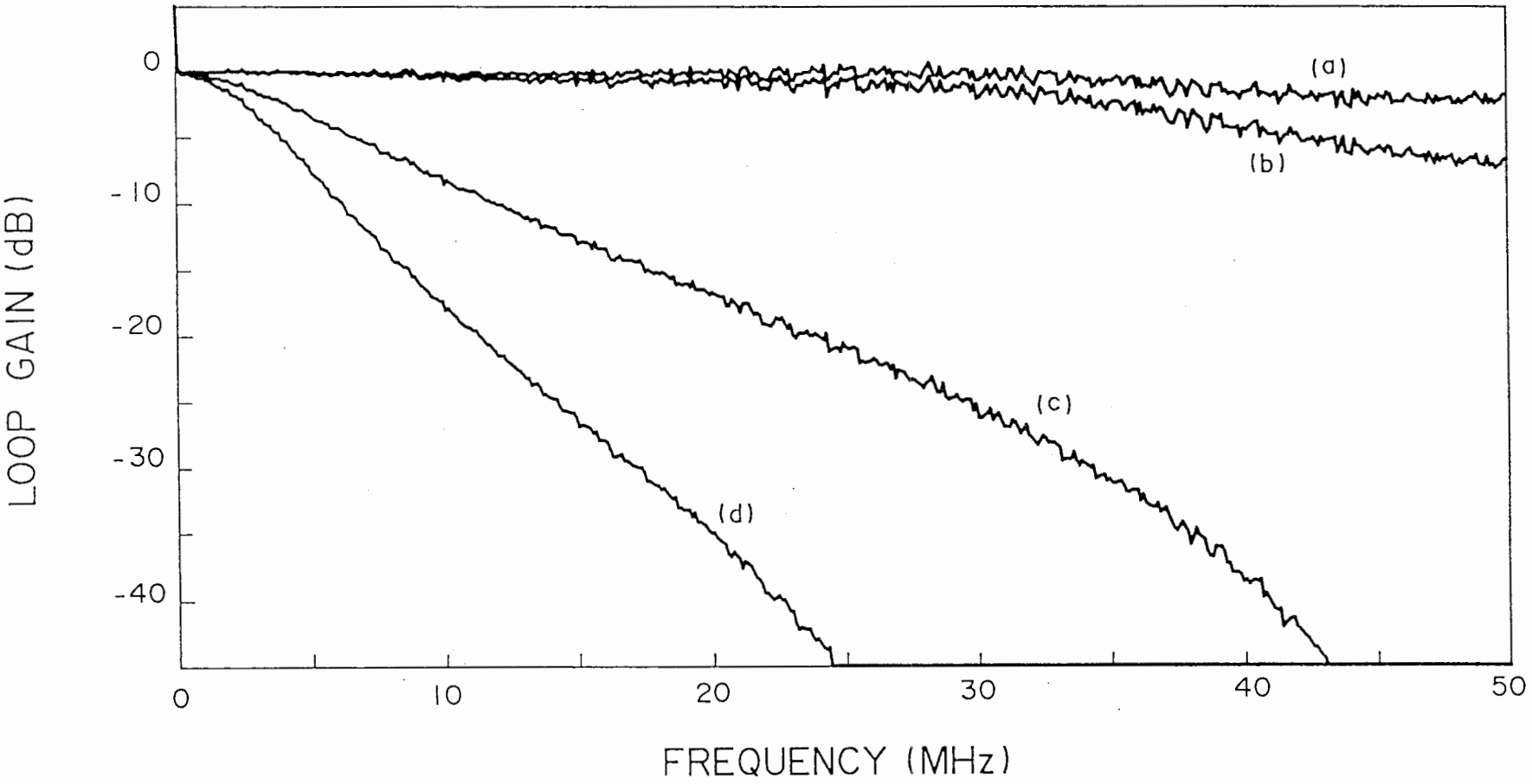

Figure 6: Transfer spectrum $|G(\omega)|$ of the open loop gain. This was measured with small amplitude sinusoidal signal V_i, where $G(\omega)$ is defined in terms of the Fourier transforms of V and V_i as $V(\omega) = G(\omega)V_i(\omega)$. : (a) without low pass filter (LPF), (b) with LPF ($T_r/T_m \approx 520$), (c) with LPF ($T_r/T_m \approx 124$), and (d) with LPF ($T_r/T_m \approx 63$).

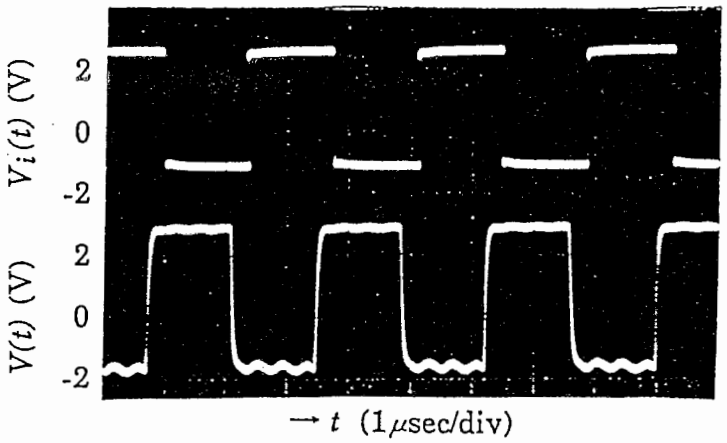

Figure 7: An example of ripple on $V(t)$ observed when the system is driven with rectangular wave V_i in the open loop configuration for $T_r/T_m \approx 124$.

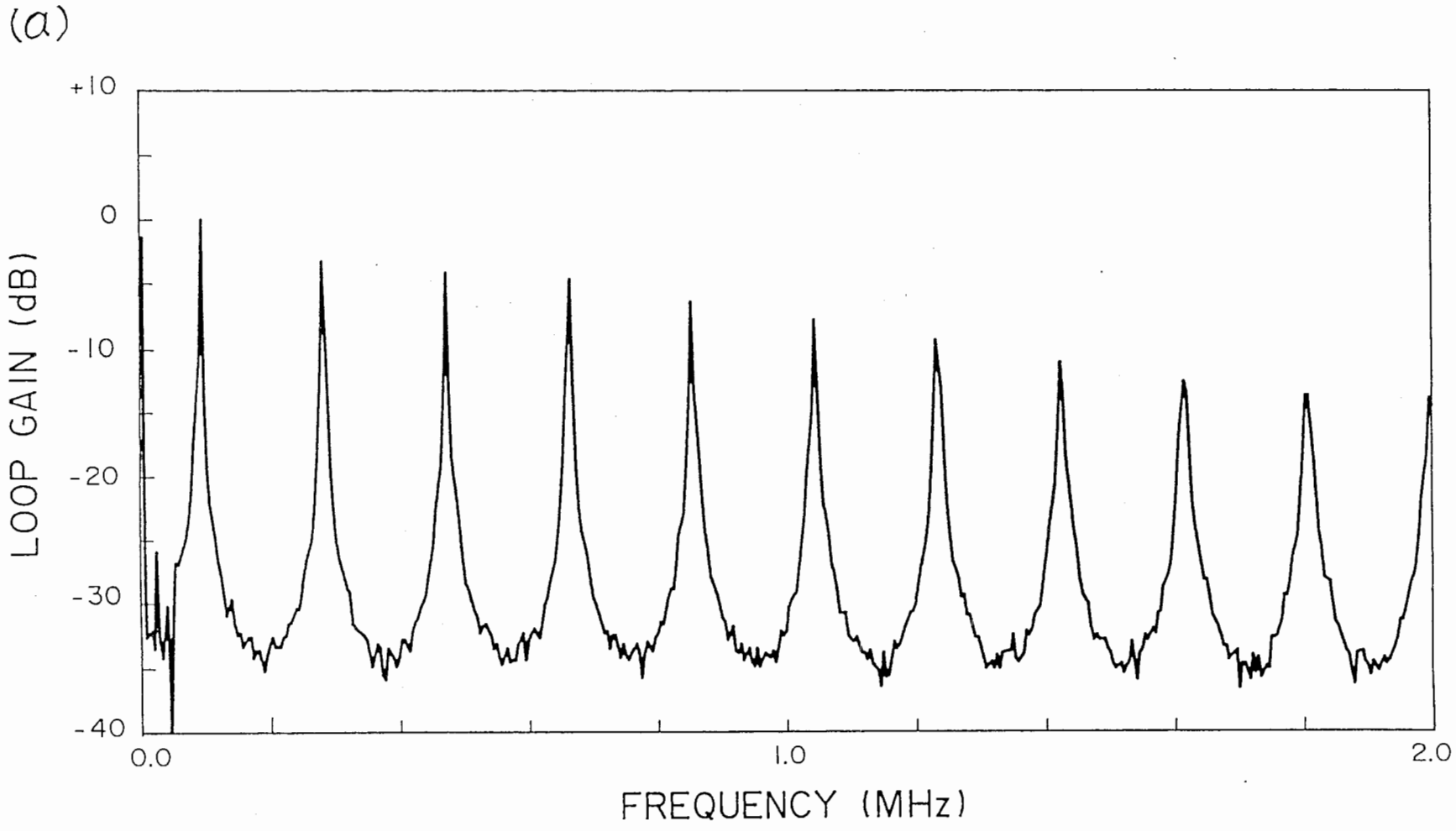

Figure 8: Small signal resonance characteristic of the nonlinear resonator for $T_r/T_m \approx 124$. (a)frequency range from 0 to 2.0MHz, and (b)from 2.0 to 4.0MHz.

(b)

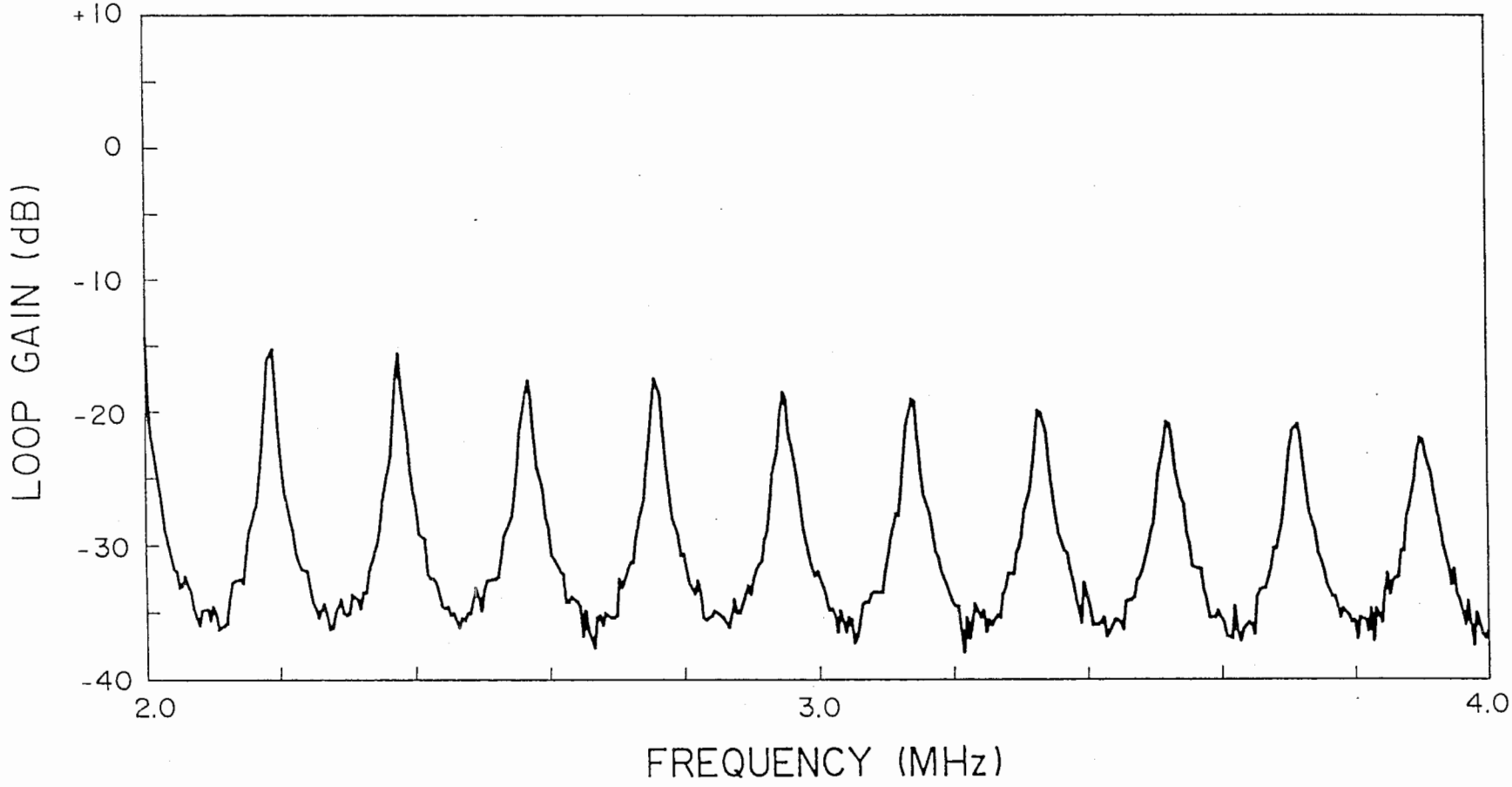

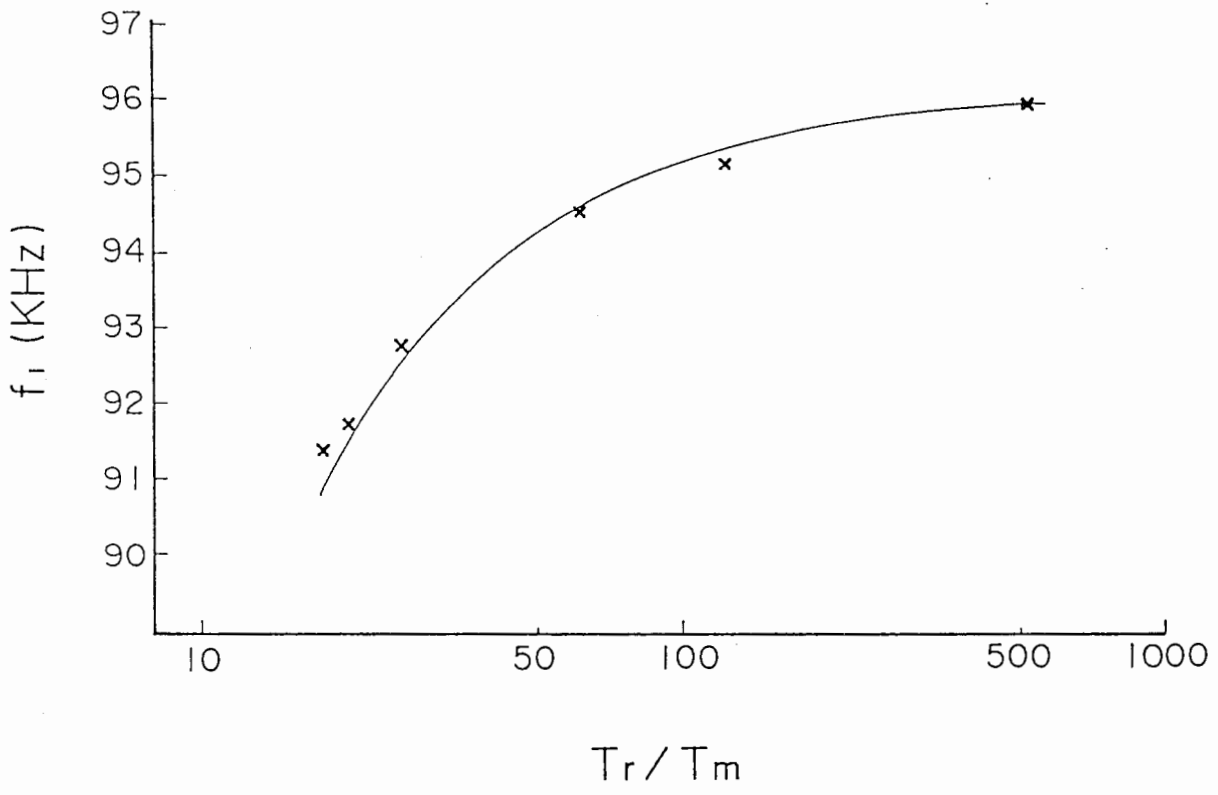

Figure 9: Dependence of frequencies of fundamental mode f_1 on effective delay T_r/T_m. Solid line shows values calculated from equation (12) for n=1 and dots show experimental values.

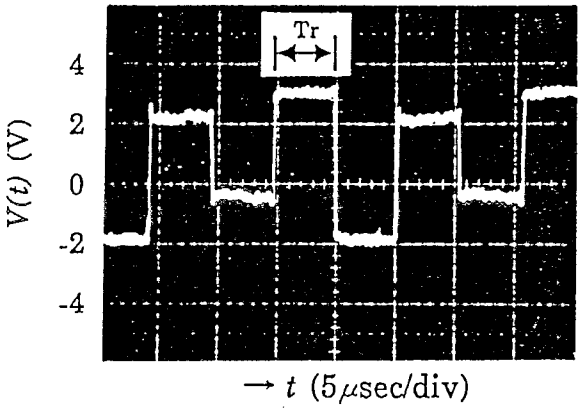

Figure 10: Oscillation waveform of (n,m)=(1,2) mode for $T_r/T_m \approx 124$.

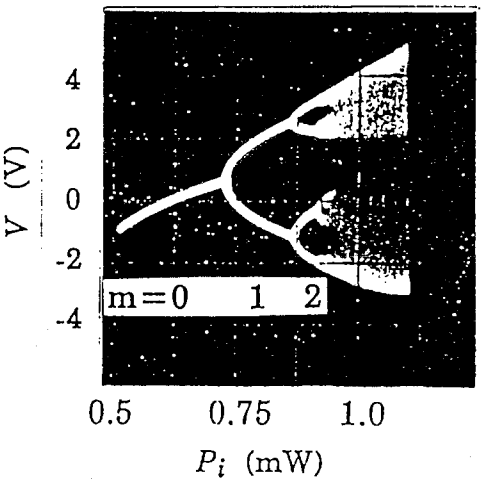

Figure 11: Bifurcation diagram for $T_r/T_m \approx 124$. This diagram shows bifurcation of levels of n=1 oscillation for $T_r/T_m \approx 124$ obtained by slowly varying input optical power $P_i(\propto \mu)$ at about 10Hz and observing P_i and V in the X-Y mode of the oscilloscope.

(a)

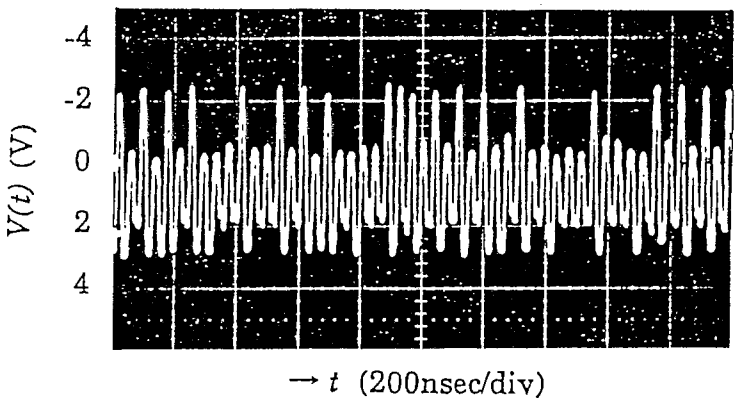

Figure 12: Oscillation of one of the (n,m)=(265,2) modes for T_r/T_m ≈520. (a) waveform, and (b) power spectrum.

(g)
RELATIVE POWER INTENSITY (dB)
+20
0
-20
-40
-60
0
10
20
30
40
50
FREQUENCY (MHz)

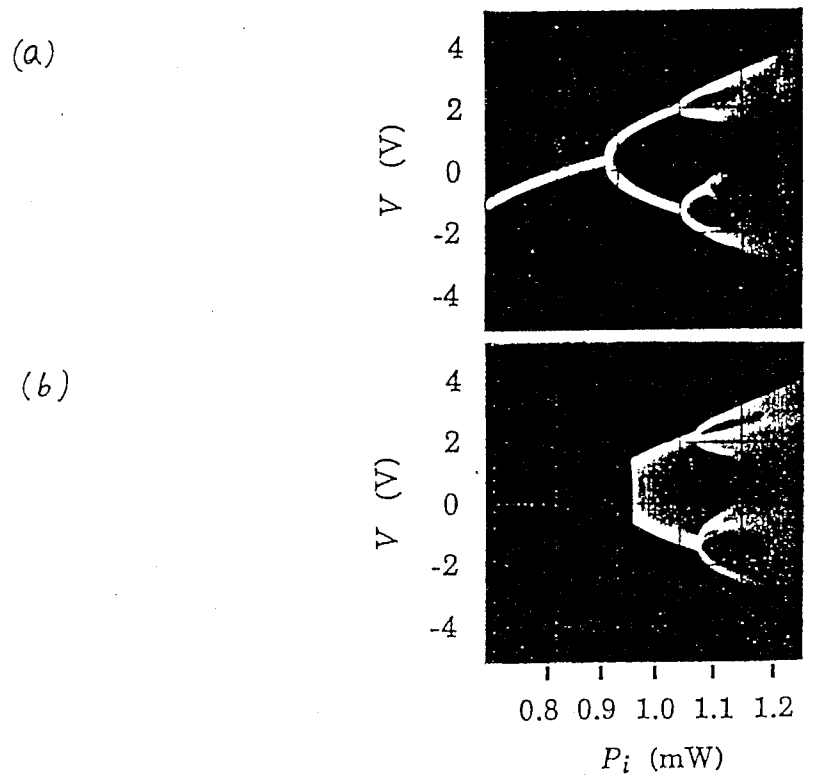

Figure 13: Bifurcation diagrams of (a) n=1 and (b) n=21 modes for $T_r/T_m \approx 124$. These diagrams were obtained by the same method as for figure 11. The propagation loss in the optical path and E-O modulation curve in this measurement were slightly different from those for figure 11, due to reconnection of FC-connectors in the optical path.

(a)

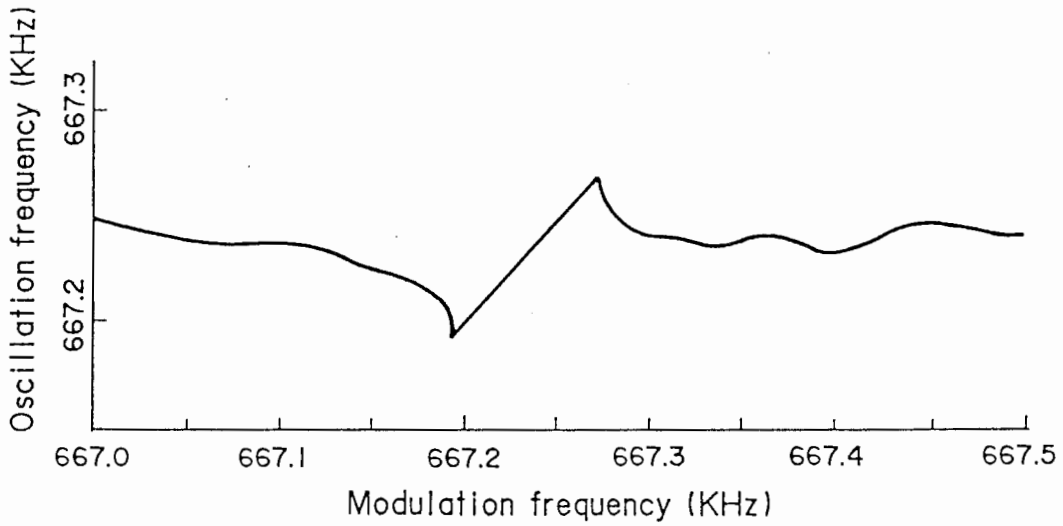

(b)

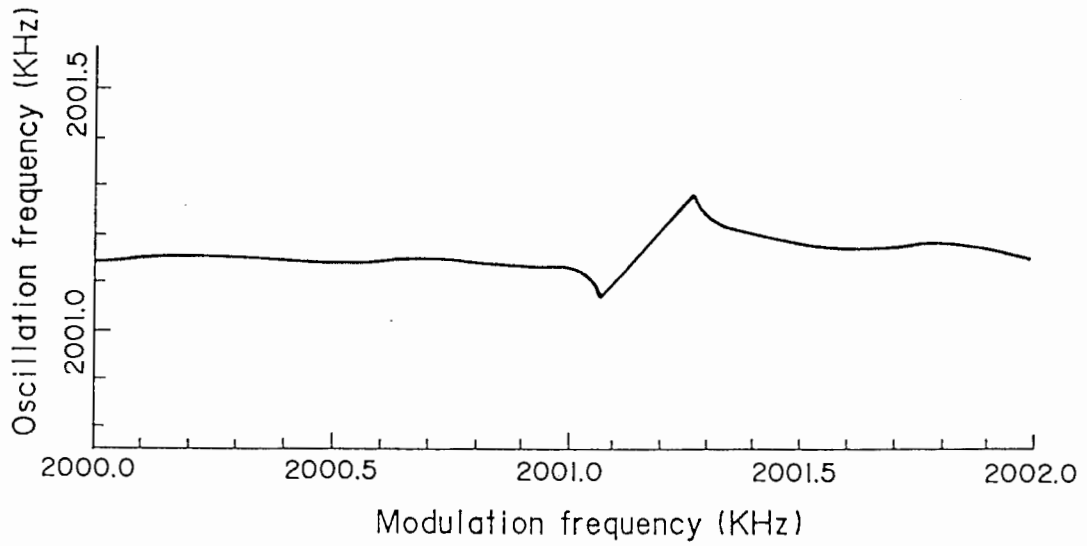

Figure 14: Frequency locking characteristics for T_r/T_m ≈124 at the modulation depth of input optical power P_i of 0.4%. (a) (7,2) mode, and (b) (21,2) mode.

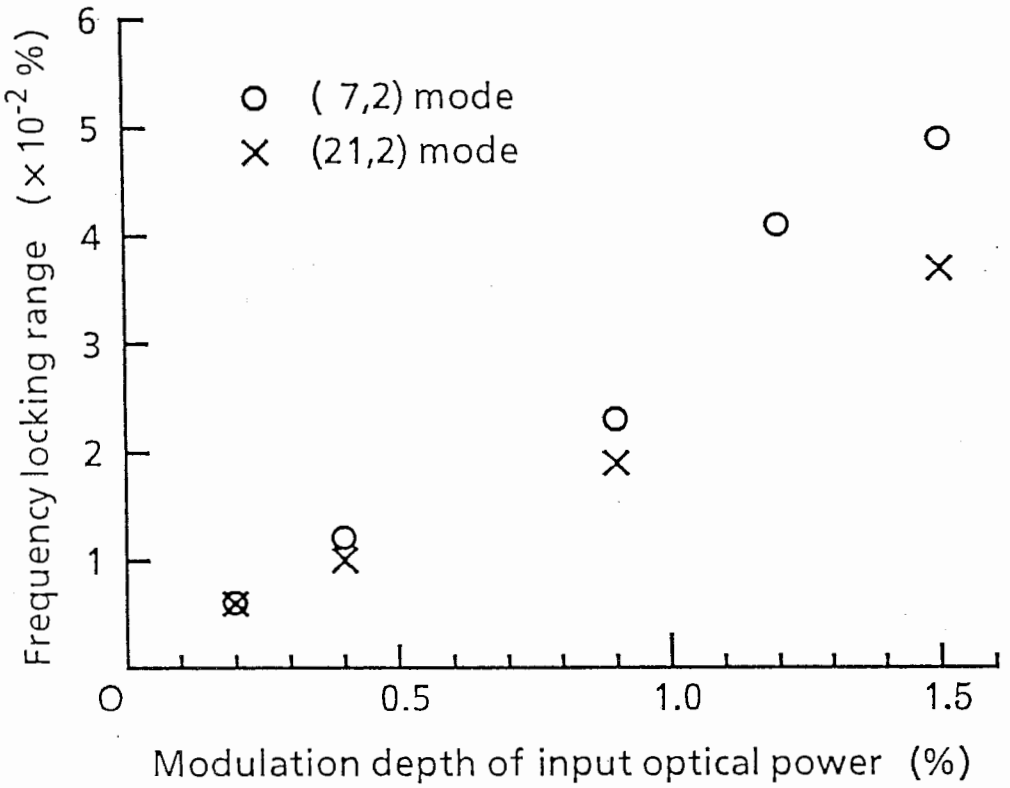

Figure 15: Dependence of frequency locking range on modulation depth of input optical power P_i, for $T_r/T_m \approx 124$.

(i)

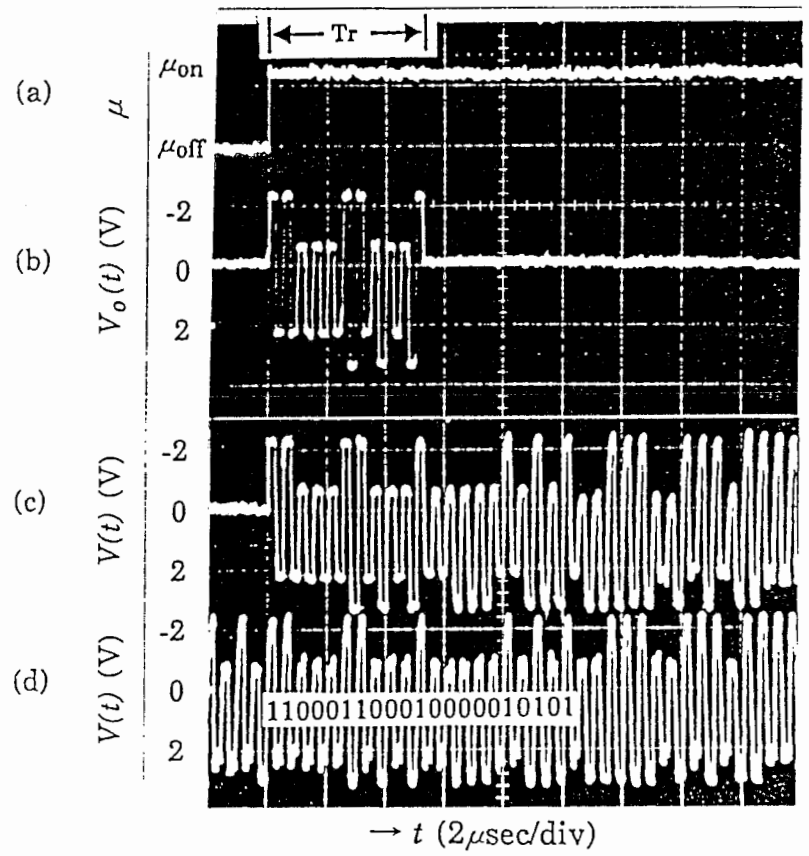

Figure 16: Two examples of 21-bit data WRITE to dynamical memory. (i) bit sequence '110001100010000010101' (ii) bit sequence '101010101010101010101'. (a) The change of μ from μ_{off} to μ_{on} corresponds to change of input optical power P_i. The increase of the input optical power ΔP_i was about 0.25mW. (b) $V_o(t)$ modulated by the seed signal, (c) the excited oscillation $V(t)$, one of the (21,2) modes. (d) The stable asymptotic state of the oscillation $V(t)$, observed a long time ($\geq 10^6 T_r$) after WRITE.

(ii)

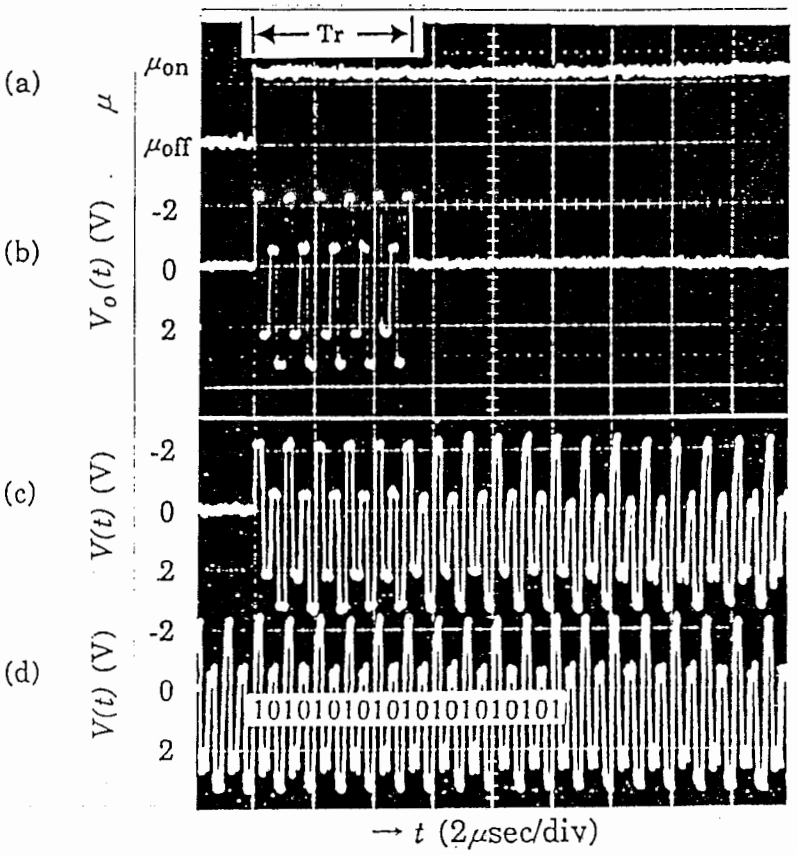
(a)
(b)
(c)
(d)
Tr
μon
μoff
μ
Vo(t) (V)
V(t) (V)
V(t) (V)
-2
0
2
-2
0
2
-2
0
2
10101010101010101010101
→ t (2μsec/div)

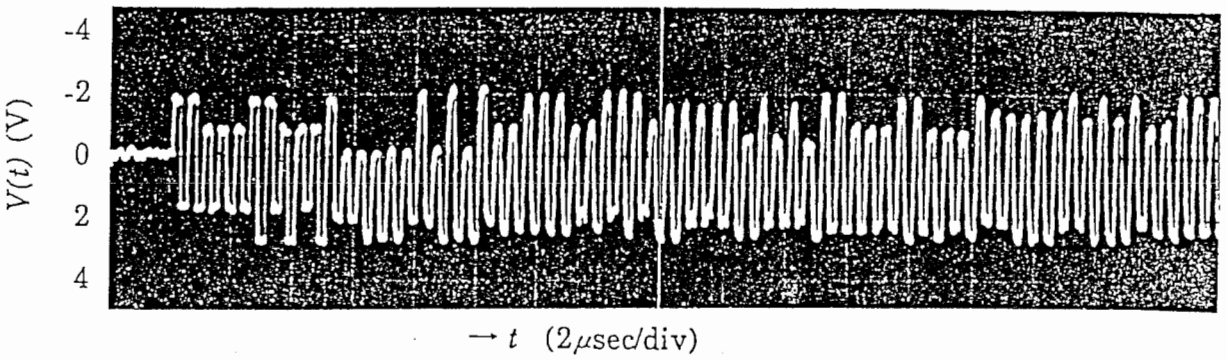

Figure 17: An example of transient waveform observed in the WRITE procedure when the shape of the seed signal has discrepancies of -30% in peak levels and +30% in valley levels from the optimum levels. The optimum levels were slightly different from those for figure 16, due to reconnection of FC-connectors in the optical path.

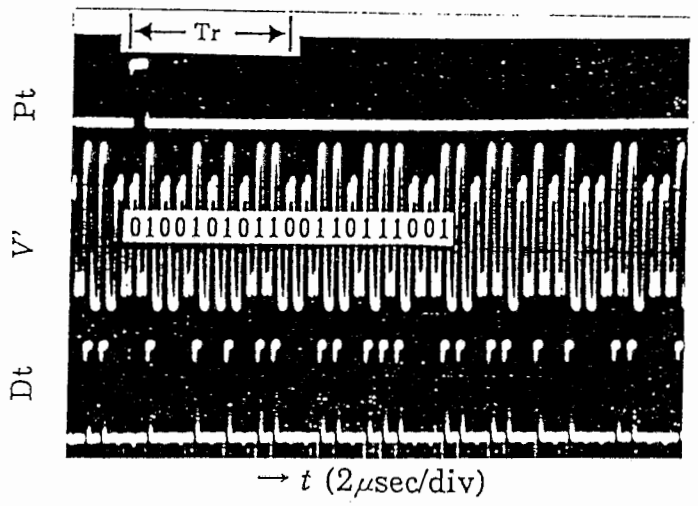

Figure 18: Example of 21-bit data READ from dynamical memory locked to an external reference clock. Pt: Timing pulse (period $4T_r$), V': Stable oscillation (proportional to V), Dt: Binary data read from V' by thresholding.

(a)

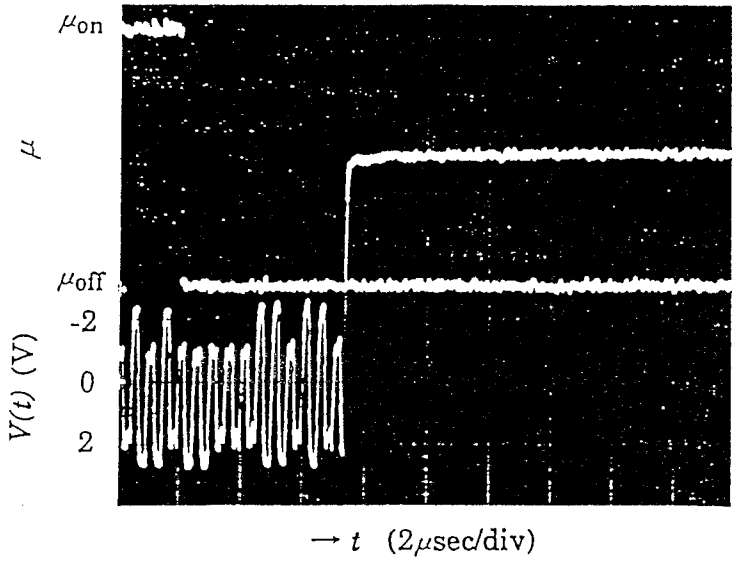

(b)

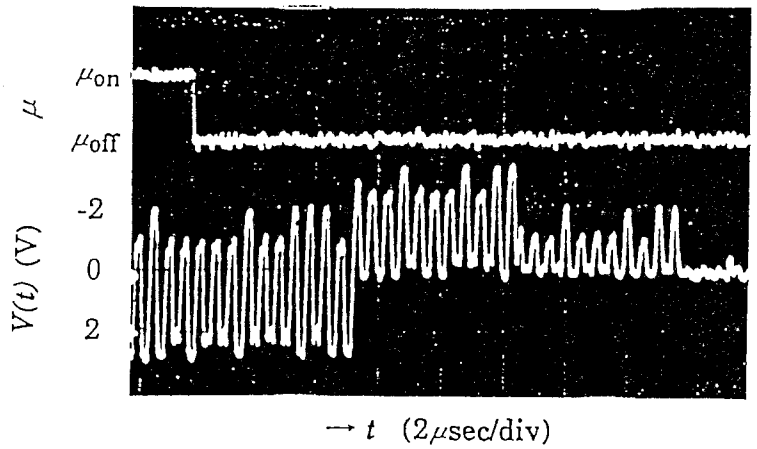

Figure 19: Two examples of the erasure of a (21,2) mode. Erasing begins T_r after switching μ back to μ_{off}, due to the delay line. (a) Erasing when the value of μ_{off} was set to be nearly zero. (b) Erasing when μ_{off} was a larger non-zero value. A switching transient of a few T_r in length is observed.

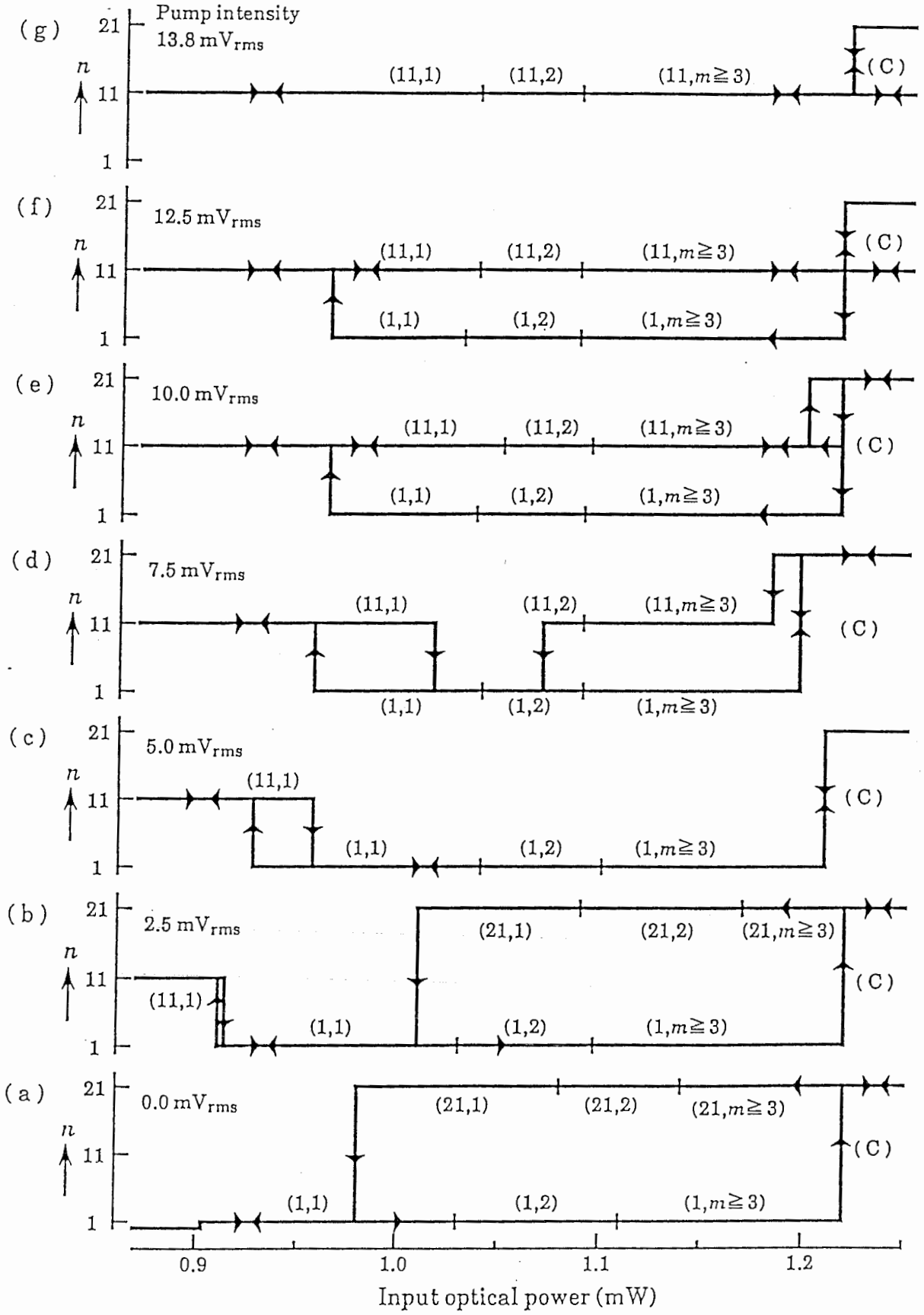

Figure 20: Dependence of oscillation mode on input optical power P_i and pump intensity for $T_r/T_m \approx 124$. (a) Oscillation modes without pumping signal, and (b)~(g) oscillation modes for increasing intensity of pumping signal at 1.0482MHz showing recovery of n=11 mode. (1,1),(1,2),(11,1),$\cdots$ denote oscillation mode classifications (n, m) and (C) denotes chaotic oscillation. The propagation loss in the optical path and E-O modulation curve in this measurement were slightly different from those for figure 11, due to reconnection of FC-connectors in the optical path.

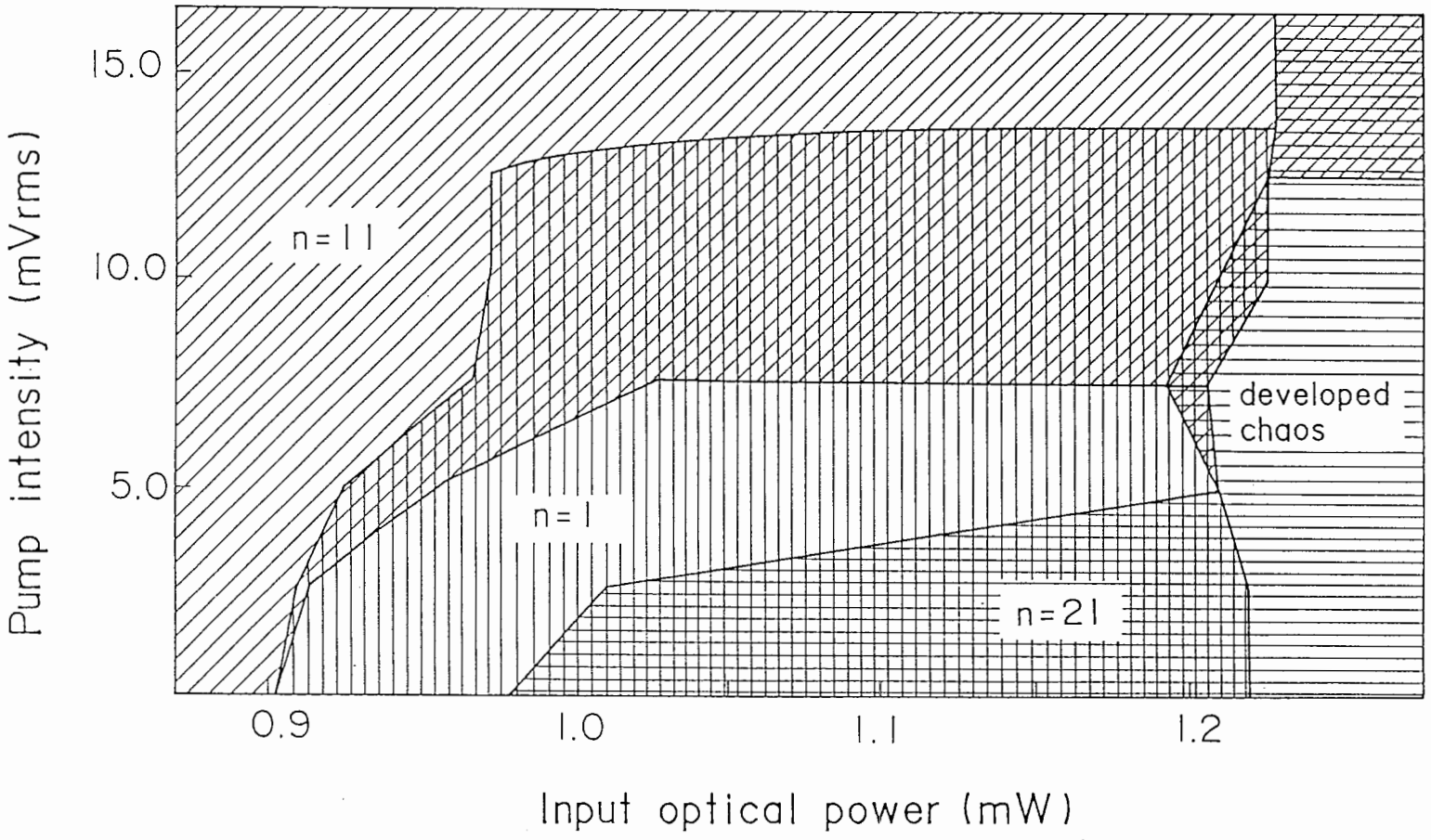

Figure 21: Phase diagram of mode excitation obtained from figure 20 drawn in input optical power P_i - pump intensity space.

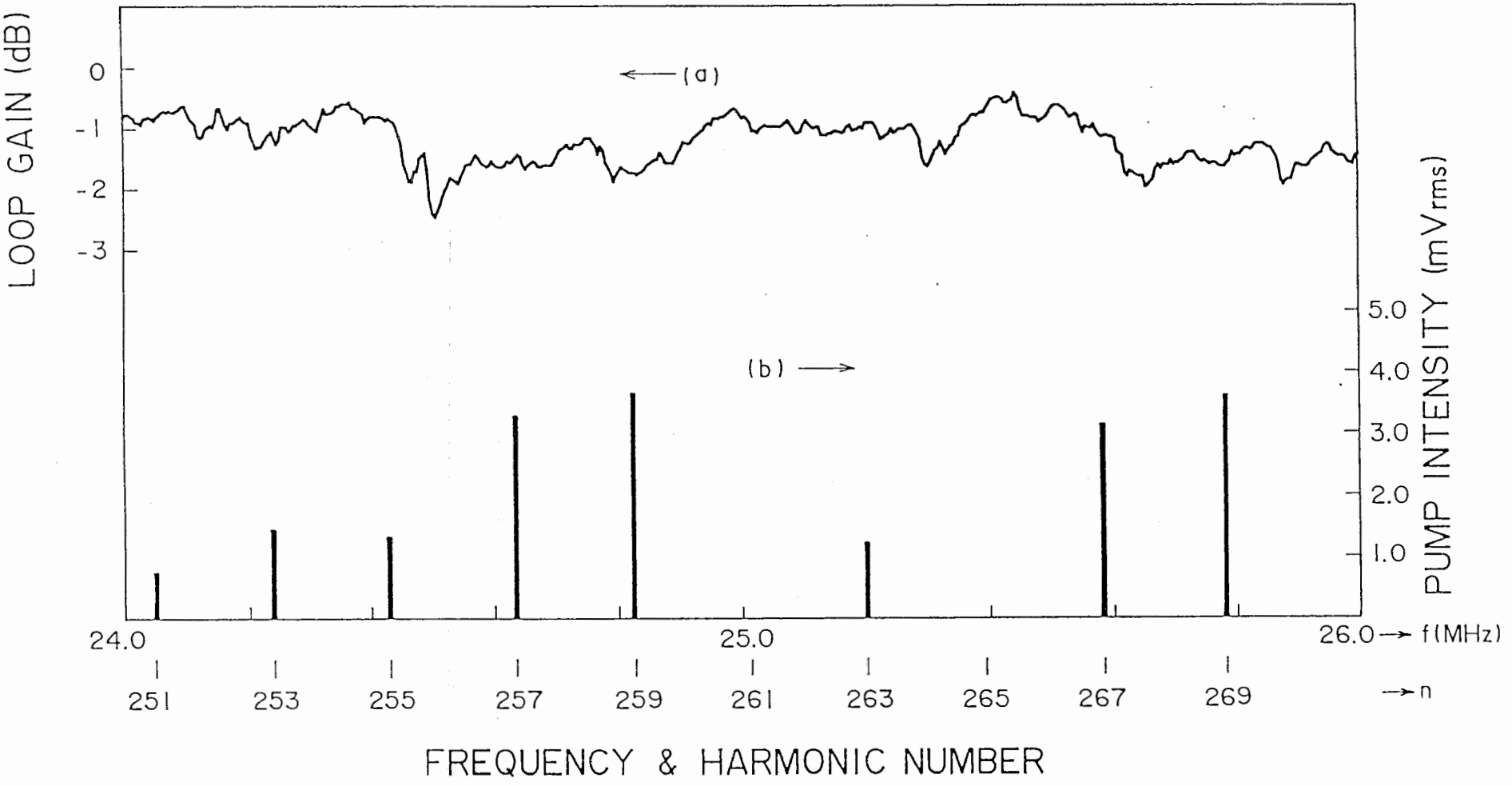

Figure 22: Relation between transfer spectrum of the open loop gain and threshold pump intensity required to stabilize missing harmonics. (a) Transfer spectrum $|G(\omega)|$ of the open loop gain for $T_r/T_m \approx 520$ expanded around the frequency of the 265th harmonic, and (b) threshold pump intensity required to stabilize the corresponding harmonic. The 265th harmonic spontaneously oscillates, and the 261th harmonic oscillates after initial excitation with pump signal.

Chapter III

Storage of Optical Pulse Data Sequences in A Loop Memory using Multistable Oscillations

Abstract

A new configuration for a loop memory using multistable nonlinear oscillation modes was proposed. The basic functions of the proposed loop memory have been confirmed with experimental demonstration of "write" and "erase" using optical pulse sequences in an electro-optical hybrid nonlinear ring resonator.

1 Introduction

A nonlinear ring resonator, such as an optical bistable system with delayed-feedback, can have a huge variety of multistable oscillation modes [1]-[3]. We have previously performed an experiment on an electro-optical (E-O) hybrid nonlinear ring resonator in which we demonstrated selective switching of multistable oscillation modes and examined the feasibility of utilizing the modes for data storage [4][5]. The intrinsic stability of data stored as stable oscillation modes is an important advantage of the loop memory compared to a conventional optical delay line memory. As there is an intrinsic regeneration mechanism in the nonlinear oscillation to compensate pulse decay and suppress amplitude and phase noise the proposed memory can have simple structure. This simplicity of structure should be of considerable merit in future high-speed optical communication systems, where buffer loop memories could be used in switching nodes [6].

In the previous experiment on the nonlinear ring resonator for memory [5], switching of modes corresponding to memory states was done by simultaneously changing a control parameter, the cw laser pump power, and injecting a seed signal. A unipolar return-to-zero (RZ) binary data pulse train was easily obtained as output by thresholding peak levels of the oscillation waveform. The seed signal, a "write" signal coded from input binary data, was a four-level signal including negative levels. The need for negative level input signals posed problems for control and cascading in application of the memory function to a conventional optical communication system using unipolar binary data pulses.

In this letter, we make a proposal of a configuration for using the memory function which solves the above mentioned problem, and report experimental results of "write" and "erase" using optical pulse data, which confirm the feasibility of the proposed configuration. The possibility of all-optical operation of the memory is also mentioned.

2 Configuration and principle of the loop memory

Figure 1 shows the proposed configuration of the loop memory. The nonlinear ring oscillator is formed by an optical fiber loop of round-trip time T_r, including an active

nonlinear element with response time T_m. Couplers dedicated to "write", "erase", "read" and "locking" ports are attached to inject or to detect signals. The delayed feedback of the "read" output to "write" is used for the "erase" operation. The active nonlinear element is assumed to have a sinusoidal type relationship between input intensity and output intensity. An all-optical element could in principle be achieved with a Kerr switch [7]. In a hybrid electro-optical implementation, the nonlinear element could be a laser with an E-O intensity modulator [5].

With large effective delay (round-trip-time T_r/response-time $T_m \gg 1$), many different modes can oscillate stably in the ring. The modes can be classified into classes, each class labeled by (n, m) where n is an odd harmonic and m is a bifurcation order [3]. Examples of (21,2) modes are shown below in figure 3. The relationship between the modes and data stored in the waveform is as follows. A mode in the $(n, 2)$ class can be considered as a carrier oscillation of period $2T_r/n$, whose peaks (and also valleys) are modulated in two levels, a high "1" level and a low "0" level. The peak modulation pattern corresponds to a cyclic $2n$-bit pattern. Data stored in the modulation peak pattern can be read by thresholding the peak levels. The resulting "read" signal is a periodic RZ binary optical pulse train, corresponding to a sequence of n bits of information in a time interval of length $2T_r$ followed by the inverted n-bit sequence. Different modes in the $(n, 2)$ class have different peak modulation patterns. With phase identification, there is an $(n, 2)$ oscillation for every n-bit sequence, and the capacity of the memory using the $(n, 2)$ class of oscillations is n bits.

The important feature of this proposal is that "write" and "erase" of data can be executed using the same sort of RZ binary pulse train which is obtained as "read" signal. The "write" is executed by injecting an n-bit RZ binary optical pulse train into the loop through the "in" coupler. Input pulses should have both width and separation of about T_r/n. An n-bit input pulse train has total length $2T_r$. The "erase" operation can be executed by injecting a "read" signal of length $2T_r$ back into the loop after a delay of $2T_r$, which corresponds to superposed "write" of the inverse bit-pattern to cancel the n-bit pattern stored in the oscillation waveform. Phase identification is achieved by locking the oscillation to an external reference oscillation through the "locking" port. All timings of the memory operations can be identified with locking to the external reference oscillation.

3 Experimental results

The experimental setup used to confirm the feasibility of this proposal is shown in figure 2. The ring generating the multistable oscillations was a hybrid electro-optical ring resonator, essentially consisting of a Fabry-Perot(FP) laser diode (LD), an E-O intensity modulator with waveguide Mach-Zehnder structure, a 1000m single-mode optical fiber delay line, PIN photo diode for 1.3μm optical communication and high speed video amplifiers with 3dB bandwidth from DC to more than 150MHz [5]. The active nonlinear element was the combination of LD and E-O modulator. The E-O modulator had a sinusoidal E-O modulation characteristic. In this experiment we set the effective delay $T_r/T_m \approx 124$ ($T_r \approx 5.2\mu$sec, $T_m \approx 42$nsec) by introducing a low pass filter at the output port of the first stage video amplifier. For the "in" coupler we used an optical coupler with a splitting ratio of 90:10, while the other couplers in figure 1 were substituted with electrical power dividers as shown in figure 2.

The ring resonator was pumped by the LD with constant optical power. The class of $(n, 2)$ modes could be selected and phase-locked to an external reference oscillation by injecting into the loop a small amplitude sinusoidal signal at a frequency near the carrier frequency, $n/(2T_r)$. For the (21,2) modes shown in figure 3, the LD pump power was 0.76mW. The frequency and amplitude of the external reference oscillation were set to be 1.99566MHz and 0.5% of the amplitude of the oscillation in the loop, respectively. The locking range under the above mentioned condition was about 0.023% of the free running frequency of the (21,2) mode. The range increased in proportion to the amplitude of the injected reference signal. Different modes in the (21,2) mode class were found to have almost identical locking ranges. With this locking technique, we could obtain phase stability and identify the first bit of the cyclic 42-bit memory pattern.

Figure 3 shows an example of "write", "read" and "erase" of 21-bit binary data. One of the memory states, the one corresponding to all "0" is used as an initial state for "write" operation. This state can be reached from any other memory state with the "erase" operation described below.

In the experiment, another 1.3μm FP LD, directly driven by an arbitrary function generator, was used to generate the "write" signal, a 21-bit RZ binary optical pulse

train of length $2T_r$. The "write" signal was injected through the optical coupler. The optical power of the "write" pulses injected into the loop was 0.024mW. When injected with the correct timing, the "write" pulses are superposed on the low "0" peaks of the initial state oscillation in the loop, as shown in figure 3(a).

In the "read" operation of the experiment, the peak levels of the electrical oscillation signal output from the electrical stage of the ring are thresholded midway between the "1" and "0" levels to obtain a cyclic 42-bit RZ pulse sequence of period $4T_r$ (21-bit RZ pulse sequence of length $2T_r$, followed by the inverted 21-bit RZ pulse sequence of length $2T_r$), as indicated in lower waveforms of figure 3.

In the test of "erase" operation, shown in figure 3(b), the same "write" signal as in figure 3(a) was injected with a delay of $2T_r$ with respect to the first bit of the 42-bit cyclic memory pattern so that it is added onto the inverted peak pattern to cancel the data in the memory. In a future implementation, the "erase" signal of length $2T_r$ could be extracted with an optical thresholder and gate from the optical "read" signal.

In the "write" and "erase" operations shown in figure 3, the RZ pulse height and width of "write" (or "erase") signal injected in the loop were about 0.024mW of optical power and 50% of duty ratio, respectively, which roughly corresponded to the difference between high and low peaks of the (21,2) oscillation waveform in the loop. With the optimum pulse height and width, the waveform quickly settled to the destination memory state with little transient as shown in figure 3. However, some variation of the pulse height and width could be tolerated, due to the dynamical stability of the oscillation mode. Figure 4 shows a typical example of the region of the pulse height-pulse width space in which the "write" operation for a 21-bit pattern could be reliably executed. The shape of the region showed that the narrower the pulse width the larger the pulse height. Though there were small differences in the region for "write" and "erase" of the same bit pattern and there was a small dependence on bit pattern, it was found that for all the bit patterns examined the area around 0.024mW pulse height and 50% pulse width was suited to reliable "write" and "erase" operations.

4 Conclusion

We have made a new proposal of novel loop memory and experimentally confirmed the basic functions, "write", "erase" with optical pulses and "read", for the memory system to show the feasibility of our proposal. The bit capacity of the memory can be increased by increasing the effective delay T_r/T_m [5].

High-speed all-optical operation of the loop memory is an important target. The key factor for realizing a practical all-optical implementation is a fast, large nonlinear response achievable with a low optical power, e.g. diode laser power. Recent experiments on nonlinear switches suggest that a promising approach is to use the optical Kerr effect in optical fiber pumped by a laser diode [7][8]. The response of the Kerr effect is fast ($T_m < 10^{-14}$sec) and the long interaction length and optical power concentration in a fiber switch make it possible to obtain a sinusoidal type input-output intensity relationship with a low optical power of order milliwatts or less [7][8].

References

[1] K.Ikeda, "Multiple-valued stationary state and its instability of the transmitted light by a ring cavity system," Opt. Commun., vol.30, pp.257-261, Aug. 1979.

[2] K.Ikeda and K.Kondo, "Successive higher-harmonic bifurcations in systems with delayed feedback," Phys. Rev. Lett. vol.49, pp.1467-1470, Nov. 1982.

[3] K.Ikeda and K.Matsumoto, "High-dimensional chaotic behavior in systems with time-delayed feedback," Physica 29D, pp.223-235, 1987.

[4] P.Davis and K.Ikeda, "Switching between multistable oscillations and applications in signal generator and memory," Technical Digest of the 16th International Conference on Quantum Electronics, ThC-3, pp.634-635, Tokyo, Jul. 1988

[5] T.Aida and P.Davis, "Experimental demonstration of novel dynamical memory function in a nonlinear elecro-optical ring resonator," Jap. J. Appl. Phys. vol.29, pp.L1241-L1243, Jul. 1990.

[6] S.Kuroyanagi, T.Shimoe and K.Murakami, "Photonic ATM switching network," in Tech. Dig., Intern. Topical Meet. Photonic Switching, Kobe, Japan, Apr. 1990, paper 14B-2, pp.223-225

[7] I.H.White and R.V.Penty, "Demonstration of the optical Kerr effect in an all-fibre Mach-Zehnder interferometer at laser diode powers," Electron. Lett., vol.24, pp.340-341, 1988

[8] D.J.Richardson, R.I.Laming and D.N.Payne, "Very low threshold Sagnac switch incorporating an erbium doped fibre amplifier," Electron. Lett., vol.26, pp.1779-1781, Oct. 1990

Figure captions

Figure 1 Configuration of the loop memory

Figure 2 Experimental setup

Figure 3 Example of (a)"write" and (b)"erase" of 21-bit sequence of '100111000011111000001' where signal levels indicated are those of optical powers in the fiber loop

Figure 4 Regions of the pulse height-pulse width space for reliable (a)"write" and (b)"erase" of 21-bit sequence of '100111000011111000001'; No transients in "read" signal were observed in the dark-shaded zone; Transients of a few T_r in length were observed in the light-shaded zone

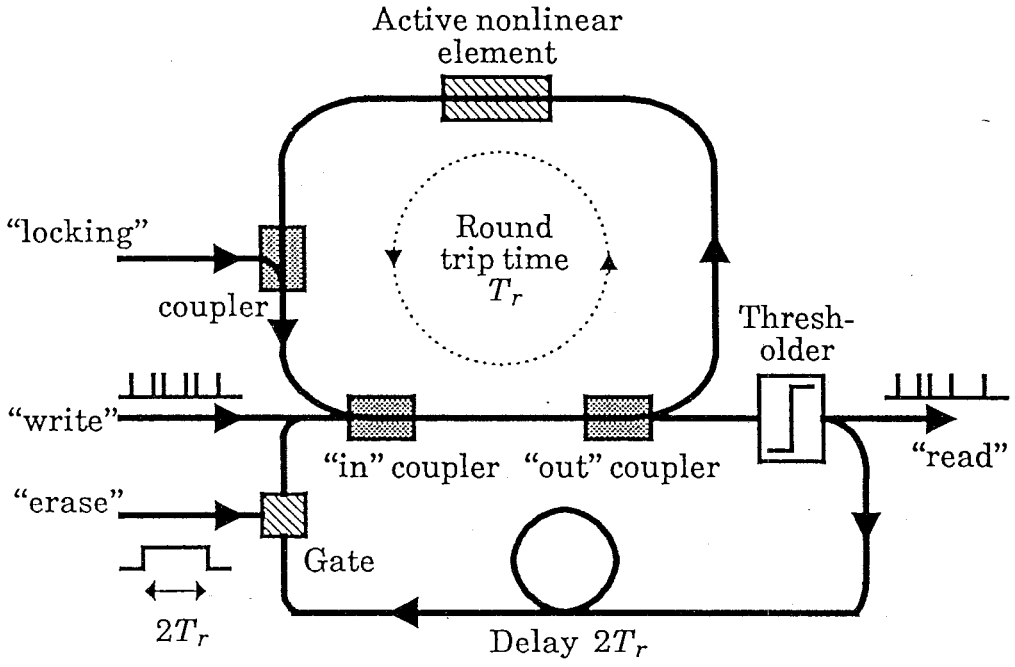

Fig.1 Configuration of the loop memory

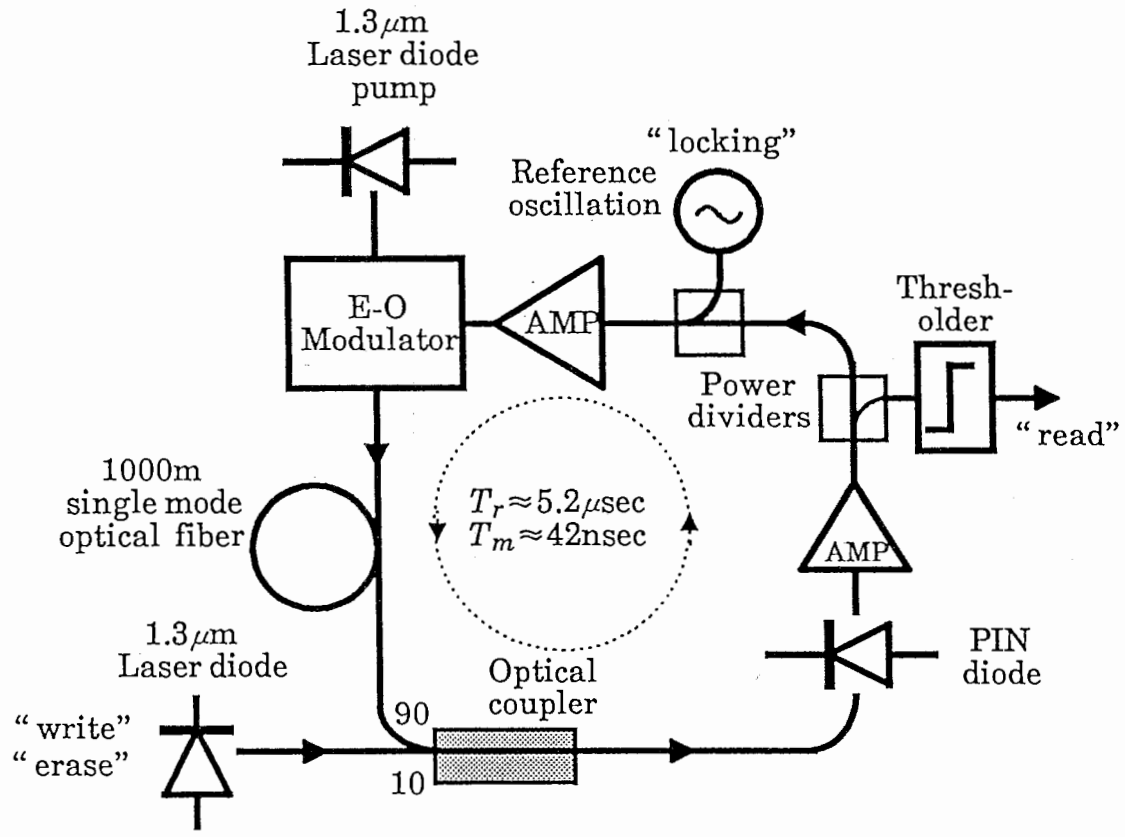

Fig.2 Experimental setup

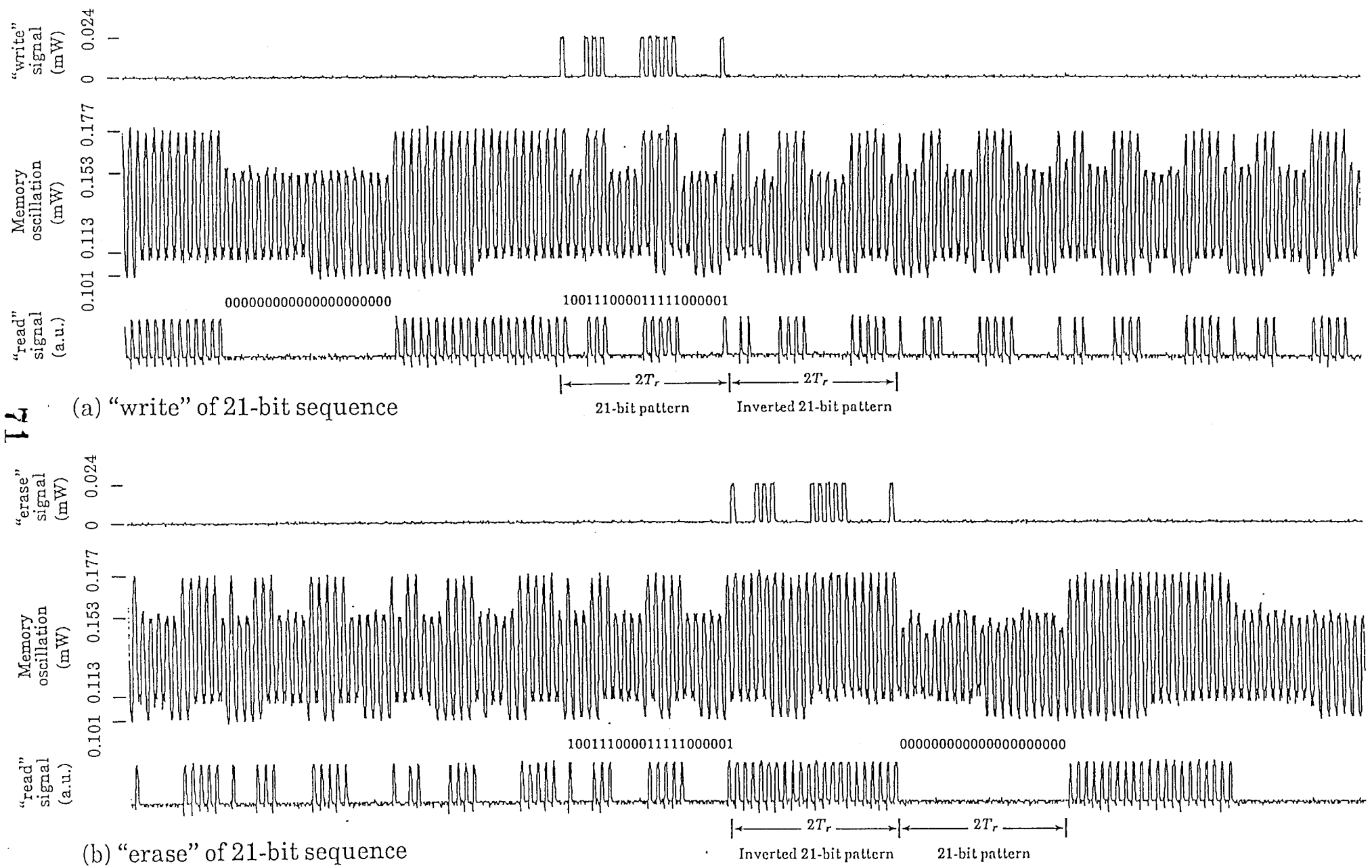

Figure 3 Example of (a)"write" and (b)"erase" of 21-bit sequence of '10011100001111100001' where signal levels indicated are those of optical powers in the fiber loop

(a)

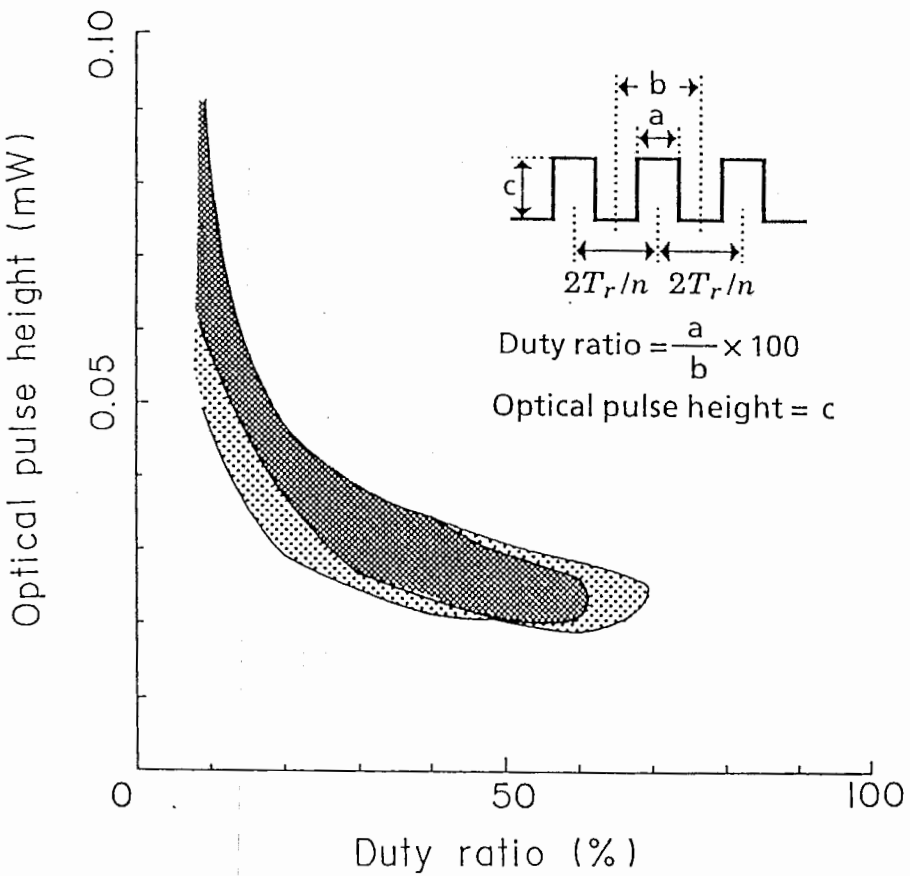

Figure 4 Regions of the pulse height-pulse width space for reliable (a)"write" and (b)"erase" of 21-bit sequence of '100111000011111000001'; No transients in "read" signal were observed in the dark-shaded zone; Transients of a few T_r in length were observed in the light-shaded zone

(b)

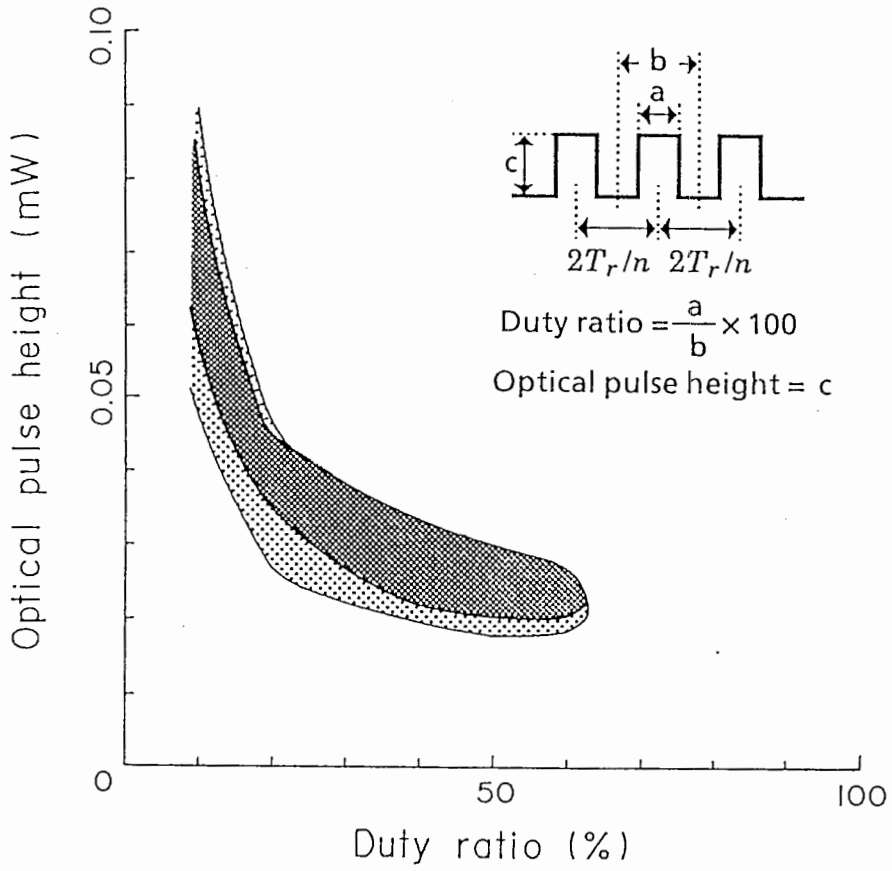

"erase" : 10011100001111100000 1

Chapter IV

Oscillation Mode Selection using Bifurcation of Chaotic Mode Transitions in A Nonlinear Ring Resonator

Abstract

This paper demonstrates the effectiveness of an adaptive parametric control method for searching and switching among a large number of multistable oscillation modes using chaotic mode transitions. The adaptive control is used to select nonlinear oscillation modes in an electro-optic ring resonator. In the adaptive control scheme, the result of a simple test of resonator output is fed back to a single parameter, pump laser power, governing bifurcation to and from chaos. The test is the presence or absence of a target code in the oscillation waveform of the resonator output. Chaotic mode transition phenomena, called chaotic itinerancy, are investigated in terms of code dynamics, and the results are used to determine the optimal parameters for the adaptive control.

1 Introduction

The ability of nonlinear devices with only simple structure to generate very complicated behaviors, such as chaos, is well known. However, this ability has not been exploited in technological applications of devices. This paper addresses this issue. We demonstrate that onset of chaos can be exploited in a device which interacts, in a "trial and error" manner, with its environment to find a suitable mode of operation.

Theoretical and experimental studies on nonlinear delayed feedback systems have shown the existence of a large variety of multistable bifurcated oscillation modes leading to chaos [1]-[7]. Ikeda *et al.* [5] clarified the hierarchical tree structure of the bifurcation of the oscillation modes excited in a nonlinear optical ring cavity and suggested the applicability of the multistable modes for memory. It has been theoretically proposed that selective excitation of modes, useful for optical signal generation and memory, is possible by two complementary methods, seeded switch [8] and chaotic search [9].

The seeded switch is a direct, deterministic selection of a mode by injection of a signal close to the mode (i.e. content addressing). The seeded switch was experimentally demonstrated in an electro-optic (E-O) hybrid nonlinear resonator and availability of the multistable modes for the generation and storage of binary optical pulse sequences was confirmed [7][10].

Chaotic search is an approach to selection of mode, which is complementary to selection by seeding and results in stochastic selection of a mode which satisfies a given constraint. A method has been proposed for chaotic search which uses adaptive parametric feedback control of bifurcation to and from chaos to search for and select a mode which satisfies the given constraint [9][11]. In this paper we shall refer to this method to "CS" for short. CS corresponds to access to modes from an upper chaotic stage of the hierarchical mode bifurcation tree, while the seeded switch is access from a lower [7] or same [10] stage.

The validity of the proposal for chaotic search by adaptive bifurcation was experimentally demonstrated in an E-O hybrid nonlinear resonator, which gave a concrete image to the applicability of chaos [11].

This paper gives the details of the experiment and quantitative investigations of CS, relevant to characterization of chaotic mode transitions, control parameters

and switch time. In particular, we consider the above mentioned factors from the practical viewpoint of tuning the CS. We explain how parameters can be tuned to reduce the CS time and what factors determine the lower limit of the CS time.

In section II we first review the general idea of CS. In section III we describe the oscillation modes of the nonlinear ring resonator, and coding which is applicable to waveforms of multistable modes and chaotic modes. In section IV we present chaotic mode transitions observed as code dynamics, where we can grasp the dependence of mode transitions on the control parameter. In section V we discuss how to use the results of section IV to choose parameters for adaptive control of bifurcation, and present data from experimental trials of CS. In section VI we examine the relations between chaotic mode transitions, control parameters and switching time, giving the optimum conditions for the adaptive parametric control.

2 Principle of chaotic search

The method of adaptive mode selection using bifurcation to chaos was proposed by Davis [9]. The method is complementary to direct mode selection by parameter in monostable systems or by seeding (content-addressing) in multi-stable systems. In contrast to direct mode selection, this type of mode selection will be useful when a device has to operate autonomously.

The key idea is that an optical device which is capable of supporting a variety of modes and chaotic transitions among them could interact with its environment in a trial and error manner in order to find a suitable mode of operation. According to the method proposed, chaotic transitions allow the device to sequentially try each of the modes to test whether they are suitable or not. An external feedback signal indicating that a mode is suitable is used to stabilize the mode by changing a parameter and taking the device into a multistable regime where all the modes are stable.

It has been argued [9] that this method should be generally applicable when there are responses from the environment which indicate whether the current device output is satisfactory or not, and where there is one parameter bifurcation of the device state from a multistable mode regime to a regime where there is intermittent transitions among modes.

The onset of intermittent transitions among modes allows the modes to be tested

in turn. Intermittent transitions among modes can occur if chaos appears via basin merging and chaotic paths are created between the "attractor ruins" of the previously stable modes [5][12]. In the context of transitions among multiple modes in high dimensional systems such transition sequences have been referred to as "chaotic itinerance" [11][13]-[15]. To ensure that each candidate mode is accessible to the search and selection process, it is necessary that the chaotic itinerance repeatedly visits each and every one of the mode neighborhoods.

This method of adaptive mode selection has some similarity with a method recently proposed by Ott, Grebogi and Yorke [18] [19] for selecting a periodic orbit from a chaotic attractor. Each uses chaos to search the phase space, and also each uses feedback to a single parameter. However, the adaptive mode selection described in this paper is concerned with bifurcation of stable candidate modes to and from a chaotic attractor. Moreover, it is concerned with an external test of the current state which may be arbitrary and not specifically related to internal dynamical structure such as basin structure.

3 Oscillation modes and coding

In this section we describe the nonlinear oscillation modes of the ring resonator which will be the subject of the mode selection experiment. The nonlinear ring resonator used for the present experiment is the same electro-optic (E-O) hybrid ring resonator as was used in a previous experiment [7] where modes corresponding to multi-bit binary codes were selected by seed injection. Moreover, we use one of the same sets of modes, the twice-bifurcated 7-th harmonic modes. The modes are assigned two types of codes for identification. One of the codes, a non-specific "feature" code, will be used as target in mode selection. [1]

3.1 modes of nonlinear ring resonator

The nonlinear resonator used for the experiment is an E-O hybrid ring resonator with very large effective delay [7], in which a large number of nonlinear oscillation modes are excited. In figure 1, the nonlinear ring resonator is illustrated with the coding and control circuits for the CS experiment.

[1] For ease of implementation and for the purpose of comparison, we used the same coding as previously used in computer experiments on the method [9].

The nonlinear ring resonator is modeled by the following delay differential equation [7],

$$T_m \frac{dV(t)}{dt} = -V(t) + V_o + \mu F(V(t - T_r)). \tag{1}$$

Here V is the signal in the loop, either the optical intensity in the fiber or the voltage on the EO modulator. V_o is an accumulated offset bias voltage at the final stage amplifier, μ is the bifurcation parameter proportional to the input optical power P_i from the laser diode (LD), and T_m and T_r are the response time and the delay time of the nonlinear feedback, respectively. The function F is the typical sinusoidal E-O modulation characteristic of an EO intensity modulator. A nonlinear characteristic with at least one hump or valley (maximum or minimum), and an effective delay, T_r/T_m, is needed to give delay-induced bifurcations to chaos as μ is increased. We are concerned with the case of large effective delay, $T_r >> T_m$, in which there are multistable modes useful for generation and storage of binary optical pulse sequences [7].

This hybrid electro-optic system acts also as a model for the dynamics of an all-optical implementation of equation (1), and so, in principle, the results of this paper are relevant also to all-optical signal generation and storage in future all-optic communication networks.

For low pump power (low input optical power from the LD), the oscillation modes which can be excited in the resonator are the fundamental mode of period T_1 of about $2T_r$ and odd (n-th) harmonic modes with period T_n equal to about $2T_r/n$. Each of these harmonic modes exhibits bifurcations leading to chaos with increase of pump power. The modes of the nonlinear oscillation can be classified with harmonic number n and bifurcation order m as (n, m) [5]. Figure 2 shows schematic bifurcation diagrams of oscillation level and oscillation mode.

In each (n, m) class there are multiple oscillation modes, "isomers", with different peak modulation patterns [5][7], which are all stable at the same value of pump parameter μ. As in [9], we shall represent isomers in an (n, m) class by the symbol $\xi_{n,m}$ and a particular isomer by $\xi_{n,m,L}$, where L is some distinguishing label. We denote by μ_m the value of pump parameter μ at which m-th order bifurcation occurs and each $\xi_{n,m-1}$ mode bifurcates into multiple $\xi_{n,m}$ modes.

Successive bifurcations reach onset of chaos at a certain point μ_F, and after the onset of chaos at μ_F there are order m^* "inverse" bifurcations [5]. In the inverse

bifurcations, the basins of the multiple chaotic modes merge together, resulting in fluctuations on peak and valley levels of the n-th harmonic carrier and intermittent transitions among different $\xi_{n,m}$ type oscillation waveforms.

In this paper we consider switching among isomers of $(n,2)$ class at $\mu_2 < \mu < \mu_3$ using chaotic mode transitions in $(n, m^* = 2^*)$ class at $\mu_{2^*} < \mu < \mu_{1^*}$. For the CS experiment, we set the effective delay $T_r/T_m \approx 124$ ($T_r \approx 5.2\mu$sec and $T_m \approx 42$nsec) and excite modes by pumping the nonlinear resonator with the LD at about 1mW [7]. A signal with the desired n-th harmonic carrier frequency was injected initially to excite the n-th harmonic class of oscillation [7].

3.2 coding

In this section we introduce a method for distinguishing between oscillation modes. Thresholding of the oscillating optical signal output can be used to generate characteristic binary pulse sequences [9]. The most natural coding of oscillation modes of $(n, m = 2)$ class is the binary sequence corresponding to the high and low peak levels. In the experiment we extract a binary $\boldsymbol{J}$ code from the peak modulation pattern in order to characterize oscillations. However, another code, called the feature R code is extracted, by a different sampling of the peak modulation pattern, for use in the search. Figure 3 shows the schematic diagram of the coding circuits used to extract $\boldsymbol{J}$ and R. Figures 4(a) and (b) show examples of signals which appear in the process of coding periodic and chaotic oscillations, respectively.

Signals are passed through thresholders and pulsewidth extenders so that oscillating signals, even the irregularly fluctuating chaotic signals, are converted into sequences of regular pulses. Timing for sampling of pulse sequences is determined by a clock signal, CLK, which is obtained from the harmonic carrier oscillation. Here we make use of the fact that in the chaotic states $\xi_{n,m=2^*}$ used for search, even though the peak modulation fluctuates, the carrier is quite stable.

Threshold level V_{th1} and pulsewidth extension T_r/n are chosen to obtain a pulse sequence $S_1(t)$ from which the $\boldsymbol{J}$ code is obtained. The $\boldsymbol{J}$ code is the n-bit binary sequence corresponding to the first n consecutive binary pulses of signal $S_1(t)$ in each interval $2T_1 \approx 4T_r$, and is updated at a rate of $2T_1$ interval.

Threshold level V_{th1} and pulsewidth extension $3.5T_r/n$ are used to obtain sequence $S_2(t)$ for the R code. R is the number of pulses of signal $S_2(t)$ in a long

interval $T \approx 20T_r$, and is updated at a rate of T interval. The R code can be thought of as a measure of the anti-bunching of the "1"s in the $\boldsymbol{J}$ code sequence, and was chosen simply because it is easily implemented and separates the modes into different classes.

In figure 5 the ten multistable isomers of $\xi_{n=7,m=2}$ mode, labeled by mode number p as $\xi_{7,2,p}$, $(p = 1 \sim 10)$, are shown. The mode coding is summarized as follows. All the isomers of the $\xi_{7,2}$ mode can be completely identified by assigning 7-bit code $\boldsymbol{J} = (J_1, J_2, \cdots, J_7)$ [7]. With phase identification, for example as is possible with locking of the carrier to a reference clock signal, there are 128 (2^7) distinguishable modes, labeled as $\xi_{7,2,\boldsymbol{J}}$. Without phase identification these 128 modes degenerate into the ten isomers shown and labeled by mode number p in figure 5. The feature R of the stable $\xi_{7,2,p}$ modes takes four discrete values of {20, 25, 30,35}, thus ten $\xi_{7,2,p}$ modes are categorized into four $\xi_{7,2,R}$ sets of modes by the R code. Some further details about the coding are summarized in the appendix.

4 Chaotic mode transitions

With increase of μ (proportional to input optical power), peaks and valleys of waveform of $\xi_{n,2}$ mode oscillations of the type shown in figure 5 begin to fluctuate, leading to chaotic $\xi_{n,2}$- mode oscillations involving transitions among $\xi_{n,2}$ isomer patterns. The global character of the transitions can be seen in the transition matrices shown in figure 6. Oscillations near to each and every one of the $\xi_{n,2}$ modes appear repeatedly in a single chaotic time series. The transition matrix for the $\boldsymbol{J}$ code shows clearly that transitions tend to take place by change in one peak level at a time, as in a random walk on an n-dimensional hypercube. In this section we look mainly at the transitions among $\xi_{n=7,m=2}$ modes in terms of the non-specific, feature R code, since this is the code we shall use in the adaptive mode selection in the next section. We consider the sequences of codes generated and characterize the dynamics by residence time statistics and absence time statistics for each R value. We emphasize that the use of the R code means that we are looking at a low dimensional projection of dynamics in which multiple modes are only distinguished in classes, and the statistics for mode transitions reflect averages over multiple modes.

4.1 parameter dependence of mode transitions

Figure 7 shows waveforms and R dynamics during bifurcation from $\xi_{n=7,m=2}$ to $\xi_{n=7,m^*=2^*}$ mode oscillations in the range $\mu_2 < \mu < \mu_{1^*}$. Increasing degrees of chaos accompanied by mode transitions can be observed in the R variations.

Initially (figure 7(a)) the system is below the onset of chaos, in one of the stable modes with the feature value $R = 30$, and R remains constant at 30. When μ exceeds μ_{2^*}, mode transitions appear in R dynamics, as shown in figure 7(b). With further increase in μ above μ_{2^*}, the change in R value became faster, as shown in figures 7(c)(d) $\cdots$ (f). This shows that the rate of mode transitions between isomers increases with increase of the degree of chaos. As can be seen from the figures 7(b)(c) $\cdots$ (f), in this range even a small change of order 0.1% (1μW) of input optical power P_i affects the mode transition dynamics.

Near μ_{2^*}, oscillation waveform retained distinctive features of $\xi_{7,2}$ mode (figures 7(b)$\sim$(f)) and the values of R concentrates mainly on the values for isomers of $\xi_{7,2}$ mode, $R \in \{20, 25, 30, 35\}$. This tendency is reflected in "visiting ratio", proportion of time spent at each R value. Figure 8 shows the distribution of the visiting ratios of R values for figure 7(f). The distribution has peaks at values of R corresponding to the isomers, $R \in \{20, 25, 30, 35\}$. As μ increases further, the tendency for dwelling near the previously stable modes decreases. For larger values of μ, R values showed a tendency to spread to higher values (figures 7(g)(h)) and then, for μ near μ_{1^*} concentrate within a narrow range near the maximum value of $R = 35$ (figure 7(i)).

This is because as μ increases, the chaotic degree of the oscillation increases and the peaks swing large and fissure into multiple peaks, increasing the probability of a crossing of the threshold level V_{th1}. As the result, most of the binary pulse sequences generated take the '1' level, giving a concentration of R near $R = 35$.

4.2 residence and absence time distributions

The nature of chaotic mode transition can be characterized by residence time and absence time distributions. Examples of histograms of residence times obtained from a single chaotic time series are shown in figure 9. The distributions are monotonic decreasing with time. The distributions typically have a dominant exponential part with a long time tail. Due to the long time tail, care must be taken in rigorously defining an average or typical time. However, from a practical point of view, we

are working far enough above the bifurcation point so that the exponential part dominates and we found the averages of these distributions are useful estimates, and in particular are useful for the tuning of chaotic search, as explained in the next section.

Escape probability $P_e(\mu; \xi_{n,m,L}, t)$ has been introduced [9] as the probability that an oscillation escapes the neighborhood of the $\xi_{n,m,L}$ mode within a time t. A long average residence time at a mode corresponds to a small probability of escape from the mode.

Figures 10 and 11 show the distributions of average residence time $< \tau_R >$ and average absence time $< \tau_A >$ of each R value and their dependence on parameter μ, respectively.

The average residence times of $R \in \{20, 25, 30, 35\}$, which at lower μ corresponded to stable modes, are long, while those of other values of $R \notin \{20, 25, 30, 35\}$, are at most one count of $T \approx 20T_r$, independent of μ. This means that oscillation often dwells at or near a mode for some time before making a typically quick transition to another mode in time T or less. As is shown in the figure 10, the smaller the μ, the longer the residence time $< \tau_R >$ for $R \in \{20, 25, 30, 35\}$. Below the onset of chaos at μ_{2^∞}, $< \tau_R >$ becomes infinite for $R \in \{20, 25, 30, 35\}$ corresponding to the stable modes (figure 7(a)).

Absence time is the time between appearances of a code value. Figure 11 shows the distribution of average absence time $< \tau_A >$. The absence time for feature values corresponding to destabilized modes, $R \in \{20, 25, 30, 35\}$, is shorter than for other values. Though there is some dependence on R, in general the smaller the parameter value μ, the longer the average absence time $< \tau_A >$ of $R \in \{20, 25, 30, 35\}$.

The experimental results presented here combine to give a characterization of the phenomenon of "chaotic itinerancy" in this system whereby oscillations move around in the phase space, visiting and dwelling for some time at or near around a remnant mode, the "ruins" of an attractor corresponding to a stable oscillation mode, and then moving to another. It is significant to note that the phenomenon described here is robust, in the sense that the statistics of the itinerancy are reproducible. In the next section, we use this chaotic itinerancy to search for modes in an adaptive mode selection scheme. The reproducibility of the itinerance statistics is essential to the applicability of this phenomenon for adaptive mode selection.

5 Adaptive bifurcation control for chaotic search

It was confirmed from the observation of chaotic itinerancy in the previous section that there is a practical parameter range where intermittent chaotic mode transitions occur persistently among all the $\xi_{7,2}$ mode isomers. In this parameter range the rate of chaotic mode transitions among $\xi_{7,2}$ mode isomers can be simply controlled by parameter μ. The adaptive parametric control for the "CS" search scheme is based on this property of the chaotic mode transitions [9]. Namely, if the current mode is not satisfactory parameter μ is increased above $\mu > \mu_{2*}$ to where isomers will appear one after another in chaotic itinerance, and when a satisfactory mode appears, μ is decreased so that the satisfactory mode becomes stable.

In this section, we describe the control scheme and how to choose and tune control parameters for CS based on the observations of chaotic mode transitions in the absence of control.

5.1 adaptive parameter control scheme

In the CS experiment, a mode is judged to be satisfactory or not according to its R code. The adaptive control of parameter μ, the LD power, is described by the following equation,

$$T_g \frac{d\mu}{dt} = -\mu + G(E). \tag{2}$$

Here, $E = |R - R^c|$ is a scalar feedback signal which is a measure of the mismatch between an externally specified feature value R^c and the feature value R measured in the previous T interval. E is updated at the end of each T interval. T_g is the response time for varying μ. $G(E)$ is a monotonic increasing sigmoid type function of E, bounded below and above as $\mu_2 < G(0) < G(\infty) < \mu_{1*}$. Figures 12(a) and (b) are the shapes of $G(E)$ functions, respectively used for multi-mode localization and single-mode selection. These functions are characterized by three parameters - Δ, the boundary value of E distinguishing between satisfactory and unsatisfactory outputs, $G(0)$, the value of μ for satisfactory output, and $G(\infty)$, the value of μ for unsatisfactory output.

For the control scheme, the parameters of function $G(E)$ and the value of T_g are the key factors which determine the efficiency of CS, as quantified for example by the search time. Next we show how these parameters can be chosen on the basis of

the experimental data for the chaotic mode transitions, introduced in the previous section, figures 7, 10 and 11.

For multi-mode localization the $G(E)$ function shown in figure 12(a)) is used. The minimum value $G(0)$ is set slightly above the onset of mode transitions of R dynamics μ_{2^*}. The maximum level from $G(6)$ to $G(\infty)$ is set at a saturation level μ_s where R values for all the isomers of $\xi_{7,2}$ mode, $R \in \{20, 25, 30, 35\}$, appear as evenly and as often as possible - for example the value μ_{medium} in figures 10 and 11 corresponding to the dynamics in figure 7(f).

In contrast, for single-mode selection the $G(E)$ function in figure 12(b) is used. The minimum value $G(0)$ is set at a value, μ_o, below the onset of chaotic mode transition. The value of $G(\Delta)$, where $\Delta = 5$ is the minimum difference in R values between different $\xi_{7,2}$ modes, is set above the onset of the mode transitions at μ_{2^*}. The level from $G(6)$ to $G(\infty)$ is set at the same saturation level μ_s as for the muli-mode localization case.

Using residence time distribution data, the response time T_g can be chosen so that parametric control of equation (2) reacts to dwellings near modes rather than to transients during transitions between modes. As is shown in figure 10, the residence time at or near isomers, $R \in \{20, 25, 30, 35\}$, is several T ($T \approx 20T_r$), while that of other values of R is about T, independent of μ. From these observations we first set T_g at about T. We check the dependence of search performance on T_g later.

5.2 multi-mode localization test

First, we do a rough demonstration of the CS parametric control of equation (2) using the $G(E)$ function of figure 12(a) where the minimum is slightly above μ_{2^*}, the onset of mode transitions. The effect of the control of equation (2) is seen in figure 13.

When there is no control, the visiting ratio is roughly independent of J code value, as shown in figure 13(a). When the parametric control is activated, there is a localization of oscillation in modes with the target feature value $R = R^c = 30$, as seen in the increase of the visiting ratios in figure 13(b).

This roughly confirms the validity of the control scheme defined by equation (2). The rate of escape from a mode is maximum when there is a large mismatch E between R and R^c. Conversely, when the mismatch E is small, the mode escape rates

decrease, the typical residence times are longer, and this results in a localization of oscillations in modes where E is small.

5.3 single-mode selection test

When the $G(E)$ function of figure 12(b) was employed with minimum value set below the onset of mode transitions, eventually the oscillations converge to a single mode, one of the modes whose feature value is equal to the target value $R = R^c$.

Figure 14 shows an example of search and selection of mode with $R = R^c = 25$. The adaptive parametric control is activated at the time marked with (a). The oscillation mode settles to an isomer of $\xi_{7,2,R=25}$ mode at the point marked with (c). Figures 15(a),(b) and (c) show expansions of the time series at the points marked with (a),(b) and (c) in figure 14. Similar behavior was observed for the other choices of target feature value in the set $R \in \{20, 25, 30, 35\}$.

Switching of target value results in a transient search period during which the system bifurcates in and out of chaotic itinerancy until eventually a mode with the target value is trapped. Repeatedly changing the target feature value, we observed that any of the multiple $\boldsymbol{J}$ codes corresponding to each target feature value had a chance of being selected.

Typically there is bifurcation in and out of chaos a number of times before convergence to a stable mode. This is due to the fact that the external test is an arbitrary one, in the sense that outputs with the target feature value are not necessarily in the basin of attraction of an oscillation with the target feature value when μ_s is reduced. This can be thought of as a partition mismatch - a mismatch between the internal partition determined by the mode basin structure and the external partition of the space of waveforms defined by the external responses to the output. We expect the existence of such a mismatch to be common for complex adaptive devices in general, and this is why we chose a non-specific feature code as the mode selection criterion [9].

6 Repeated CS and search time statistics

Since chaotic dynamics are used in the search for an appropriate mode, characteristics of the search, such as search time, are stochastic quantities, and require

statistical description. We used the following "repeated CS method" to make a statistical evaluation of the time required for single-mode selection.

First, we interrupt the control feedback in such a way that E, and hence μ, is large and constant for a time, called the "ERASE interval", during which the oscillation is chaotic and, typically, the memory of the mode selected in the previous trial is lost. Then the feedback control is reconnected and search allowed to take place for a time, called the "SEARCH interval". We repeat this procedure of the combination of ERASE interval and SEARCH interval periodically by using a square wave interruption signal.

Figure 16 shows an example of the repeated CS for $R^c = 25$ when T_g is set at $0.865T$ ($\approx 17.3T_\tau$). The time series of error $E = |R - R^c|$ and feature R are indicated. The period of repeated CS is 100msec, 50msec for each ERASE and SEARCH interval. An ERASE interval of length 50msec ($\approx 9615T_\tau \approx 481T$), being much longer than the average residence and absence times, was usually long enough to erase the memory of the mode selected in the previous SEARCH interval. Note that the chaos in the ERASE intervals is that of μ_{medium} in figures 10 and 11. CS is judged to succeed in a SEARCH interval if E settles to zero within the SEARCH interval. In this particular example of repeated CS, CS time for 90% success rate was estimated at less than 50msec.

Figure 17 shows the dependence of the CS time for 90% success rate on T_g. Too large T_g makes the response of the adaptive parametric control slow and oscillations tend to escape from the mode neighborhoods before μ decreases enough to trap them there. On the other hand, when T_g is too small, the adaptive parametric control responds to fluctuations of R during transitions between $\xi_{7,2}$ modes. The valley in the times shown in figure 17, shows the existence of an optimum value of T_g in the range between $0.3T$ and T. The optimum value of T_g is less than the minimum residence time in the R coding scheme. This reflects the fact that the typical time for transitions between neighborhoods of $\xi_{7,2}$ modes is less than T.

Figure 18 shows success in finding a mode with target feature value $R = 25$ as a function of search time. The data was obtained from about 300 periods of repeated CS. Curve (a) shows the probability of converging to a mode with the target feature value under CS control of equation (2). For comparison, curves (b)$\cdots$(e) show statistics for unconstrained (ie. free-running, with control loop open) chaotic itiner-

ancy at μ_s, namely, the probability of having had a residence time of length (b) $1T$ ($T \approx 20T_r$), (c) $5T$, (d) $10T$, (e) $20T$. All the curves approach 100% asymptotically, although there is a fall off in rate of increase in success which corresponds to the long-time tail seen in the residence and absence time distributions.

That curve (a) is above curves (d) and (e) shows that trapping with the adaptive control is effective. Curve (b) is the upper bound on search performance. It is the performance expected if a mode with the target feature value is trapped as soon as the target feature value is encountered in the itinerancy. Typically this does not happen due to the partition mismatch described above - outputs with the target feature value are not necessarily in the basin of attraction of an oscillation with the target feature value when parameter μ is reduced.

Tuning of the CS parameters for optimum performance corresponds to choosing the value of μ_s to maximize the rate of mode transitions as seen in the curves (b) to (e), and choosing T_g to bring curve (a) as close as possible to curve (b).

With optimal tuning, we found the time expected for 90% success in mode selection was around $350T$ (36msec), roughly an order of magnitude larger than the lower limit determined by the dynamics of the unconstrained chaos, the average absence time of a target mode at μ_s (see figure 11).

A number of factors affect the optimal value. Most significant factor is the choice of test criterion, which determines, for example, the mismatch between E values and mode basin structure. Another is environmental noise. Little is know yet about the effect of noise on chaotic itinerancy among multiple modes. As seen from the long time tails in the residence and absence time distributions, occasionally the search dynamics get caught in some places for exceptionally long times. The presence of some system noise could help escape from such traps. On the other hand, too much noise could interfere with the chaotic itinerancy if the chaotic itinerancy is taking place through narrow dynamical passageways in the phase space. This is a topic for more work in the future.

7 Conclusion

In this paper, we have experimentally tested a method [9] which makes positive use of chaos for adaptive selection of modes in a nonlinear ring resonator.

In the experiment reported in this paper, we tested that the method works in

a practical physical system - an electro-optic circuit useful for repetitive generation of binary optical pulse sequences [7]. The multiple modes correspond to generation of different multi-bit pulse sequences. A scalar signal indicating the results of an external test of generated pulse sequences is fedback to determine power of the LD source of mW light.

The effectiveness of the method was seen in the statistics of mode search time - the time for convergence to a satisfactory mode. In the particular case studied, we found the likelihood of search success seemed to approach asymptotically with time to 100%, with 90% success achievable within several thousands of mode periods.

We looked at the dependence of search time on control parameters, and on the relation between search time and statistics of mode transitions in unconstrained chaotic itinerancy. We showed simple guidelines for tuning for optimum search performance, based on the statistics for unconstrained chaos, such as residence time and absence time distributions. In particular, we showed that there is an optimum value of laser power above onset of chaos which corresponds to a trade-off between convergence to and divergence from neighborhoods of candidate modes. There is also an optimum value of rate of response of change of laser power, which corresponds to a trade-off between waiting for attraction into the neighborhood of a satisfactory mode, and trapping the oscillation before it escapes the neighborhood.

The particular values for optimum performance are expected to depend on the type of mode classification effected by the external test. For example, in the non-generic case where the classification of waveform in terms of external test results corresponds exactly to the basins of attraction of the modes it would not be necessary to wait for the chaotic itinerancy orbit to visit the close vicinity of a mode. However, usually there will be a mismatch between the external mode classification and the internal mode basin structure, and it may be necessary to do trial and error many times until a target mode is trapped, resulting in search time which is long compared with mode period.

From the device application point of view, the experiment showed that the method is feasible in an opto-electronic circuit if the laser power is stable to order 0.1%. It remains to be seen whether design of nonlinearities in the circuit could increase the tolerance to laser power fluctuations, for example by increasing the separation between multistable regime and the optimal chaotic itinerancy regime.

Appendix

Here we summarize the coding of $\xi_{n,m=2}$ mode oscillations.

Let us sample peak levels of oscillation $V(t)$ to project the oscillation on N dimensional vector sequence $\boldsymbol{V}^N(t)$ at discrete times t_k as,

$$\begin{aligned} \boldsymbol{V}^N(t_k) &= \{V(t_k-(N-1)\tau), V(t_k-(N-2)\tau), \cdots, V(t_k-\tau), V(t_k)\}, \quad (3) \\ t_k &= t_0 + k\sigma\tau, \quad (k=0,1,2,\cdots), \\ \tau &= T_1/n \approx 2T_r/n, \end{aligned}$$

where t_0 is a sampling phase and σ is a constant integer number. An N dimensional binary vector sequence $\boldsymbol{J}^N(t_k)$ is obtained from equation (3) by discriminating with respect to a threshold level V_{th} as

$$\boldsymbol{J}^N(t_k) = \{X(t_k-(N-1)\tau), X(t_k-(N-2)\tau), \cdots, X(t_k-\tau), X(t_k)\}, \quad (4)$$

where $X(t) = 1$ for $V(t) \geq V_{th}$ and $X(t) = 0$ for $V(t) < V_{th}$.

Now we can choose t_0 and V_{th} so as to obtain a binary sequence corresponding to sequence of high and low peak levels of stable $\xi_{n,m=2}$ modes. t_0 is adjusted so as to sample peaks, and V_{th} is set between high and low peak levels.

Now for the $\xi_{n,m=2}$ modes we shall use the facts that,

$$\boldsymbol{J}^N(t_k + T_1) = \overline{\boldsymbol{J}}^N(t_k), \quad (5)$$

and

$$\boldsymbol{J}^N(t_k + 2T_1) = \boldsymbol{J}^N(t_k), \quad (6)$$

where the bar indicates an inverted binary sequence. Hence, we characterize a mode by a binary vector code for the waveform of length $T_1 \approx 2T_r$, by taking $N = n$. Replacing $X(t)$ with binary labels $J_i = 0$ or 1, equation (4) is re-expressed as the code

$$\boldsymbol{J} = (J_1, J_2, \cdots, J_n), \quad (7)$$

The $\boldsymbol{J}$ code for $\xi_{n,m=2}$ modes is followed by the inverted code $\overline{\boldsymbol{J}}$ in the next $T_1 \approx 2T_r$ interval, and the code sequence of $\boldsymbol{J}$ and $\overline{\boldsymbol{J}}$ repeats with period $2T_1 \approx 4T_r$ [7]. Taking $\sigma = 2n$ results in a constant $\boldsymbol{J}$ output when in a stable $\xi_{n,m=2}$ mode.

As for the feature code, the R code of $\xi_{n,m=2}$ modes takes integer values from $5\,\mathrm{int}[n/2]$ to $5n$, where $\mathrm{int}[n/2]$ means round up integer value of $n/2$. This is easily

determined from the width of secondary pulses, $3.5T_r/n$, and the count interval, $10T_1 \approx 20T_r$. As the count interval is a multiple of the period, $2T_1$, of the stable $\xi_{n,m=2}$ modes, the output sequence of R values will be constant for these modes.

The coding processes described here mainly consist of thresholding, pulsewidth extension and pulse count. In the experiment we employed electronic circuits for the coding. However, it is also possible to execute these processes by using simple optical systems; an optical thresholder for the former, and an optical medium with long relaxation characteristic for the latter two which are intrinsically integration processes.

References

[1] K.Ikeda, "Multiple-valued stationary state and its instability of the transmitted light by a ring cavity system," Opt. Commun. , vol.30, pp.257-261, Aug. 1979.

[2] K.Ikeda and H.Daido, "Optical turbulence : Chaotic behavior of light from a ring cavity," Phys. Rev. Lett. vol.45, pp.709-712, Sept. 1980.

[3] M. W. Derstine et al, "Alternative paths to chaos in optical bistability", Phys. Rev. Vol. 27, pp.3200-3208, 1982.

[4] K.Ikeda and K.Kondo, "Successive higher-harmonic bifurcations in systems with delayed feedback," Phys. Rev. Lett. vol.49, pp.1467-1470, Nov. 1982.

[5] K.Ikeda and K.Matsumoto, "High-dimensional chaotic behavior in systems with time-delayed feedback," Physica 29D, pp.223-235, 1987.

[6] Réal Vallée and C. Delisle, "Mode description of the dynamical evolution of an acousto-optic bistable device," IEEE J. Quantum Electron., vol.QE-21, pp.1423-1428, Sept. 1985.

[7] T.Aida and P.Davis, "Oscillation modes of laser diode pumped hybrid bistable system with large delay and application to dynamical memory," IEEE J. Quantum Electron., vol.28, pp.686-699, Mar. 1992.

[8] P.Davis and K.Ikeda, "Switching between multistable oscillations and applications in signal generator and memory," Technical Digest of the 16th International Conference on Quantum Electronics, ThC-3, pp.634-635, Tokyo, Jul. 1988.

[9] P.Davis, "Application of Optical Chaos to Temporal Pattern Search in a Nonlinear Optical Resonator," Jap. J. Appl. Phys. vol.29, pp.L1238-L1240, Jul. 1990.

[10] T.Aida and P.Davis, "Storage of optical pulse data sequences in loop memory using multistable oscillations," Electron. Lett., vol.27, pp.1544-1546, Aug. 1991.

[11] T.Aida and P.Davis, "Applicability of bifurcation to chaos : Experimental demonstration of methods for switching among multistable modes in a nonlinear resonator," OSA Proc. on Nonlinear Dynamics in Optical Systems, N.B.Abraham, E.M.Garmire and P.Mandel, eds., vol.7, pp.540-544, 1991.

[12] C. Grebogi, E. Ott, F. Romeiras and J. A. Yorke, "Critical exponents for crisis-induced intermittency," Phys. Rev. A, vol.36, pp.5365-5380, Dec. 1987.

[13] K. Ikeda, K. Otsuka and K. Matsumoto, "Maxwell-Bloch turbulence," Prog. Theor. Phys. Suppl. vol.99, pp.295-323, 1989.

[14] K. Otsuka,"Self-induced phase turbulence and chaotic itinerancy in coupled laser systems," Phys. Rev. Lett. vol.65, pp.329-332, Jul. 1990.

[15] F. T. Arecchi, G. Giacomelli, P. L. Ramazza and S. Residori, "Experimental evidence of chaotic itinerancy and spatio-temporal chaos in optics," Phys. Rev. Lett. vol.65, pp.2531-2534, Nov. 1990.

[16] P.Davis and T.Aida, "Constraining chaos in an optical ring memory device," Proc. of Intern. Conf. on Fuzzy Logic and Neural Networks, pp.905-908, Iizuka, Japan, Jul. 1992.

[17] P.Davis, "Functional chaotic device," Proc. of Intern. Conf. on Fuzzy Logic and Neural Networks, pp.61-64, Iizuka, Japan, Jul. 1992.

[18] E. Ott, C. Grebogi and J. A. Yorke, "Controlling chaos," Phys. Rev. Lett. vol.64, pp.1196-1199, 1990.

[19] R. Roy, T. W. Murphy, T. D. Maier, Z. Gills, "Dynamical control of a chaotic laser," Phys. Rev. Lett. vol. 68, pp.1259-1262, 1992.

Figure 1: Experimental setup. LD, laser diode (wavelength $\lambda \approx 1.3\mu$m, output power Po $\sim$ 1mW; E-O modulator, Ericsson PGS6211 $LiNbO_3$ waveguide intensity modulator (half wave voltage $V_\pi \approx 6$V); optical fiber, 1.3μm single mode optical fiber (length 1000m); PD, pin photo diode; LPF, low pass filter (response time $T_m \approx 42$nsec); AMP, video amplifier (-3dB band width $\approx$ 150MHz).

Figure 2: Schematic bifurcation diagrams of oscillation level and oscillation mode. Examples of 7-th harmonic oscillation waveforms are shown for $m = 1$, $m = 2$ and $m^* = 2^*$ bifurcation orders.

Figure 3: Schematic diagram of coding circuits. The oscillation signal in the ring resonator, $V'(t)$, proportional to $V(t)$, is fed into the thresholders of the coding circuits. The threshold voltage of the thresholder, V_{th1}, is set at a level midway between high and low peak levels of $\xi_{n,2}$ mode oscillation to generate binary pulse signal $X(t)$ corresponding to binary peak levels. The threshold voltage of the other, V_{th2}, is set at a level midway between peak and valley levels of the oscillation to obtain a clock signal (CLK) which has the same period $2T_\tau/n$ as the n-th harmonic carrier oscillation. The pulsewidth extenders are monomulti-vibrators triggered by the rise edge of $X(t)$, generating binary pulse signals $S_1(t)$ and $S_2(t)$ of constant pulsewidth T_τ/n and $3.5T_\tau/n$, respectively. The temporal patterns of $S_1(t)$ pulse sequence of length $2T_\tau$ corresponds to $\boldsymbol{J}$ code. The $\boldsymbol{J}$ code is latched and updated at a rate of $2T_1 \approx 4T_\tau$ interval. The counter and latch generate and update a feature value R by counting up the pulses of $S_2(t)$ sequence in each $T \approx 20T_\tau$ interval. The differential circuit generates error signal $E = |R - R^c|$, where R^c is a specified target value. The error signal E is D/A-converted and is used to generate feedback signal $G(E)$. The timing signals of period $2T_1$ and T are generated by $1/(2n)$ and $1/(10n)$ division of the clock signal CLK, respectively.

Figure 4: Examples of oscillating optical intensity output signal and corresponding pulse trains. (a) periodic$\xi_{7,2}$ mode and (b) chaotic $\xi_{7,2^*}$ mode. Signals indicated by $V'(t)$, $X(t)$, $S_1(t)$ and $S_2(t)$ are observed at the points indicated in the coding circuits of figure 3. A sequence of 7 pulses in the $S_1(t)$ signal corresponds to the 7-bit binary $\boldsymbol{J}$ coding of the pattern of modulation of oscillation peaks. The number of pulses of the $S_2(t)$ signal in $T \approx 20T_\tau$ interval is the feature value R.

Figure 5: Ten different modes, "isomers", of $\xi_{n=7,m=2}$ mode. The upper trace $V'(t)$ shows the oscillating optical intensity signal output from the resonator. The lower traces $S_1(t)$ and $S_2(t)$ show the binary pulse sequences obtained from the output signal by threshold operation. A sequence of 7 pulses in the $S_1(t)$ signal corresponds to the 7-bit binary $\boldsymbol{J}$ coding of the pattern of modulation of oscillation peaks. Without phase identification, cyclic pulse trains, $\boldsymbol{J}$ and $\overline{\boldsymbol{J}}$ degenerate into ten classes, which are labeled with a mode number p. These are classified further into four classes according to feature value, $R \in \{20, 25, 30, 35\}$, defined as the number of pulses of the $S_2(t)$ signal in $T \approx 20T_\tau$ interval.

Figure 6: Typical transition matrices for code sequences obtained from a single chaotic time series of $\xi_{n=7,m=2}$ mode, (a) J code and (b) R code. Transition ratio is relative number of transitions, that is, the number of times that a transition occurs divided by total number of transitions. The length of the time series is about 8,000,000T_r (≈40sec). Diagonal terms are omitted. Diagonal terms are large because of long residence time.

Figure 7: Increasing degree of chaos of 7-th harmonic oscillation observed in waveforms and R dynamics. (a) Below the onset of chaos, oscillation waveforms are stable and the feature value R remains constant at 30. Feature values for stable modes are {20,25,30,35}. (b) With increase of parameter μ, oscillation becomes unstable and mode transition occurs. When μ exceeds μ_{2^*}, mode transitions are seen in the R dynamics. (c) - (i) With further increase of μ above μ_{2^*}, the rate of mode transitions increases. The levels of input optical power P_i are (a)1.065mW, (b)1.097mW, (c)1.100mW, (d)1.102mW, (e)1.104mW, (f)1.106mW, (g)1.111mW, (h)1.113mW and (i)1.125mW, respectively.

Figure 8: Distribution of visiting ratio of R for the case of figure 7(f).

Figure 9: Residence time distributions and their dependence on pump parameter μ. A histogram of the number of instances in a single chaotic sequence that a code value $R = 25$ persisted for a time τ_R. Time is in units of $T = 10T_1 \approx 20T_r$. Values of μ, small, medium and large, correspond to the values for figures 7(b),(f) and (h), respectively.

Figure 10: Average residence times $< \tau_R >$ for the different classes of oscillation. Oscillations are classified by feature value R. Values of μ, small, medium and large, correspond to the values for figures 7(b),(f) and (h), respectively. Residence times are longer for feature values $R \in \{20, 25, 30, 35\}$ corresponding to the $\xi_{7,2}$ oscillation modes. The smaller the parameter value μ, the longer the average residence time $< \tau_R >$ for $R \in \{20, 25, 30, 35\}$.

Figure 11: Average absence time $< \tau_A >$ for the different classes of oscillations. Oscillations are classified by feature value R. Values of μ, small, medium and large, correspond to values for figure 7(b),(f) and (h), respectively. Feature values corresponding to the $\xi_{7,2}$ oscillation modes, $R \in \{20, 25, 30, 35\}$, appear more often than other values. The smaller the parameter value μ, the longer the average absence time $< \tau_A >$ of $R \in \{20, 25, 30, 35\}$.

Figure 12: Shape of control function $G(E)$ used to feedback the error signal E of the output state to the laser power, according to equation (2). Two cases are shown; (a) for multi-mode localization $G(0)$, the lowest value of $G(E)$, is set just above the value for onset of chaotic transitions, μ_{2^*}, (b) when convergence to a stable mode is required, single-mode selection, $G(0)$ is set below μ_{2^*}.

Figure 13: The effect of adaptive parametric control of equation (2). (a)Distribution of visiting ratio of $\boldsymbol{J}$ code when $\mu = \mu_s$ without control. (b)Localization of chaos in states with low $E = |R - R^c|$ when the adaptive parametric control is used. $R^c = 30$ and the curve (a) of figure 12 was employed for control function. The localization is seen as the increase of the visiting ratio of modes, specified here by $\boldsymbol{J}$ code, with feature value $R = 30$.

Figure 14: Example of CS time series of $V(t)$ and E. The target is an isomer of $\xi_{7,2}$ mode with $R = 25$.

Figure 15: Expanded CS time series for points marked with (a), (b) and (c) in figure 14.

Figure 16: Example of repeated chaotic switching. $R^c = 25$ and $T_g = 0.865T(\approx 17.3T_r)$. In each ERASE interval error E is forcibly held at a large value, $E = 25$, where μ takes the value of μ_s, so the memory of the initial state is lost, and search can commence from a random point on the chaotic attractor. In each SEARCH interval chaotic search takes place under the adaptive parametric control of equation (2). The repeat cycle of this example is 10Hz, corresponding to a search time cutoff of 50msec. Chaotic search is seen to be successful if E converges to 0 within the cutoff time.

Figure 17: Dependence of CS time for 90% success rate on control response time T_g.

Figure 18: Success rate in finding a target mode as a function of elapsed time. Curve (a) shows the probability of converging to the target mode $\xi_{7,2,R=25}$ under CS control of equation (2) with $T_g = 0.865T(\approx 17.3T_r)$ and $G(E)$ as in figure 12(b). Curves (b)$\cdots$(e) show the probability of finding sequences of the target value $R = 25$ for unconstrained chaos without control (control loop open) at $\mu = \mu_s$. Respectively, the probability finding a sequence (residence time) of length (b) $1T$ ($T \approx 20T_r$), (c) $5T$, (d) $10T$, (e) $20T$. Note, probability is defined as the relative number of observed events.

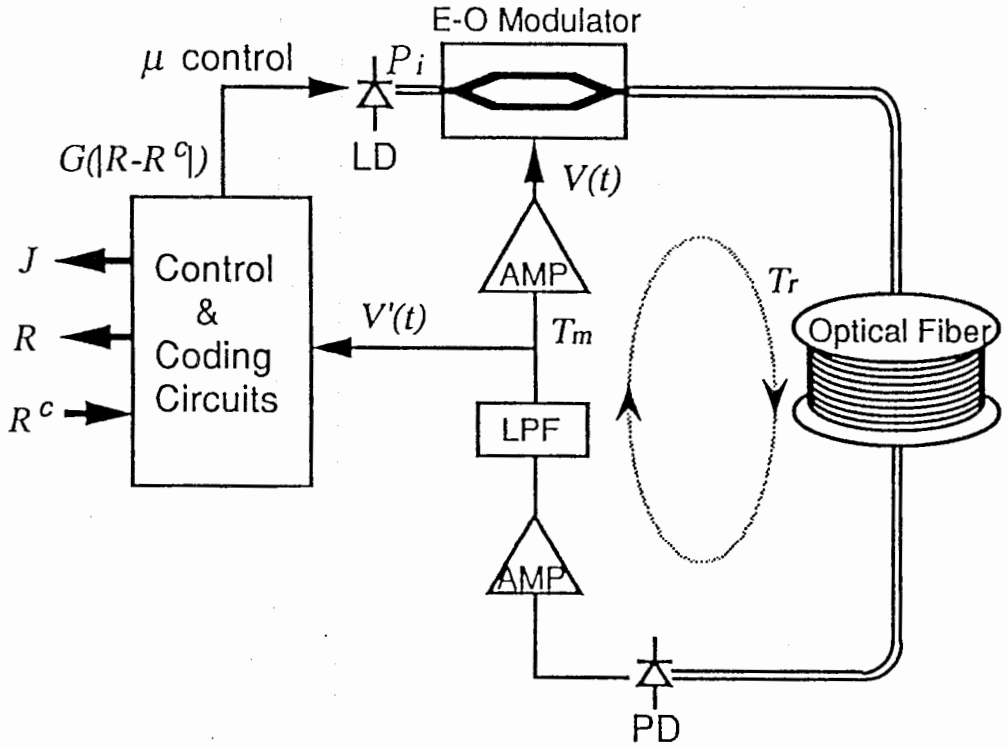

Experimental setup

Figure 1: Experimental setup. LD, laser diode (wavelength $\lambda \approx 1.3\mu$m, output power Po $\sim$ 1mW; E-O modulator, Ericsson PGS6211 $LiNb0_3$ waveguide intensity modulator (half wave voltage $V_\pi \approx 6$V); optical fiber, 1.3μm single mode optical fiber (length 1000m); PD, pin photo diode; LPF, low pass filter (response time $T_m \approx 42$nsec); AMP, video amplifier (-3dB band width $\approx$ 150MHz).

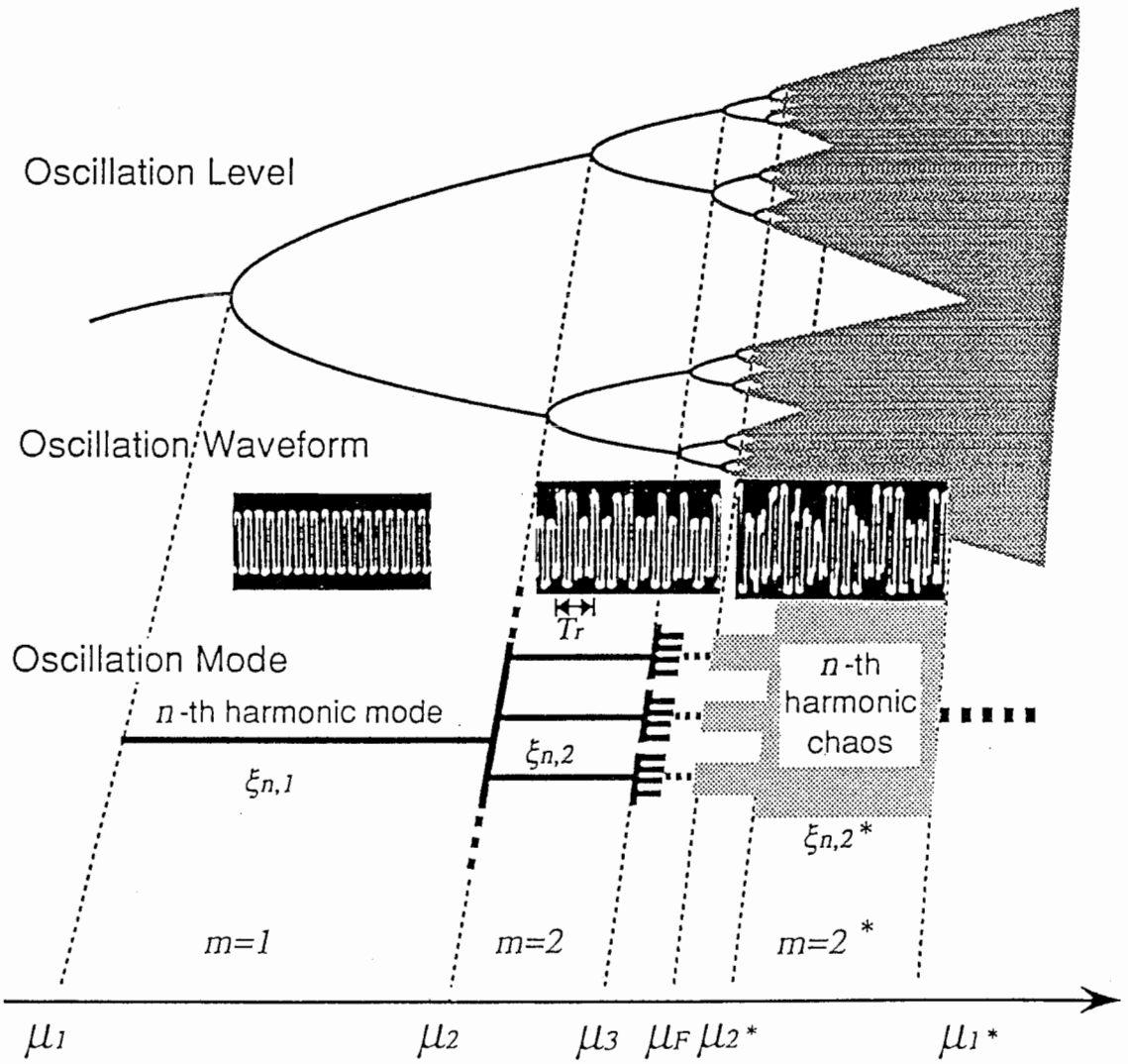

Figure 2: Schematic bifurcation diagrams of oscillation level and oscillation mode. Examples of 7-th harmonic oscillation waveforms are shown for $m = 1$, $m = 2$ and $m^* = 2^*$ bifurcation orders.

Bifurcation diagram

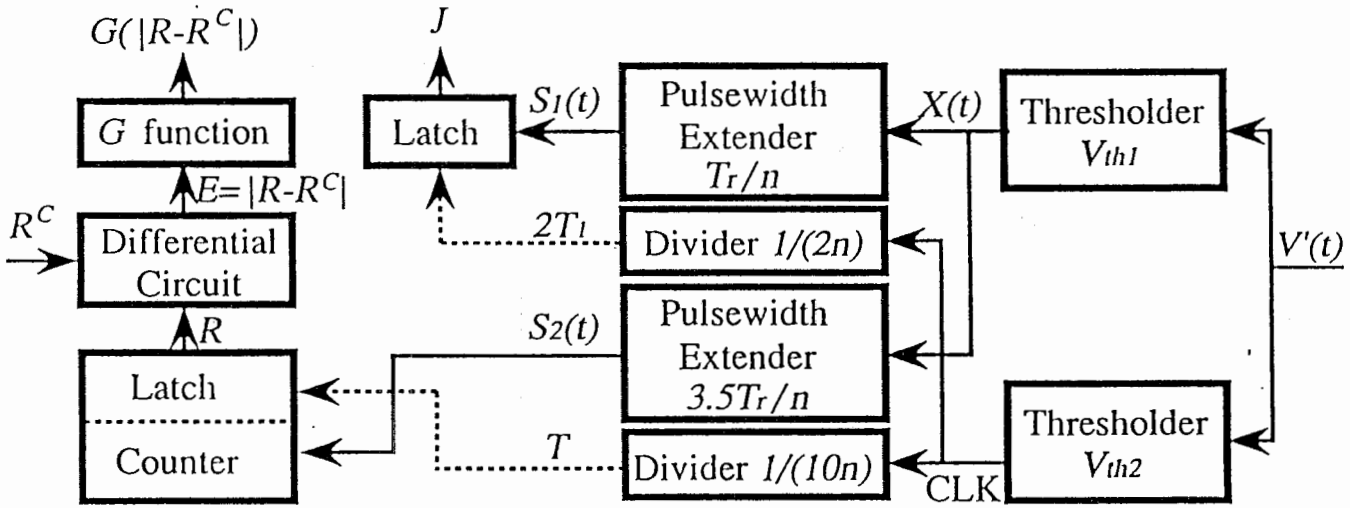

Figure 3: Schematic diagram of coding circuits. The oscillation signal in the ring resonator, $V'(t)$, proportional to $V(t)$, is fed into the thresholders of the coding circuits. The threshold voltage of the thresholder, V_{th1}, is set at a level midway between high and low peak levels of $\xi_{n,2}$ mode oscillation to generate binary pulse signal $X(t)$ corresponding to binary peak levels. The threshold voltage of the other, V_{th2}, is set at a level midway between peak and valley levels of the oscillation to obtain a clock signal (CLK) which has the same period $2T_r/n$ as the n-th harmonic carrier oscillation. The pulsewidth extenders are monomulti-vibrators triggered by the rise edge of $X(t)$, generating binary pulse signals $S_1(t)$ and $S_2(t)$ of constant pulsewidth T_r/n and $3.5T_r/n$, respectively. The temporal patterns of $S_1(t)$ pulse sequence of length $2T_r$ corresponds to $\boldsymbol{J}$ code. The $\boldsymbol{J}$ code is latched and updated at a rate of $2T_1 \approx 4T_r$ interval. The counter and latch generate and update a feature value R by counting up the pulses of $S_2(t)$ sequence in each $T \approx 20T_r$ interval. The differential circuit generates error signal $E = |R - R^c|$, where R^c is a specified target value. The error signal E is D/A-converted and is used to generate feedback signal $G(E)$. The timing signals of period $2T_1$ and T are generated by $1/(2n)$ and $1/(10n)$ division of the clock signal CLK, respectively.

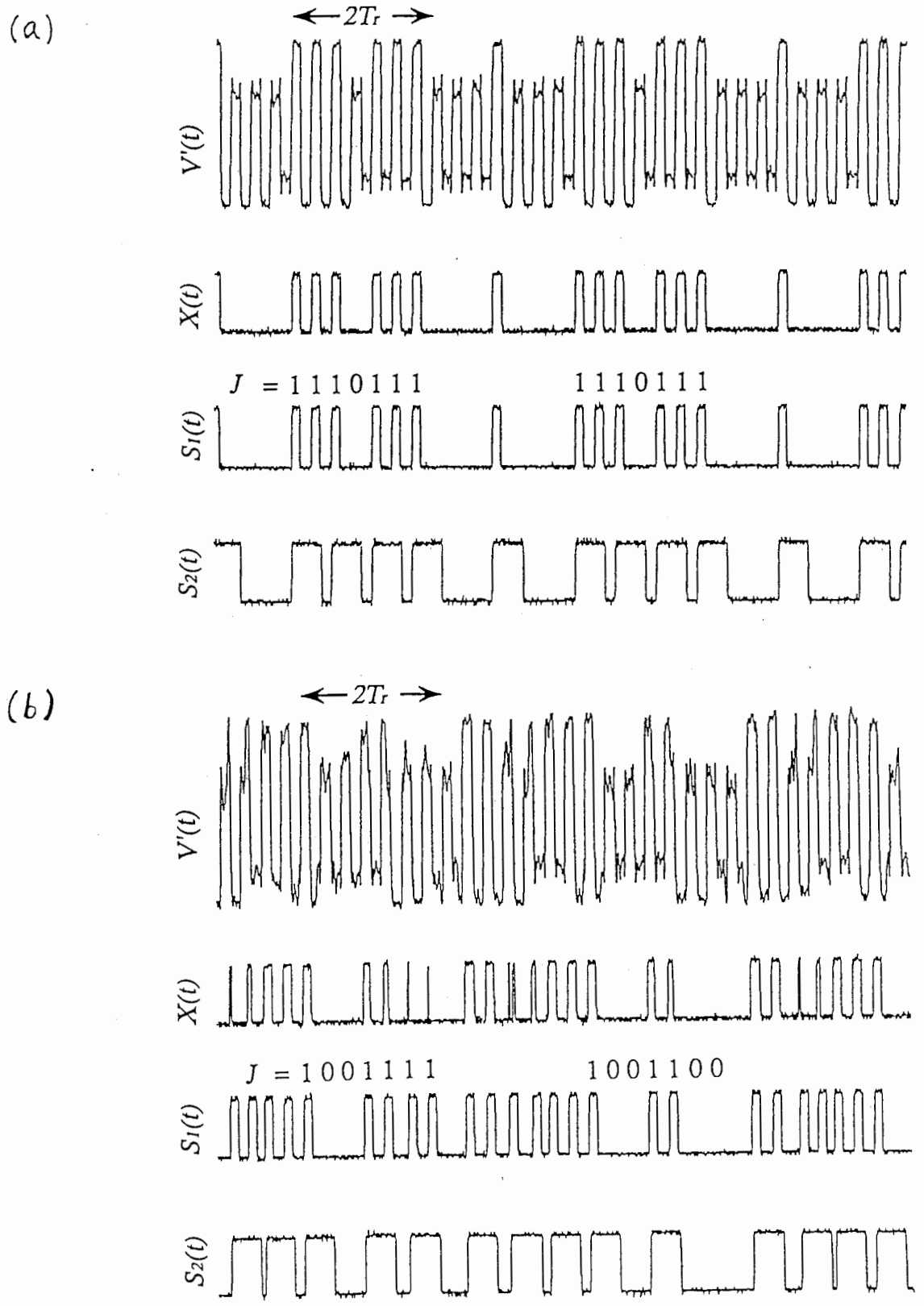

Figure 4: Examples of oscillating optical intensity output signal and corresponding pulse trains. (a) periodic$\xi_{7,2}$ mode and (b) chaotic $\xi_{7,2}$ mode. Signals indicated by $V'(t)$, $X(t)$, $S_1(t)$ and $S_2(t)$ are observed at the points indicated in the coding circuits of figure 3. A sequence of 7 pulses in the $S_1(t)$ signal corresponds to the 7-bit binary J coding of the pattern of modulation of oscillation peaks. The number of pulses of the $S_2(t)$ signal in $T \approx 20T_r$ interval is the feature value R.

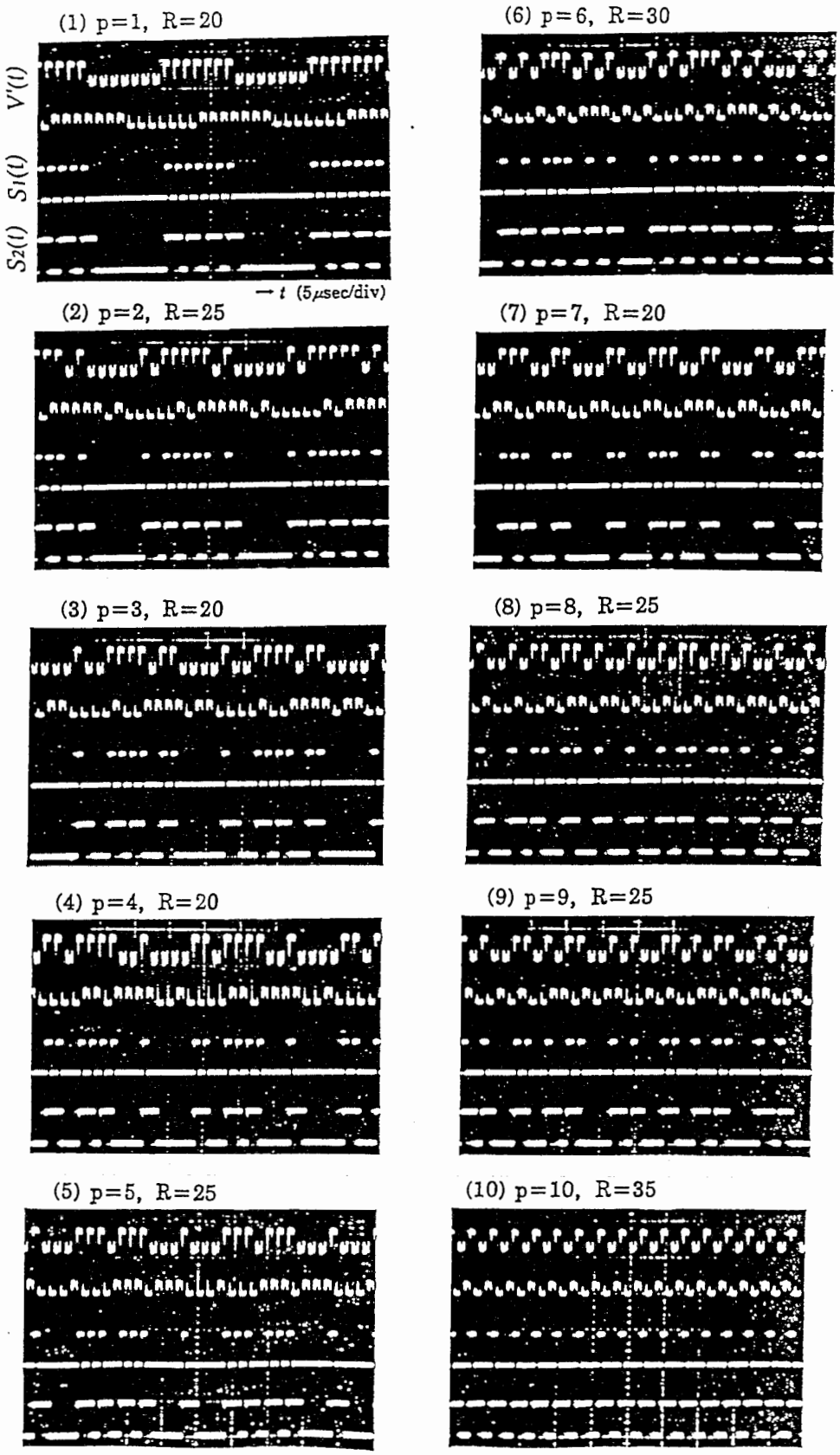

Figure 5: Ten different modes, "isomers", of $\xi_{n=7,m=2}$ mode. The upper trace $V'(t)$ shows the oscillating optical intensity signal output from the resonator. The lower traces $S_1(t)$ and $S_2(t)$ show the binary pulse sequences obtained from the output signal by threshold operation. A sequence of 7 pulses in the $S_1(t)$ signal corresponds to the 7-bit binary $\boldsymbol{J}$ coding of the pattern of modulation of oscillation peaks. Without phase identification, cyclic pulse trains, $\boldsymbol{J}$ and $\overline{\boldsymbol{J}}$ degenerate into ten classes, which are labeled with a mode number p. These are classified further into four classes according to feature value, $R \in \{20, 25, 30, 35\}$, defined as the number of pulses of the $S_2(t)$ signal in $T \approx 20T_r$ interval.

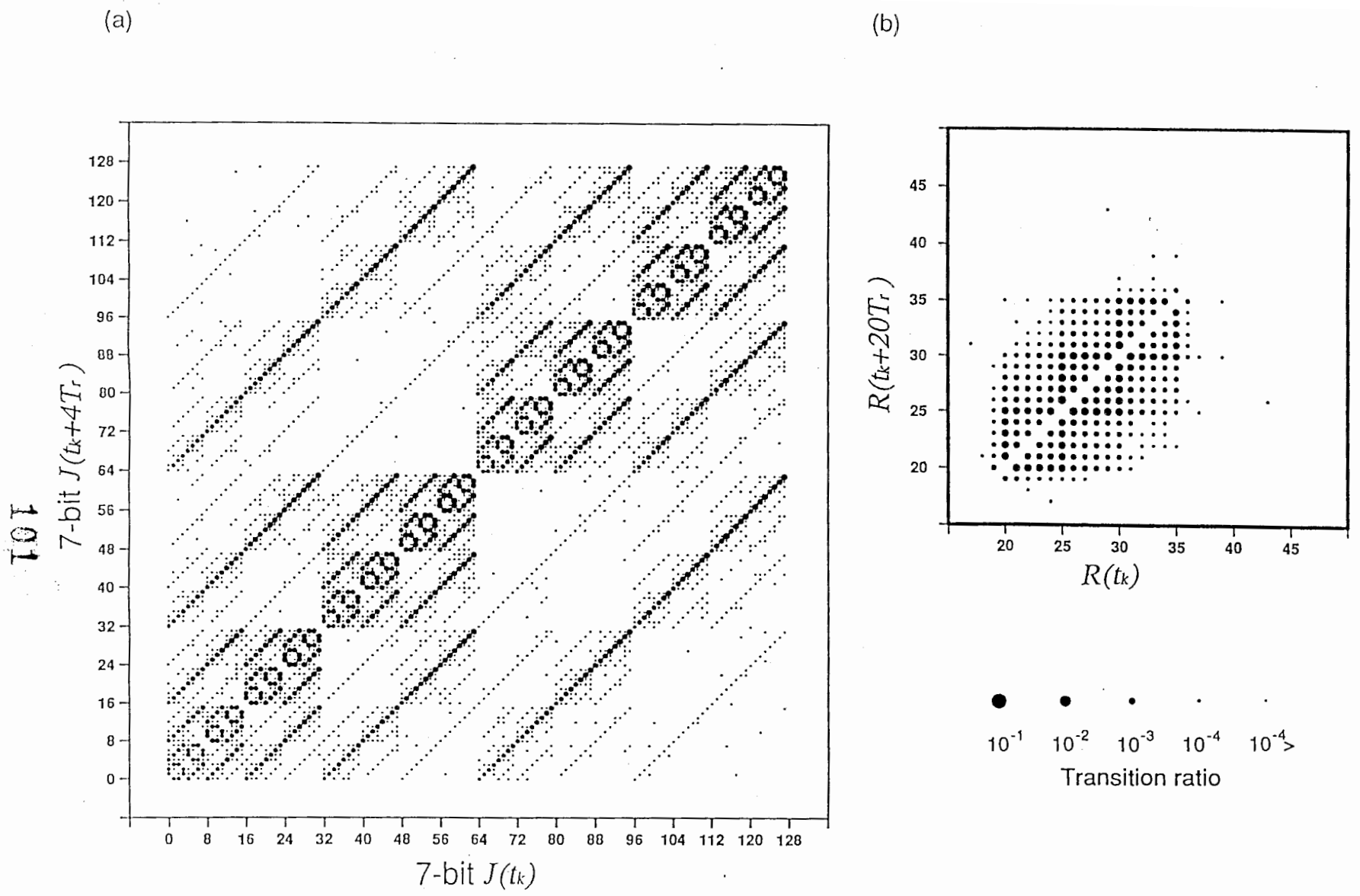

Figure 6: Typical transition matrices for code sequences obtained from a single chaotic time series of $\xi_{n=7,m=2}$ mode, (a) J code and (b) R code. Transition ratio is relative number of transitions, that is, the number of times that a transition occurs divided by total number of transitions. The length of the time series is about 8,000,000T_r (≈40sec). Diagonal terms are omitted. Diagonal terms are large because of long residence time.

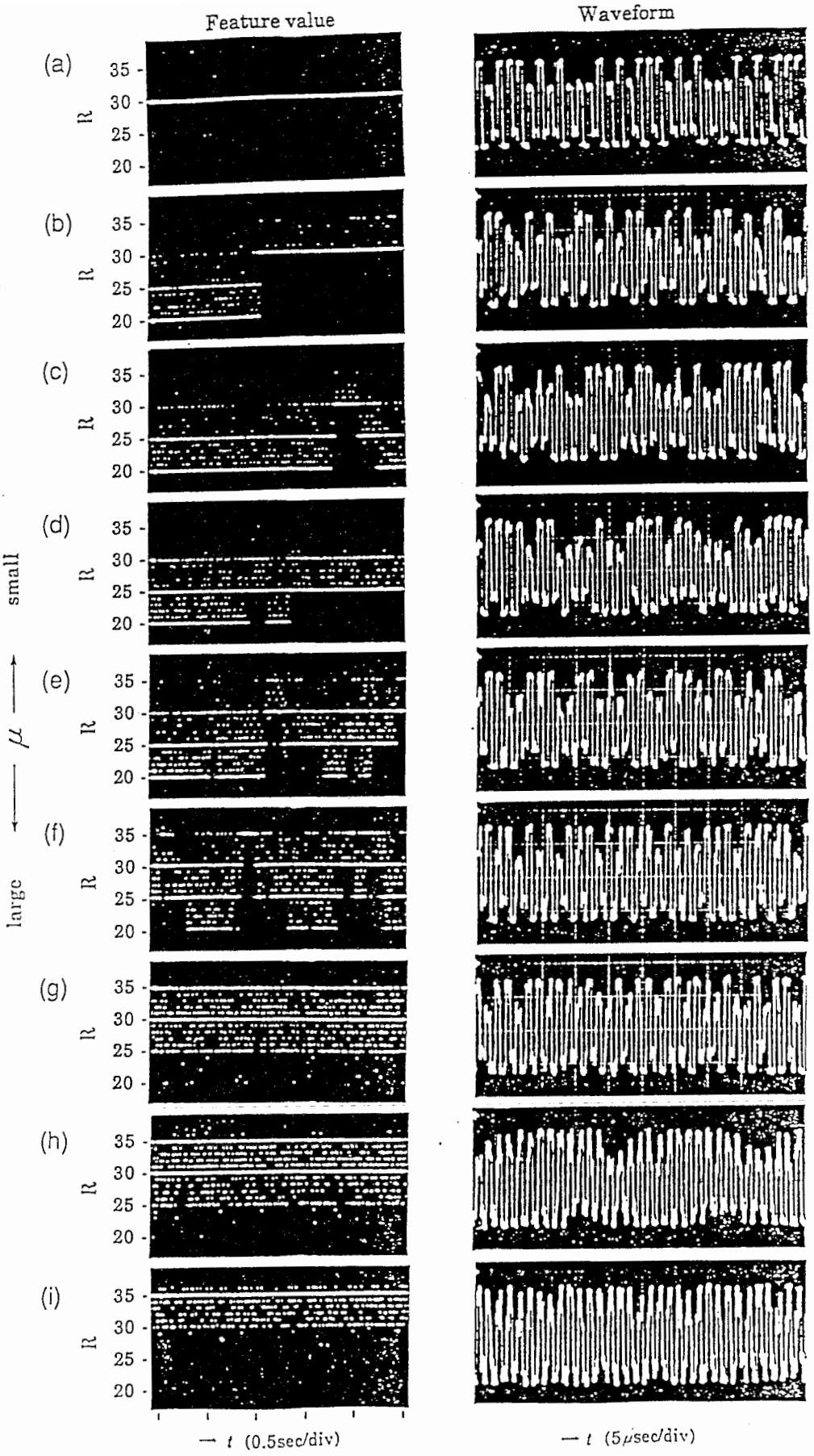

Figure 7: Increasing degree of chaos of 7-th harmonic oscillation observed in waveforms and R dynamics. (a) Below the onset of chaos, oscillation waveforms are stable and the feature value R remains constant at 30. Feature values for stable modes are {20,25,30,35}. (b) With increase of parameter μ, oscillation becomes unstable and mode transition occurs. When μ exceeds μ_{2^*}, mode transitions are seen in the R dynamics. (c) - (i) With further increase of μ above μ_{2^*}, the rate of mode transitions increases. The levels of input optical power P_i are (a)1.065mW, (b)1.097mW, (c)1.100mW, (d)1.102mW, (e)1.104mW, (f)1.106mW, (g)1.111mW, (h)1.113mW and (i)1.125mW, respectively.

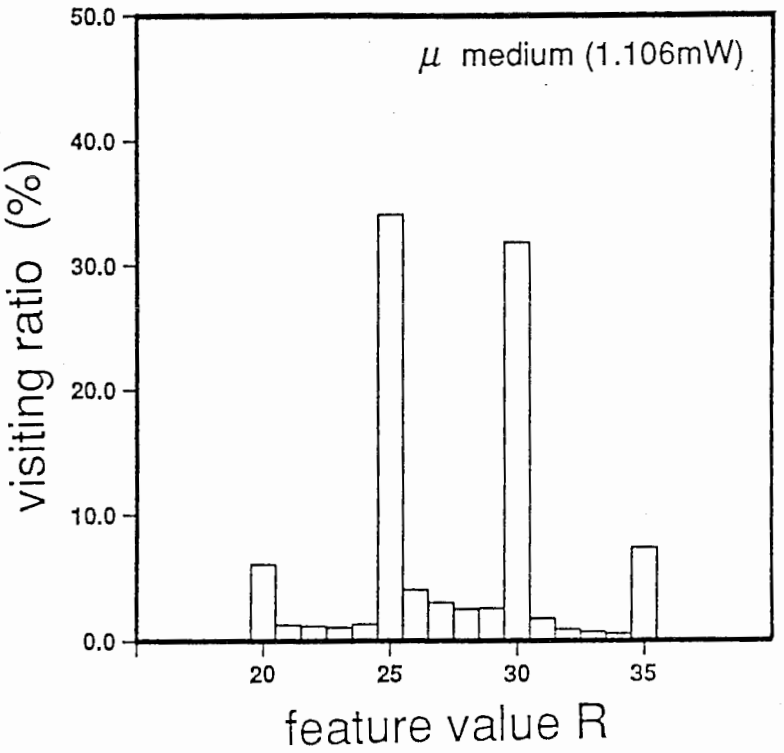

Figure 8: Distribution of visiting ratio of R for the case of figure 7(f).

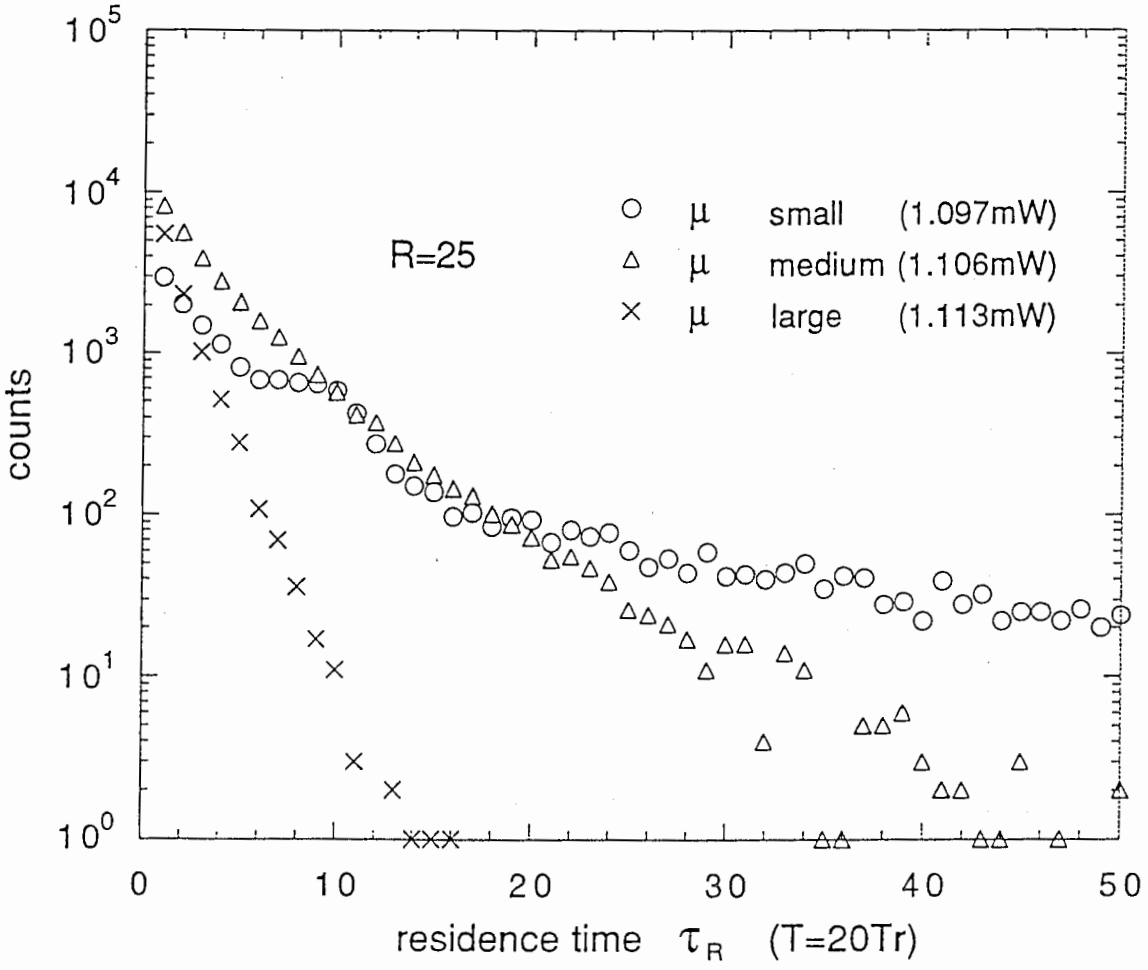

Figure 9: Residence time distributions and their dependence on pump parameter μ. A histogram of the number of instances in a single chaotic sequence that a code value $R = 25$ persisted for a time τ_R. Time is in units of $T = 10T_1 \approx 20T_r$. Values of μ, small, medium and large, correspond to the values for figures 7(b),(f) and (h), respectively.

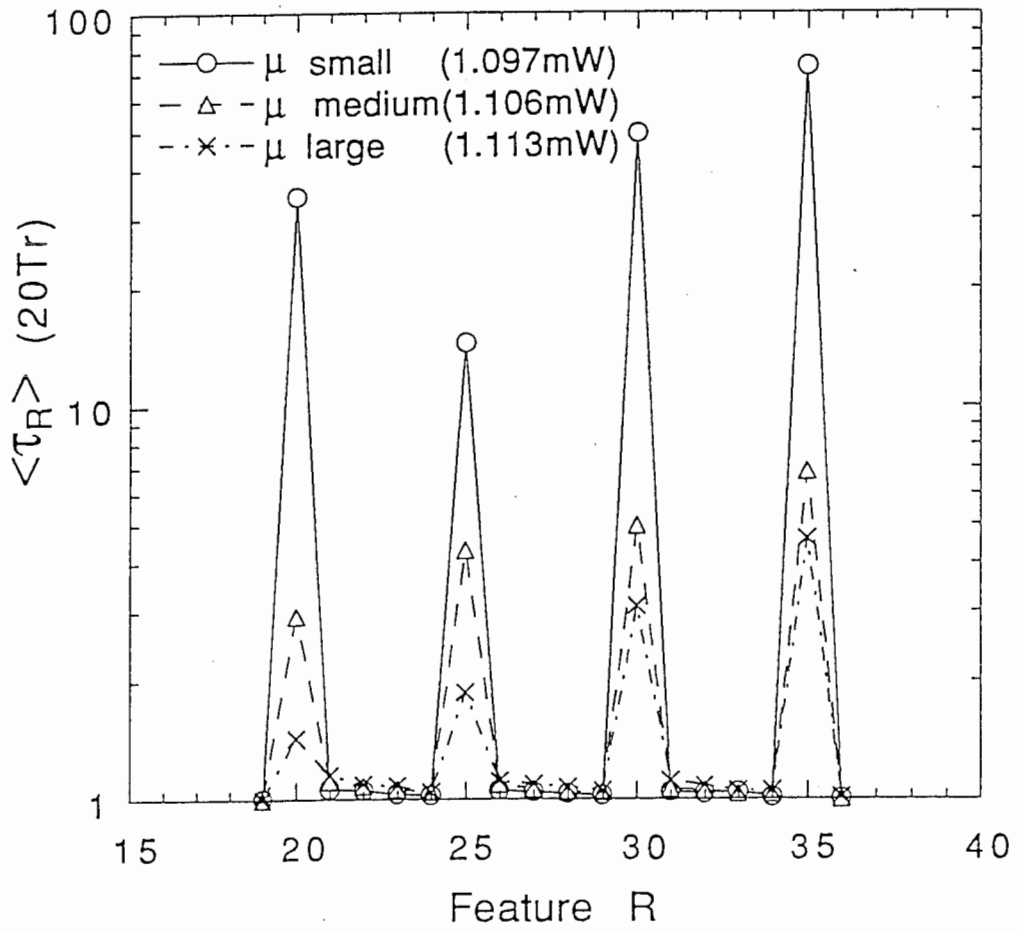

Figure 10: Average residence times $< \tau_R >$ for the different classes of oscillation. Oscillations are classified by feature value R. Values of μ, small, medium and large, correspond to the values for figures 7(b),(f) and (h), respectively. Residence times are longer for feature values $R \in \{20, 25, 30, 35\}$ corresponding to the $\xi_{7,2}$ oscillation modes. The smaller the parameter value μ, the longer the average residence time $< \tau_R >$ for $R \in \{20, 25, 30, 35\}$.

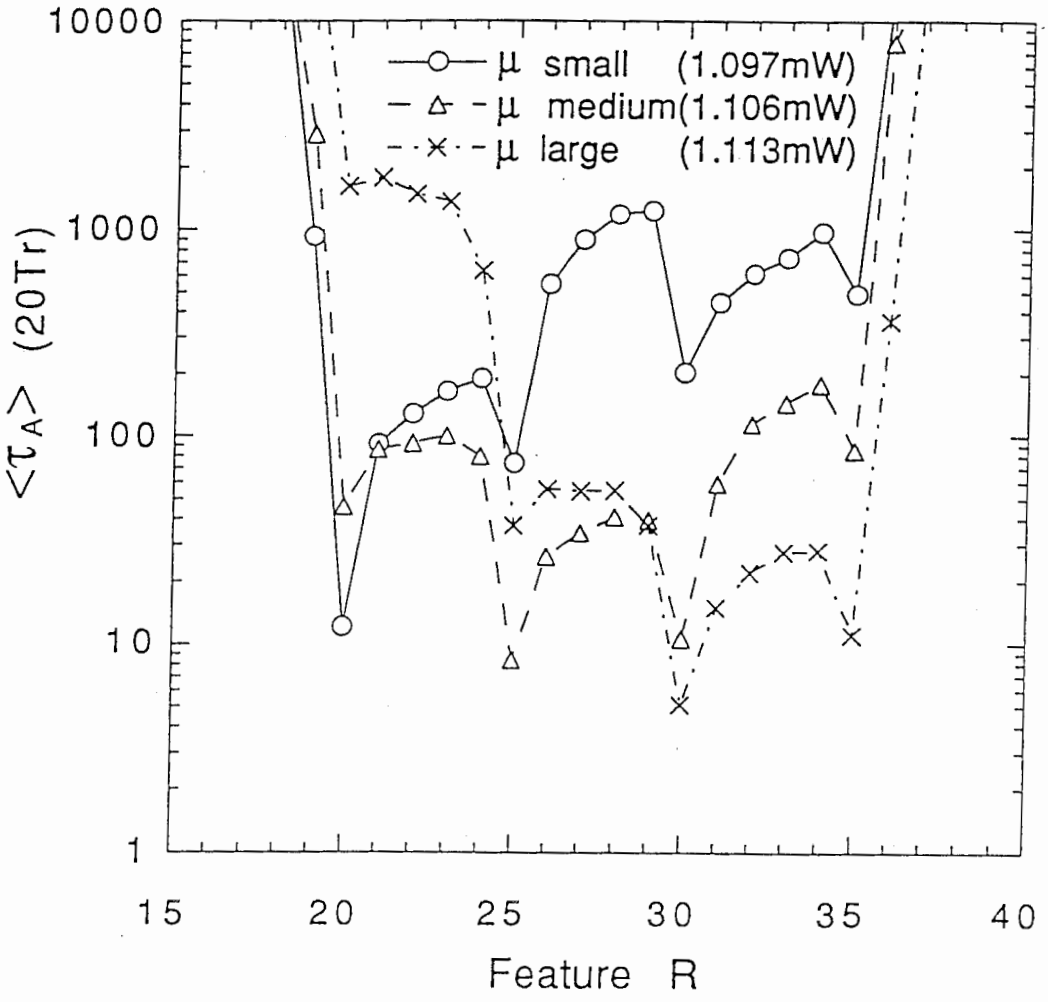

Figure 11: Average absence time $< \tau_A >$ for the different classes of oscillations. Oscillations are classified by feature value R. Values of μ, small, medium and large, correspond to values for figure 7(b),(f) and (h), respectively. Feature values corresponding to the $\xi_{7,2}$ oscillation modes, $R \in \{20, 25, 30, 35\}$, appear more often than other values. The smaller the parameter value μ, the longer the average absence time $< \tau_A >$ of $R \in \{20, 25, 30, 35\}$.

(a)

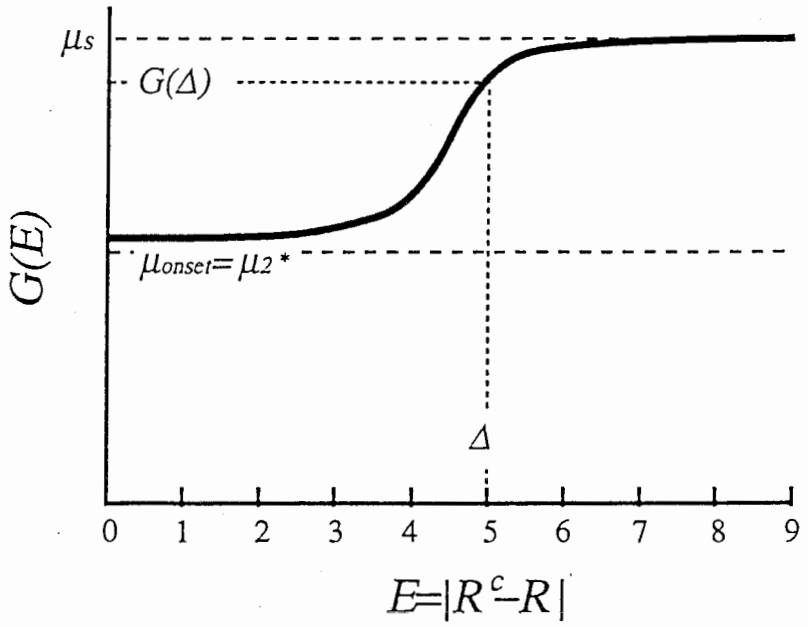

(b)

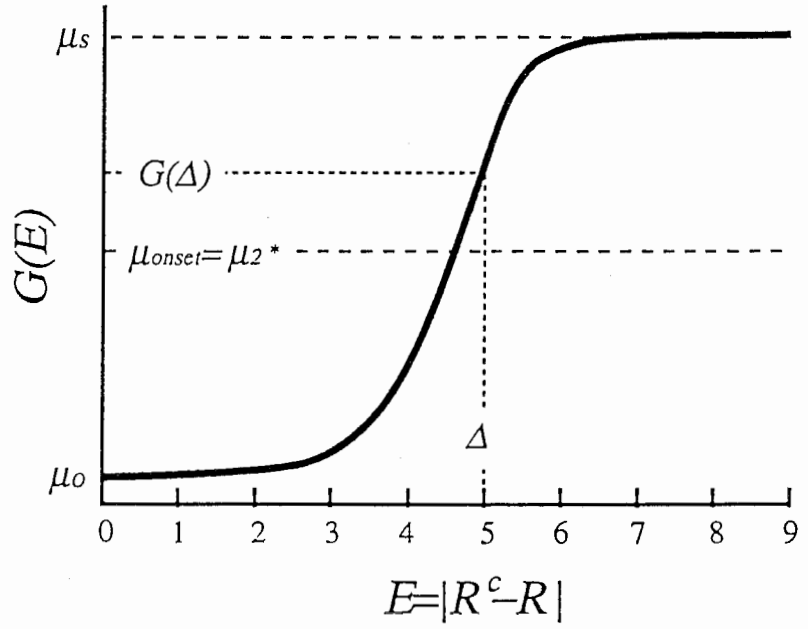

Figure 12: Shape of control function $G(E)$ used to feedback the error signal E of the output state to the laser power, according to equation (2). Two cases are shown; (a) for multi-mode localization $G(0)$, the lowest value of $G(E)$, is set just above the value for onset of chaotic transitions, μ_{2^*}, (b) when convergence to a stable mode is required, single-mode selection, $G(0)$ is set below μ_{2^*}.

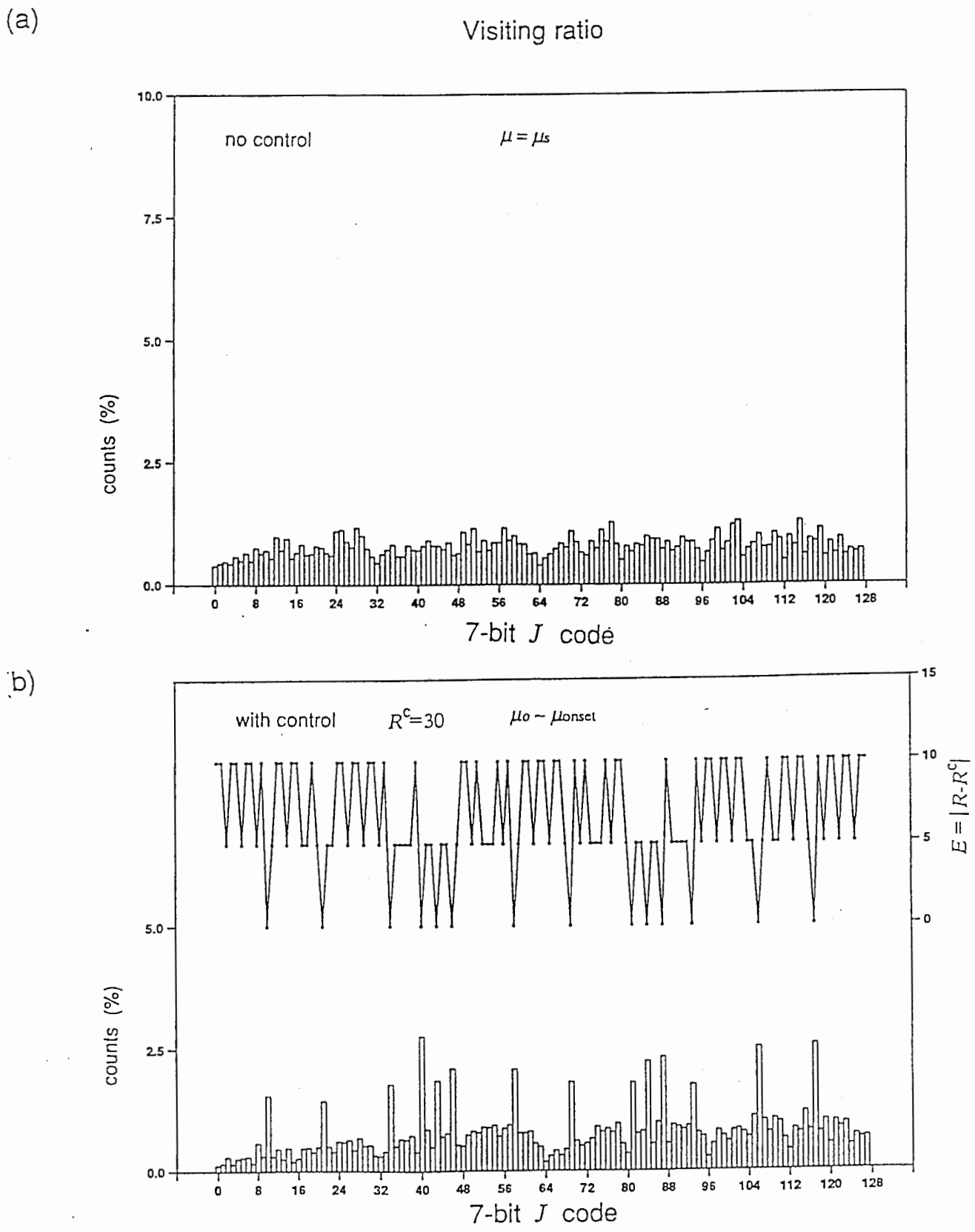

Figure 13: The effect of adaptive parametric control of equation (2). (a)Distribution of visiting ratio of $\boldsymbol{J}$ code when $\mu = \mu_s$ without control. (b)Localization of chaos in states with low $E = |R - R^c|$ when the adaptive parametric control is used. $R^c = 30$ and the curve (a) of figure 12 was employed for control function. The localization is seen as the increase of the visiting ratio of modes, specified here by $\boldsymbol{J}$ code, with feature value $R = 30$.

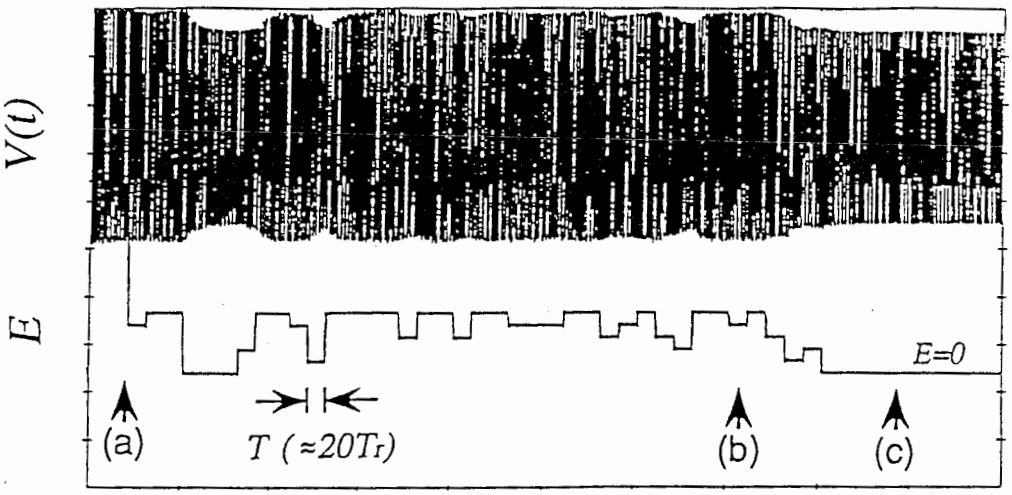

Figure 14: Example of CS time series of $V(t)$ and E. The target is an isomer of $\xi_{7,2}$ mode with $R = 25$.

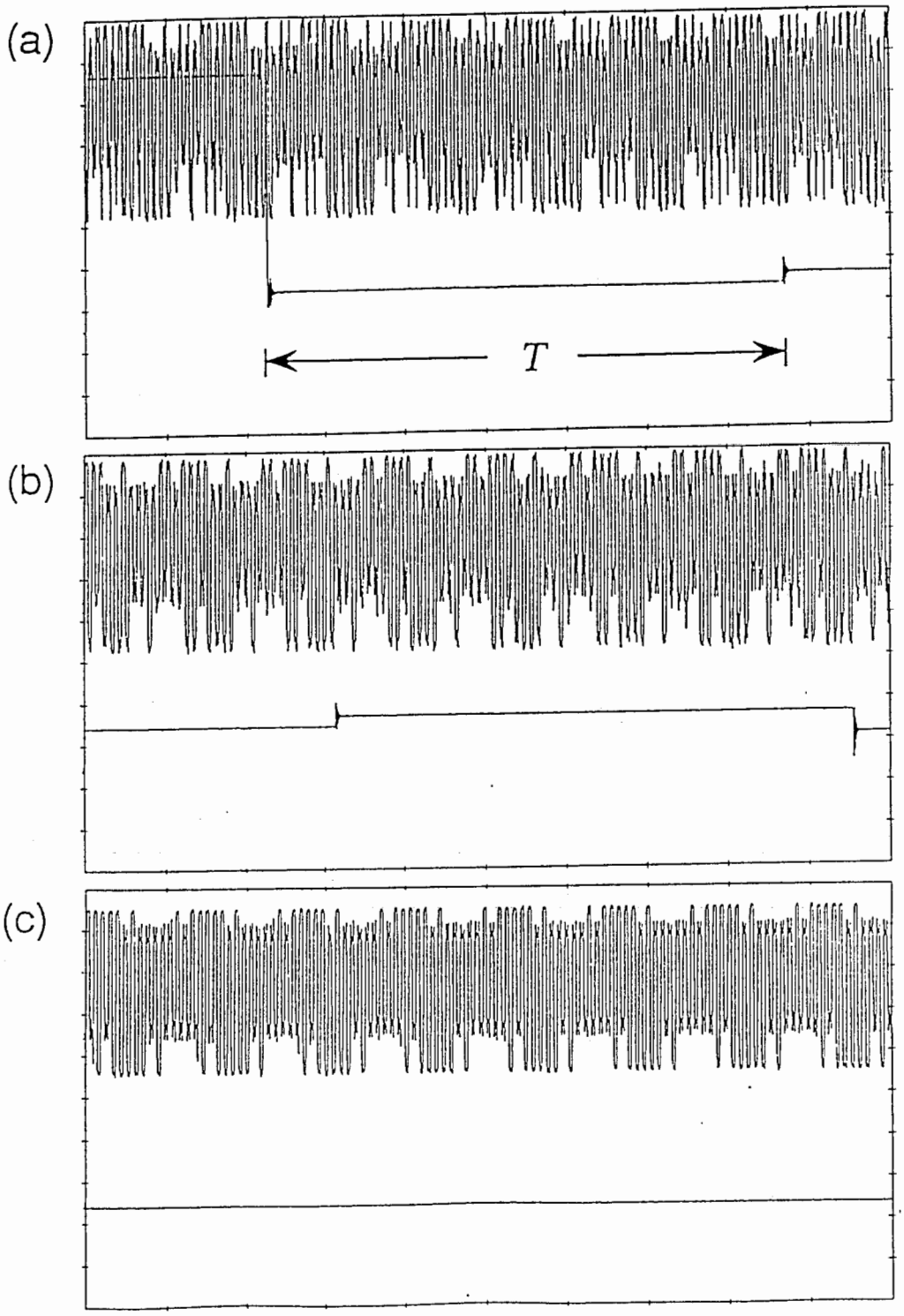

Figure 15: Expanded CS time series for points marked with (a), (b) and (c) in figure 14.

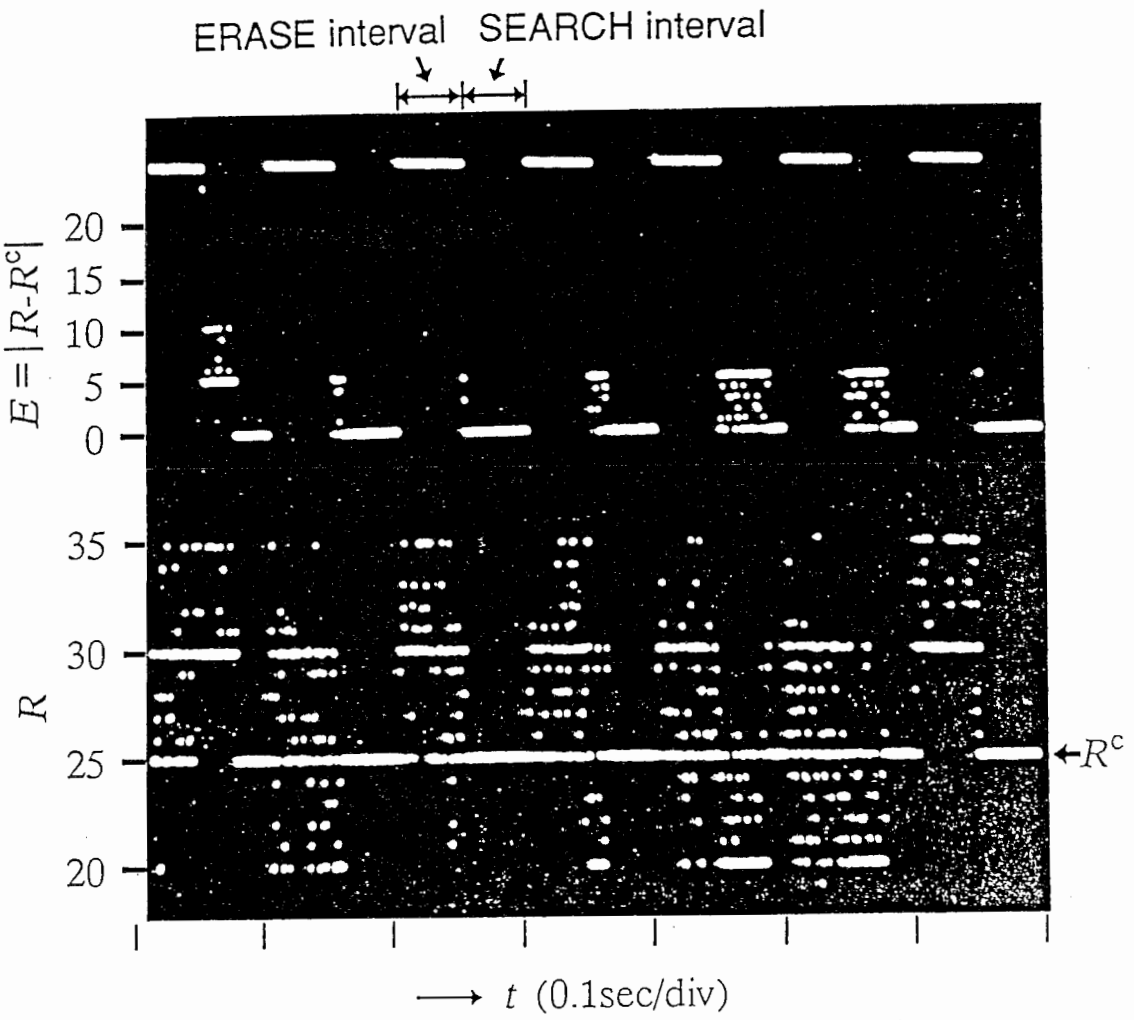

Figure 16: Example of repeated chaotic switching. $R^c = 25$ and $T_g = 0.865T(\approx 17.3T_\tau)$. In each ERASE interval error E is forcibly held at a large value, $E = 25$, where μ takes the value of μ_s, so the memory of the initial state is lost, and search can commence from a random point on the chaotic attractor. In each SEARCH interval chaotic search takes place under the adaptive parametric control of equation (2). The repeat cycle of this example is 10Hz, corresponding to a search time cutoff of 50msec. Chaotic search is seen to be successful if E converges to 0 within the cutoff time.

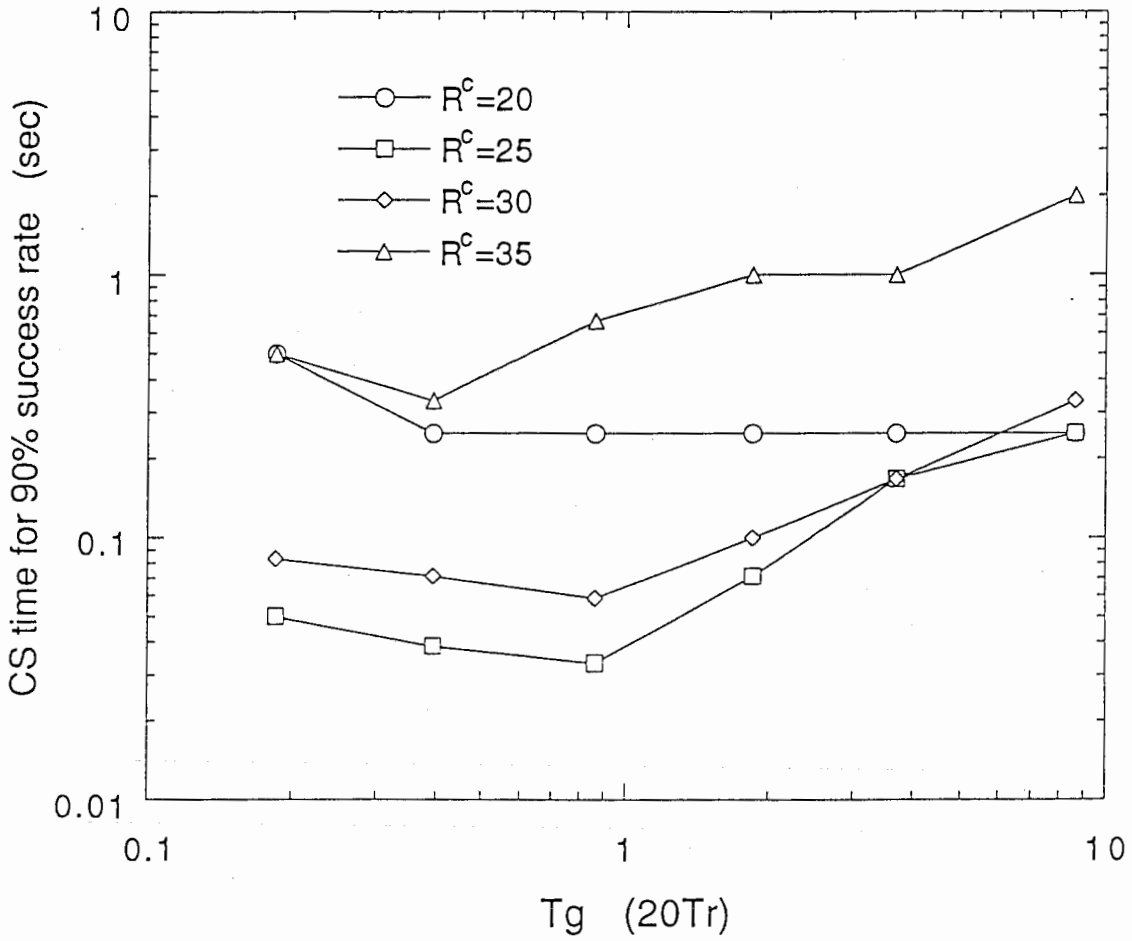

Figure 17: Dependence of CS time for 90% success rate on control response time T_g.

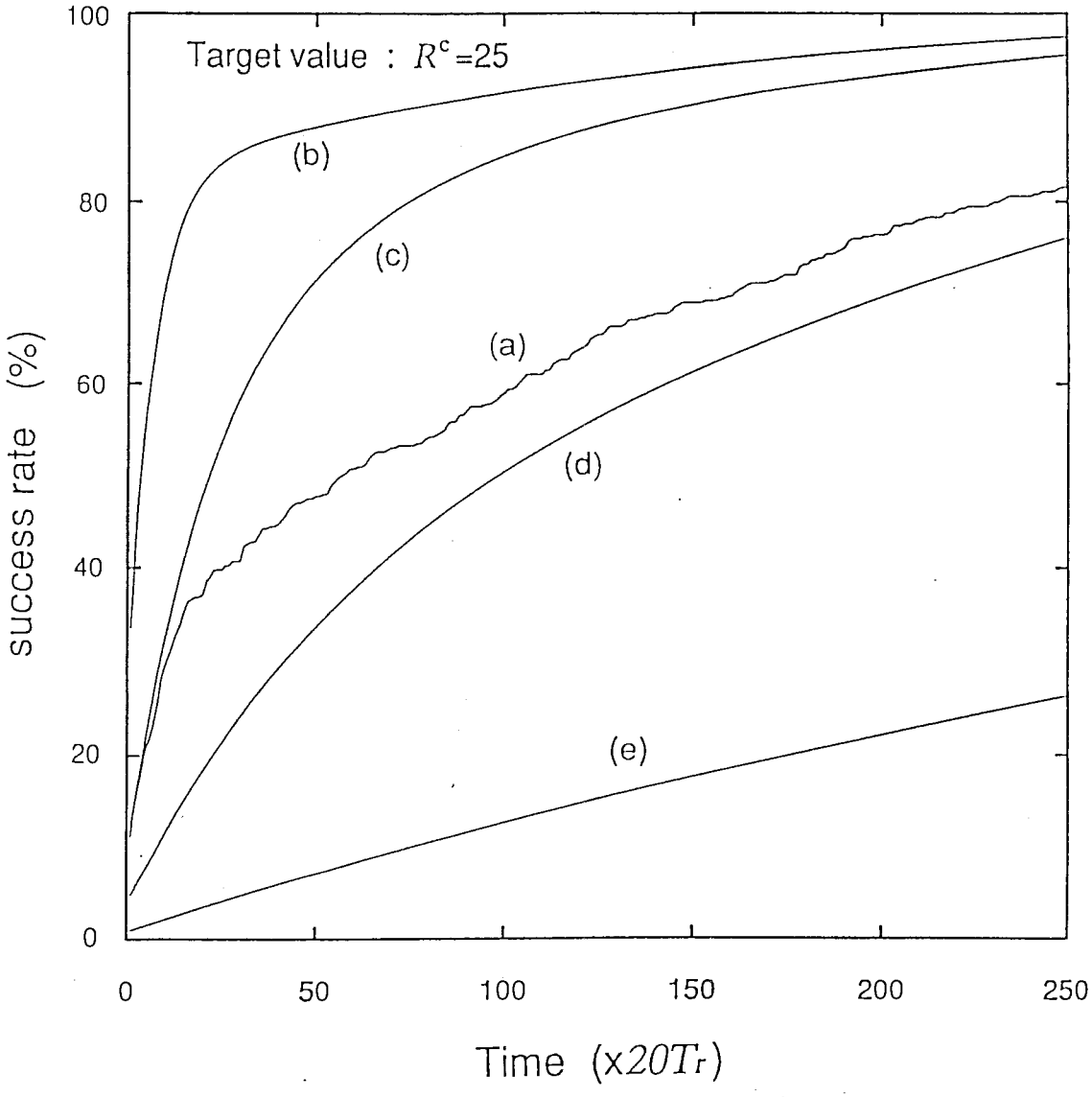

Figure 18: Success rate in finding a target mode as a function of elapsed time. Curve (a) shows the probability of converging to the target mode $\xi_{7,2,R=25}$ under CS control of equation (2) with $T_g = 0.865T(\approx 17.3T_r)$ and $G(E)$ as in figure 12(b). Curves (b)$\cdots$(e) show the probability of finding sequences of the target value $R = 25$ for unconstrained chaos without control (control loop open) at $\mu = \mu_s$. Respectively, the probability finding a sequence (residence time) of length (b) $1T$ ($T \approx 20T_r$), (c) $5T$, (d) $10T$, (e) $20T$. Note, probability is defined as the relative number of observed events.

Chapter V

Digital Implementation of A Nonlinear Delayed-Feedback System

Abstract

A digital electronic system which implements a certain class of nonlinear delayed feedback models and reproduces the nonlinear oscillation phenomena in real time was designed and constructed. The purpose of the system is two-fold: to act as a simulator and to act as a prototype design for a functional digital device using complicated nonlinear oscillations. The system has an architecture which simulates the signal flow in a nonlinear delayed feedback system with fixed-point arithmetic. We describe the design

principles aimed at maintaining the simplicity of the circuit structure and

the variety of dynamics generated. Quantization effects are discussed. In particular, it is shown how spurious quantization effects peculiar to systems can be estimated and avoided.

1 Introduction

Many types of nonlinear oscillation systems are described by nonlinear delayed feedback models. Typical systems described by delayed nonlinear feedback models are nonlinear optical cavities [1] and musical instruments [2]. Despite their simple structure, such systems can exhibit very complicated oscillation phenomena, including multistability of oscillation modes and chaotic oscillation.

The aim of the current work was to build a digital electronic system capable of generating dynamics according to the model equations governing a certain class of nonlinear delayed feedback systems. The motivation was two-fold: (1) to use the system as a versatile, real-time simulator for systematic study of dynamics of nonlinear delayed-feedback systems, and (2) to test the applicability of such a digital electronic system itself as a signal generator.

For speed and simplicity of structure, we chose a design in which the system mimics the signal flow in a delayed feedback system, rather than solves the equation describing the dynamics of the model. When designing hardware for generating nonlinear dynamics, it is important to determine to what degree dynamics should be reproducible, because nonlinear dynamics can often contain infinite complexity. In the present work, considerations of the particular dynamics observed in computer simulations and analog system experiments which we wanted to be able to generate in the digital system were used to determine the scale and architecture of the system. The designed system uses 16-bit word-length and fixed-point arithmetic. The effects of quantization in fixed-point arithmetic systems, particularly spurious hysteresis behavior, is theoretically and experimentally investigated.

2 Configuration of the System

The general conceptual structure of the nonlinear delayed feedback system is represented as a loop with linear and nonlinear parts characterized by an impulse-response function h_A and a nonlinear function g, respectively, and an overall round-trip time of t_r as $x(t) = h_A(t) * g(x(t - t_r))$, where $*$ denotes convolution.

The discrete-time equation for digital systems is expressed as

$$x(n) = h_D(n) * g(x(n - n_{t_r})) = h_D(n) * \{\mu f(x(n - n_{t_r}))\}, \tag{1}$$

where $h_D(n)$ means the impulse response of a discrete-time system corresponding to $h_A(t)$ and n_{t_r} is a delay-step number corresponding to the delay time t_r. Here, we explicitly express the loop gain μ which can be used as a control parameter. Four circuit blocks for the basic functions, μ, h_D, n_{t_r}, and f of equation (1) and an extra block inserted for testing and observing are connected in a loop with data-bus, as shown in figure 1. The dynamics of the implemented model are generated when the digital data circulates around the loop, driven by the common clock signal. For the simplicity of the configuration we employed fixed-point binary arithmetic operation system. We chose the word-length to be 16 bits.

3 Implementation of nonlinear ring cavity model

To examine the performance of the system, we implemented the nonlinear ring cavity model[1] which is modeled in the form of equation (1) as,

$$x(t) = h_A * \{\mu f(x(t - t_r))\}, \tag{2}$$

$$h_A(t) = \begin{cases} 0 & , t < 0 \\ \frac{1}{t_m} \exp(-\frac{t}{t_m}) & , t \geq 0 \end{cases}, \tag{3}$$

$$f(x) = \frac{1}{2}\{1 - \sin(2\pi x)\}. \tag{4}$$

The important factors to determine the achievable dynamics are number representation and maximum effective delay. Low noise level and large effective delay are needed for large variety of oscillation modes excited in the system. To be specific, we consider, as a reference, the performance of the E-O hybrid nonlinear ring resonator [3].

For positive values of μ, the dynamics of the model takes positive values. Hence, we employ the straight-binary (SB) representation for the 16-bit binary data. The resolution of the 16-bit word-length fixed-point binary arithmetic operation system, that is the order of the quantization noise, is $2^{-16} \approx 1.53 \times 10^{-5}$, which is adequate to distinguish order $m = 3$ bifurcations[3][4]. The effective delay for the digital system can be defined as n_{t_r}/n_{t_m}, where we define the response-step number n_{t_m} as the number of sampling data steps representing the most abrupt variation of the system dynamics. The effective delay from 0.6 to 205.3 could be realized when $n_{t_m} = 10$, and from 1.2 up to 410.6 could be achieved when $n_{t_m} = 5$.

Main tasks of the implementation of the model are writing data of equation (4)

in the lookup memory table and designing a digital filter for equation (3). These are shown in figure 2.

4 Quantization effects

The bifurcation of oscillation modes is controlled by varying feedback loop gain μ up and down. Quantization can affect the bifurcation points. We show how this effects can be easily estimated, so spurious quantization effects can be avoided.

First we discuss the expected quantization effects of the system without the digital filter. We consider a system described by the following discrete map,

$$x_{n+1} = g(x_n, \mu). \tag{5}$$

Figure 3(a) shows the calculated bifurcation diagram of the discrete map for the model implemented in the system. The system typically stays in or near steady state even after the parameter μ is increased past the bifurcation point. Figure 3(b) shows points trapped in a domain near the first bifurcation point.

A point $x_1 = x^* + \delta x_1$ near the fixed-point $x^* = g(x^*, \mu)$ is mapped onto a point $x_2 = x^* + \delta x_2$ as

$$x^* + \delta x_2 = g(x^* + \delta x_1, \mu) \simeq x^* + \left\{ \frac{\partial g}{\partial x}(x^*, \mu) \right\} \delta x_1. \tag{6}$$

Near the true fixed point, successive iterations map to alternate sides of the true fixed point ($\delta x_1 \delta x_2 < 0$), but the distance from the fixed point doesn't continue to grow, if the following condition is satisfied.

$$||\delta x_1| - |\delta x_2|| < \Delta/2, \tag{7}$$

where Δ is the quantization step and we suppose that the quantization error of the mapping is due to rounding. This condition gives an estimate for a domain of points which are trapped near the fixed point as

$$|\delta x_1| < \frac{\Delta/2}{\left|1 - \left|\frac{\partial g}{\partial x}(x^*, \mu)\right|\right|}. \tag{8}$$

The dashed line in figure 3(b) shows the boundary of the domain specified by inequality (8). Points trapped in the domain are not necessarily fixed points. However, the system can appear to be stable in the domain, because the width of the domain

is much smaller than the dynamic range of the map. We call this domain near the fixed point where inequality (8) is satisfied the "quasi-stable" region.

Next, we take a residual error r of order $n_{t_m}\Delta$ in the digital filter into account [5]. With the filter and delay included, and assuming the delay time is much longer than the relaxation time of the filter, the fixed point of the loop dynamics is given by

$$x^* = g(x^*, \mu) + r. \tag{9}$$

This leads to the following inequality, corresponding to inequality (8),

$$|\delta x_1| < \frac{\Delta/2 + |r|}{\left|1 - \left|\frac{\partial g}{\partial x}(x^*, \mu)\right|\right|}. \tag{10}$$

We can simply estimate the expected shift of the point of onset of oscillation due to quantization effects under the condition of $T_\mu \gg n_{t_r}T \gg n_{t_m}T$, where T_μ and T are the time interval for varying μ and the period of the clock signal driving the 16-bit data in the loop, respectively.

Assume the system is in a stationary state $x_i^* = g(x_i^*, \mu_i)$ and μ is then increased from μ_i to $\mu = \mu_i + \Delta\mu$. A step signal Δx is generated as $\Delta x = g(x_i^*, \mu_i + \Delta\mu) - g(x_i^*, \mu_i) \simeq \left\{\frac{\partial g}{\partial \mu}(x_i^*, \mu_i)\right\}\Delta\mu$. If the increment $\Delta\mu$ is so small that the value of x after μ increased, $x = x_i + \Delta x$, remains within the quasi-stable region at $\mu = \mu_i + \Delta\mu$, oscillation will not grow. This condition, $|\Delta x| < 2|\delta x|$, gives the following relation between $\Delta\mu$ and μ_i as

$$\Delta\mu < \frac{\Delta + 2|r|}{\left|1 - \left|\frac{\partial g}{\partial x}(x_i^*, \mu_i)\right|\right|} \left\{\frac{\partial g}{\partial \mu}(x_i^*, \mu_i)\right\}^{-1}, \tag{11}$$

with the approximation that $\delta x \sim \delta x_i$, where δx_i is the half width of the quasi-stable region at μ_i.

According to inequality (11), if μ is increased in small increments $\Delta\mu$, the onset of oscillation will not occur at the true bifurcation point, but rather will occur at a larger value of μ. On the other hand, if the system is initially in a large amplitude oscillation state (i.e., outside the quasi-stable region) at a parameter value μ above the true bifurcation point, and parameter μ is decreased, the system bifurcates back at the true bifurcation point. Thus, quantization-induced hysteresis is expected to be seen in the dependence of state on the parameter μ. The above discussion can be extended to apply to every bifurcation point.

5 Oscillation phenomena

In the experiment, we set $n_{t_r} = 400$ to fix the effective delay at $n_{t_r}/n_{t_m} = 40$, and compare the reproduced dynamics in the system with the results of Ikeda *et al.* [6]. We drove the system by a clock signal of period $T = 20\mu$sec ($\equiv$50kHz), and observed the D/A-converted signal in real time. The value of μ was set from port (d) in figure 1 by PC with the 16-bit integer data U ranging from 0 to 65535, where μ related to U as $\mu = U/65536$. U was increased or decreased in increments of $\Delta U = 100$ ($\Delta\mu \approx 1.53 \times 10^{-3}$). The time between increments of U was about 50 msec, much larger than the round-trip delay time $n_{t_r}T$=8msec and the response-time $n_{t_m}T$=0.2msec.

First we implemented the IIR digital filter of type (I). Figure 4 shows examples of the oscillations generated in the system. Figure 5 shows the schematic diagram of the oscillation mode transitions. Except for the quantization-induced hysteresis of bifurcation points, the dynamics generated in the system were consistent with those obtained by Ikeda *et al.*[6]. The extent of the quantization-induced hysteresis was consistent with the simple rough analysis at the previous section. In figure 5, the points where the bifurcations and the transitions occurred are indicated by upward triangles for increasing μ and downward triangles for decreasing μ. The smaller the increment $\Delta\mu$, the larger the hysteresis. In the case of the IIR digital filter of type (II), similar results were obtained, except for the widths of the spurious hysteresis.

Figure 6 illustrates the relation between the increasing parameter step size ΔU ($\equiv \Delta\mu$) and the value of parameter U ($\equiv \mu_i$) where bifurcation (oscillation) occurs, according to inequality (11). Dispersion of the experimental results is due to the dispersion of the initial states of the system in multiple trials. Larger dispersion of the experimental result of the IIR digital filter of type (I) is expected to result from the larger dispersion of r value due to its somewhat more complex filter structure.

6 Conclusion

We constructed a digital nonlinear delayed-feedback system which reproduces complicated nonlinear dynamics in real time. With the digital implementation, it is possible to design the degree of complexity of reproduced dynamics. We established guidelines to determine the architecture and scale of the system, appropriate to

reproduce the nonlinear dynamics required.

In a simulation of the oscillation phenomena of a nonlinear ring cavity model[6], we confirmed that bifurcations up to order m=3 can be distinguished as designed and the behavior of oscillation modes is consistent with that of the original model, except for the quantization-induced hysteresis of bifurcation points. The theoretical estimation of the hysteresis was in good agreement with the experimental results.

In the parameter range for chaotic regime, we observed features peculiar to chaos, randomness in waveform, dense orbits in phase portrait, continuous spectrum and intermittent mode transitions. A rigorous study of the degree of fidelity of the chaotic oscillations is a topic for further future study.

The implementation of nonlinear delayed-feedback models in electronic devices is of interest from the point of view of applications in complex signal generation, ranging from electronic music [2] to dynamical memory [7]. Digital devices can have advantageous over analog devices [8][9] due to the flexibility in changing parameters and the stability of operation. The simple architecture of the system proposed here makes it suitable for implementation as an IC chip which utilizes complicated dynamics.

References

[1] K.Ikeda and H.Daido, "Optical turbulence : Chaotic behavior of light from a ring cavity," Phys. Rev. Lett. vol.45, pp.709-712, Sept. 1980.

[2] M.E.Mclntyre, R.T.Schumacher and J.Woodhouse "On the oscillations of musical instruments," J. Acoust. Soc. Am. vol.74 (5), pp.1325-1344, Nov. 1983.

[3] T.Aida and P.Davis, "Oscillation modes of laser diode pumped hybrid bistable system with large delay and application to dynamical memory," IEEE J. Quantum Electron., vol.28, pp.686-699, Mar. 1992.

[4] R. Vallée and C. Delisle, "Noise versus chaos in acousto-optic bistability," Phys. Rev. A ,vol.30, pp.336-342, Jul. 1984.

[5] A.V.Oppenheim and R.W.Schafer, Digital signal processing, New Jersey, Prentice-Hall, Inc., 1975.

[6] K.Ikeda and K.Kondo, "Successive higher-harmonic bifurcations in systems with delayed feedback," Phys. Rev. Lett. vol.49, pp.1467-1470, Nov. 1982.

[7] T.Aida and P.Davis, "Storage of optical pulse data sequences in loop memory using multistable oscillations," Elec. Lett., vol.27, pp.1544-1546, Aug. 15 1991.

[8] A.Rodriguez-Vazquez, J.L.Huertas, A.Rueda, B.Perez-Verdu and L.O.Chua, "Chaos from switched capacitor circuits: Discrete maps," Proc. IEEE, vol.75, pp.1090-1106, Aug. 1987.

[9] T.Yamakawa, T.Miki and E.Uchino, "A chaos chip for analyzing nonlinear discrete dynamical network systems," Proc. of Intern. Conf. on Fuzzy Logic and Neural Networks, Iizuka, Japan, pp.563-566, Jul. 1992.

Figure 1: Block diagram of the digital delayed-feedback system and experimental setup. The nonlinear function f is implemented in a lookup memory table. The lookup memory table has a configuration of 2^{16} words $\times$ 16 bits (1 word $\equiv$ 16 bits). The gain μ is realized using a 16-bit $\times$ 16-bit parallel multiplier (Analog Devices ADSP-1016AJN). The impulse-response $h_D(n)$ is implemented in a digital signal processor (Texas Instruments TMS320C25). The variable delay-line is realized using digital memory with a configuration of 2047 steps $\times$ 16 bits. A delay-step number n_{t_r} ranging from 6 to 2053 is obtained with the delay-line and the dead delay in each circuit block. These blocks and an extra block inserted for testing and observing are connected in a loop with 16-bit data-bus. A personal computer (PC) is connected to the blocks through a common control-bus for online control of parameters.

Figure 2: Implementation of nonlinear function f and impulse response h_D.
(a) Data for the nonlinear function f written in the memory table. $F(A) = \text{nint}\left[\frac{65535}{2}\left\{1-\sin(2\pi\frac{A}{65536})\right\}\right]$, where nint$[x]$ means the rounding of x. A and F take 16-bit SB integer numbers, respectively corresponding to the 16-bit address of the memory table and the data stored there.
(b) Block diagrams of IIR digital filters realizing the relaxation characteristic of equation (3). Filter coefficients are calculated for response-step number $n_{t_m} = 10$. (type I) IIR filter, designed by bilinear transformation, with the impulse response, $h_D(n) = b_0 a_1^n u(n) + b_1 a_1^{n-1} u(n-1)$, where $u(n) = 1$ for $n \geq 0$ and $u(n) = 0$ for $n < 0$. The coefficients are $a_1 = (2n_{t_m} - 1)/(2n_{t_m} + 1)|_{n_{t_m}=10} \approx 0.904755$, $b_0 = b_1 = 1/(2n_{t_m} + 1)$, $c_0 = 1/c_1 = 2/(2n_{t_m} + 1)|_{n_{t_m}=10} \approx 0.095245$ and $c_1 b_0 = c_1 b_1 = 0.5$. (type II) IIR filter, designed by approximating the derivative with the backward difference, with impulse response, $h_D(n) = ba^n u(n)$. The coefficients are $a = n_{t_m}/(1+n_{t_m})|_{n_{t_m}=10} \approx 0.90909$ and $b = 1/(1+n_{t_m})|_{n_{t_m}=10} \approx 0.09091$.

Figure 3: (a) Bifurcation diagram of quantized map of $x_{n+1} = g(x_n, \mu)$, $g(x, \mu) = \mu f(x) = \frac{\mu}{2}\{1 - \sin(2\pi x)\}$. Variable x and function g take 65536 (2^{16}) quantized values. (b) Bifurcation diagram of the quantized map magnified around the first bifurcation point, where $\mu = U/65536$ and $x = X/65536$. The dashed line is the boundary of the quasi-stable region obtained from inequality (8).

Figure 4: Waveforms generated by the digital system and corresponding phase space trajectories, when implementing the model of equations (2)(3) and (4). These were drawn with the 16-bit digital data obtained from port (b) in figure 1. Each of these shows (n, m) mode = (a) (1,1) at $\mu = 0.534$, (b) (1,3) at $\mu = 0.691$, (c) (7,3) just above m=2 at $\mu = 0.763$, and (d) chaos at $\mu = 0.916$, respectively. (Oscillation modes are classified by harmonic number n and bifurcation order m.)

Figure 5: Schematic diagram of the oscillation mode transitions. (1,1), (1,2), (2,1), $\cdots$ denote oscillation mode classified by harmonic number n and bifurcation order m as (n, m). (n,C) denotes chaotic oscillation at n-th harmonic branch. Upward and downward triangles indicate bifurcation points for increasing μ and for decreasing μ, respectively. (The name of vertical axis n indicates harmonic number.)

Figure 6: Relation between the increasing parameter step size ΔU ($\equiv \Delta\mu$) and the value of parameter U ($\equiv \mu_i$) where bifurcation (oscillation) occurs. Here $n_{t_m} = 10$ and $n_{t_r} = 400$. Curves calculated from inequality (11) with $r = 5\Delta, 2.5\Delta$ and 0 indicate the predicted upper limits of the shift of the first bifurcation points, where $\Delta = 2^{-16}$. Thick bars and thin bars indicate experimental results for the IIR filters of types (I) and (II), respectively. The value of r for the IIR filters is estimated as $r \approx 5\Delta$.

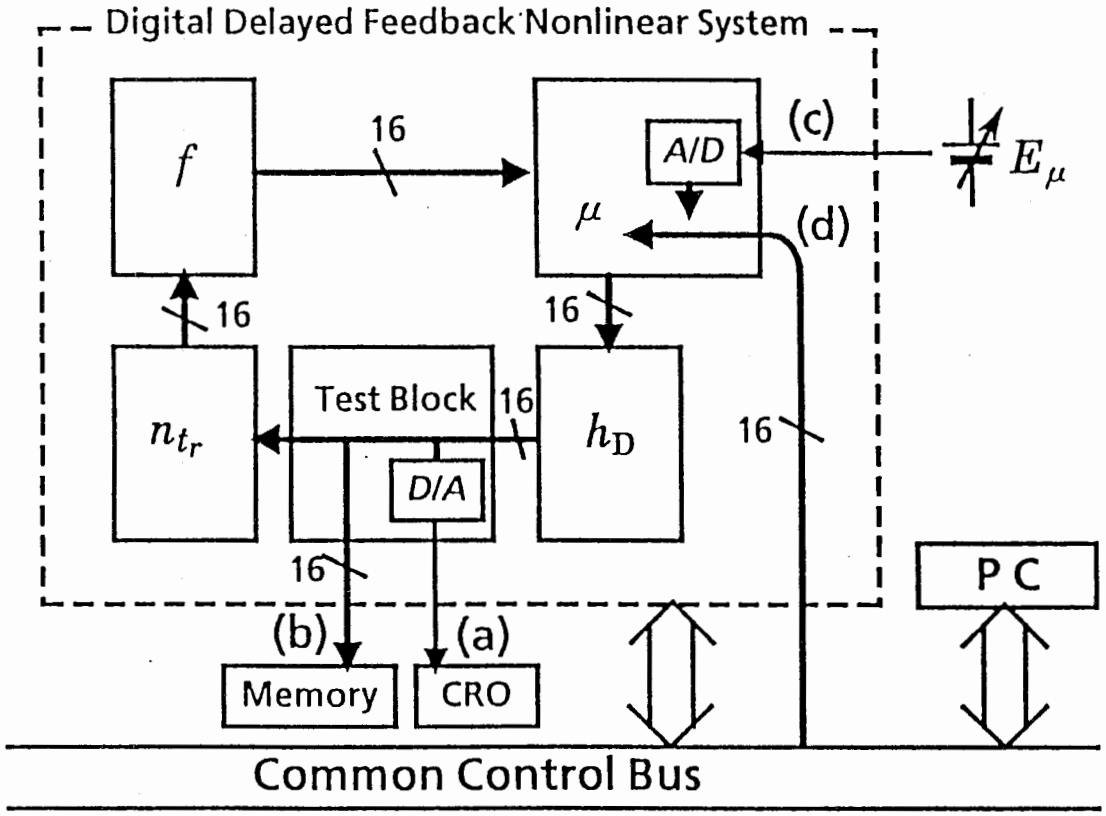

Figure 1: Block diagram of the digital delayed-feedback system and experimental setup. The nonlinear function f is implemented in a lookup memory table. The lookup memory table has a configuration of 2^{16} words $\times$ 16 bits (1 word $\equiv$ 16 bits). The gain μ is realized using a 16-bit $\times$ 16-bit parallel multiplier (Analog Devices ADSP-1016AJN). The impulse-response $h_D(n)$ is implemented in a digital signal processor (Texas Instruments TMS320C25). The variable delay-line is realized using digital memory with a configuration of 2047 steps $\times$ 16 bits. A delay-step number n_{t_r} ranging from 6 to 2053 is obtained with the delay-line and the dead delay in each circuit block. These blocks and an extra block inserted for testing and observing are connected in a loop with 16-bit data-bus. A personal computer (PC) is connected to the blocks through a common control-bus for online control of parameters.

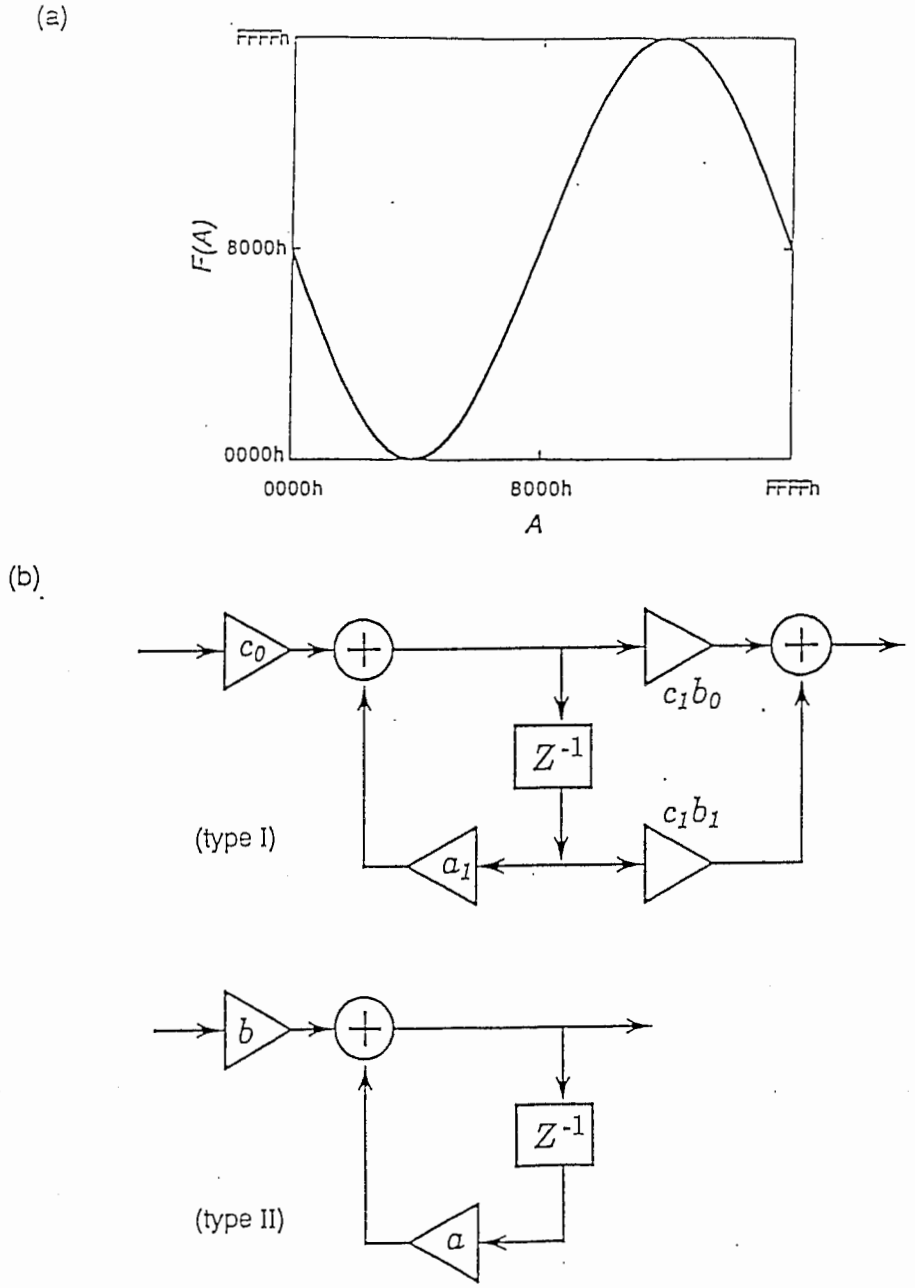

Figure 2: Implementation of nonlinear function f and impulse response h_D.
(a) Data for the nonlinear function f written in the memory table. $F(A) = \text{nint}\left[\frac{65535}{2}\left\{1-\sin(2\pi\frac{A}{65536})\right\}\right]$, where nint$[x]$ means the rounding of x. A and F take 16-bit SB integer numbers, respectively corresponding to the 16-bit address of the memory table and the data stored there.
(b) Block diagrams of IIR digital filters realizing the relaxation characteristic of equation (3). Filter coefficients are calculated for response-step number $n_{t_m} = 10$. (type I) IIR filter, designed by bilinear transformation, with the impulse response, $h_D(n) = b_0 a_1^n u(n) + b_1 a_1^{n-1} u(n-1)$, where $u(n) = 1$ for $n \geq 0$ and $u(n) = 0$ for $n < 0$. The coefficients are $a_1 = (2n_{t_m} - 1)/(2n_{t_m} + 1)|_{n_{t_m}=10} \approx 0.904755$, $b_0 = b_1 = 1/(2n_{t_m} + 1)$, $c_0 = 1/c_1 = 2/(2n_{t_m} + 1)|_{n_{t_m}=10} \approx 0.095245$ and $c_1 b_0 = c_1 b_1 = 0.5$. (type II) IIR filter, designed by approximating the derivative with the backward difference, with impulse response, $h_D(n) = ba^n u(n)$. The coefficients are $a = n_{t_m}/(1 + n_{t_m})|_{n_{t_m}=10} \approx 0.90909$ and $b = 1/(1 + n_{t_m})|_{n_{t_m}=10} \approx 0.09091$.

(a)

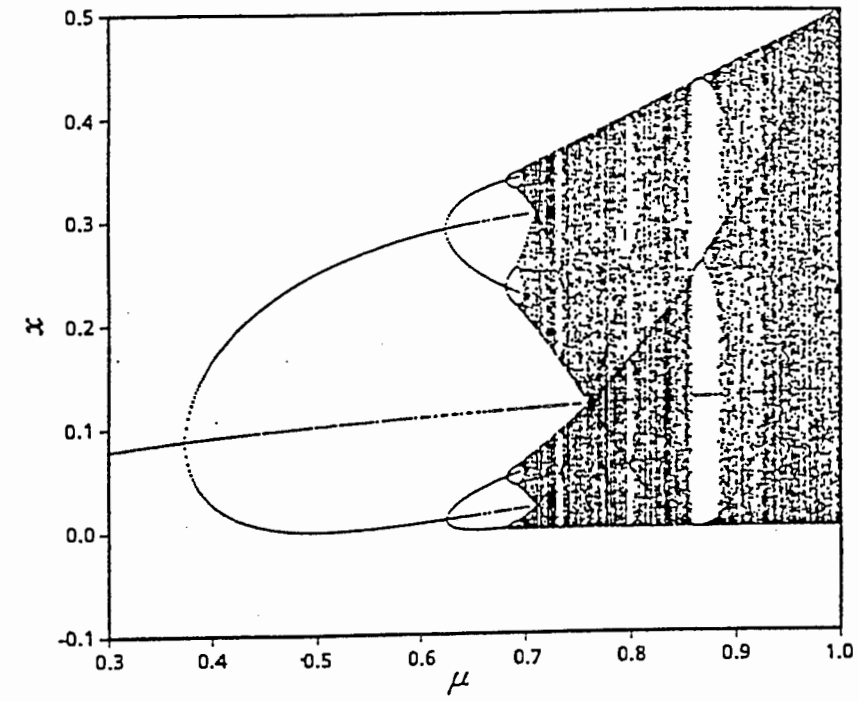

(b)

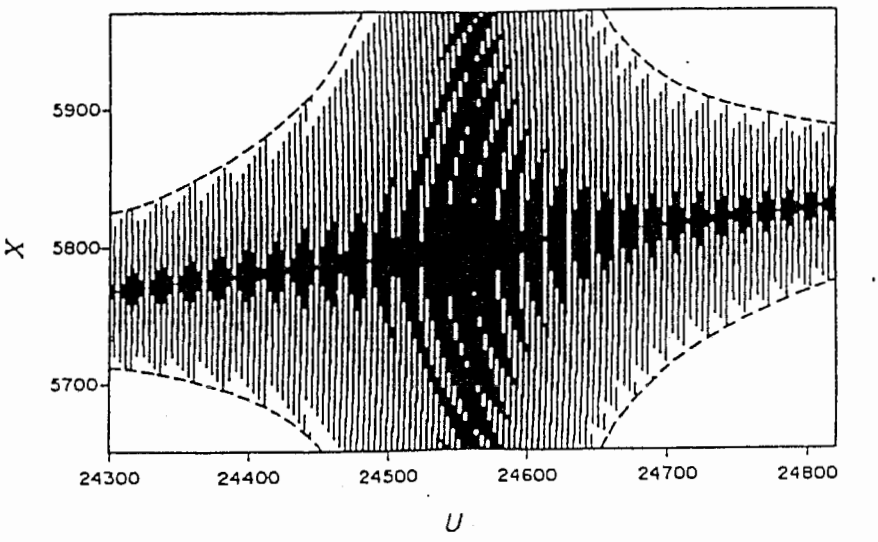

Figure 3: (a) Bifurcation diagram of quantized map of $x_{n+1} = g(x_n, \mu)$, $g(x, \mu) = \mu f(x) = \frac{\mu}{2}\{1 - \sin(2\pi x)\}$. Variable x and function g take 65536 (2^{16}) quantized values. (b) Bifurcation diagram of the quantized map magnified around the first bifurcation point, where $\mu = U/65536$ and $x = X/65536$. The dashed line is the boundary of the quasi-stable region obtained from inequality (8).

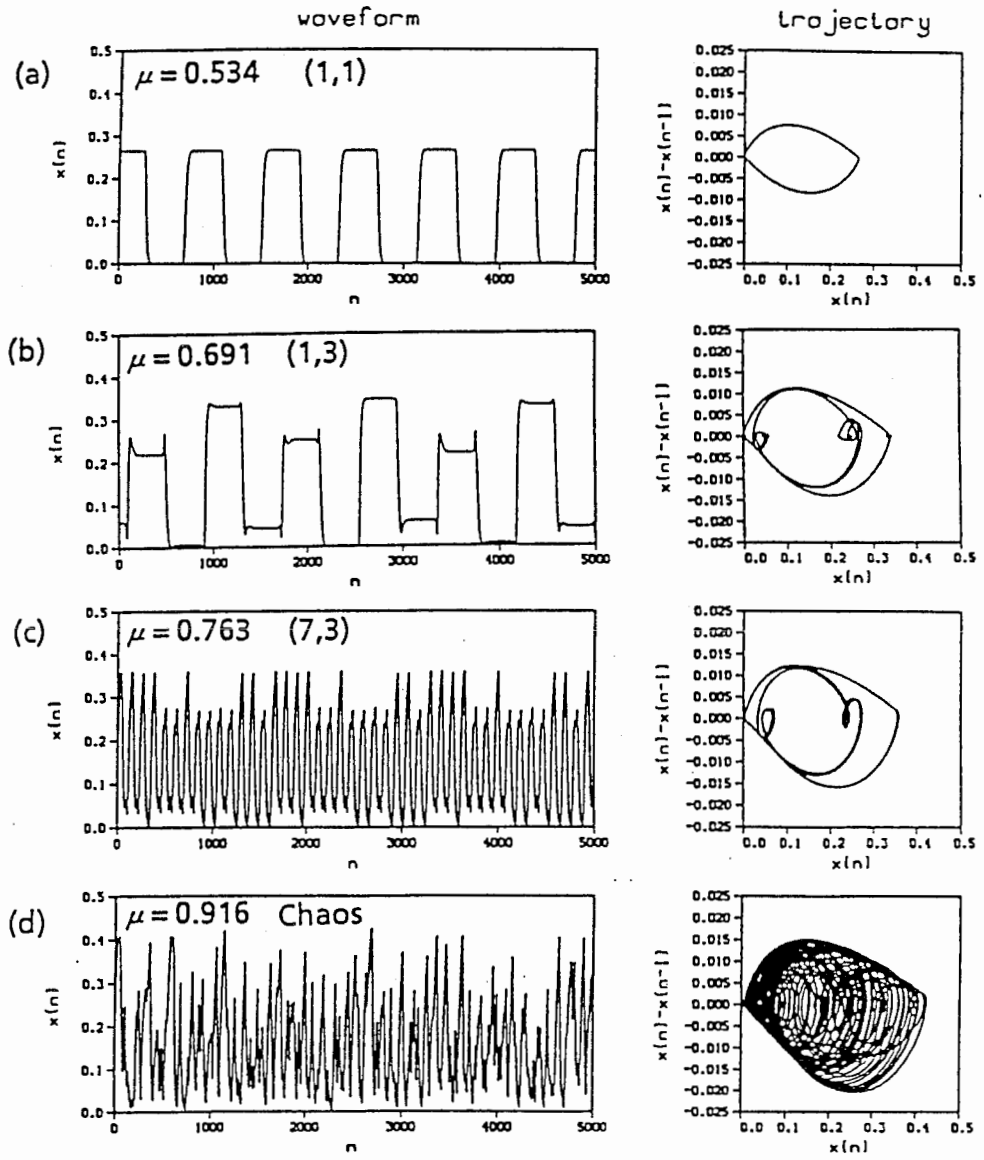

Figure 4: Waveforms generated by the digital system and corresponding phase space trajectories, when implementing the model of equations (2)(3) and (4). These were drawn with the 16-bit digital data obtained from port (b) in figure 1. Each of these shows (n, m) mode = (a) (1,1) at $\mu = 0.534$, (b) (1,3) at $\mu = 0.691$, (c) (7,3) just above m=2 at $\mu = 0.763$, and (d) chaos at $\mu = 0.916$, respectively. (Oscillation modes are classified by harmonic number n and bifurcation order m.)

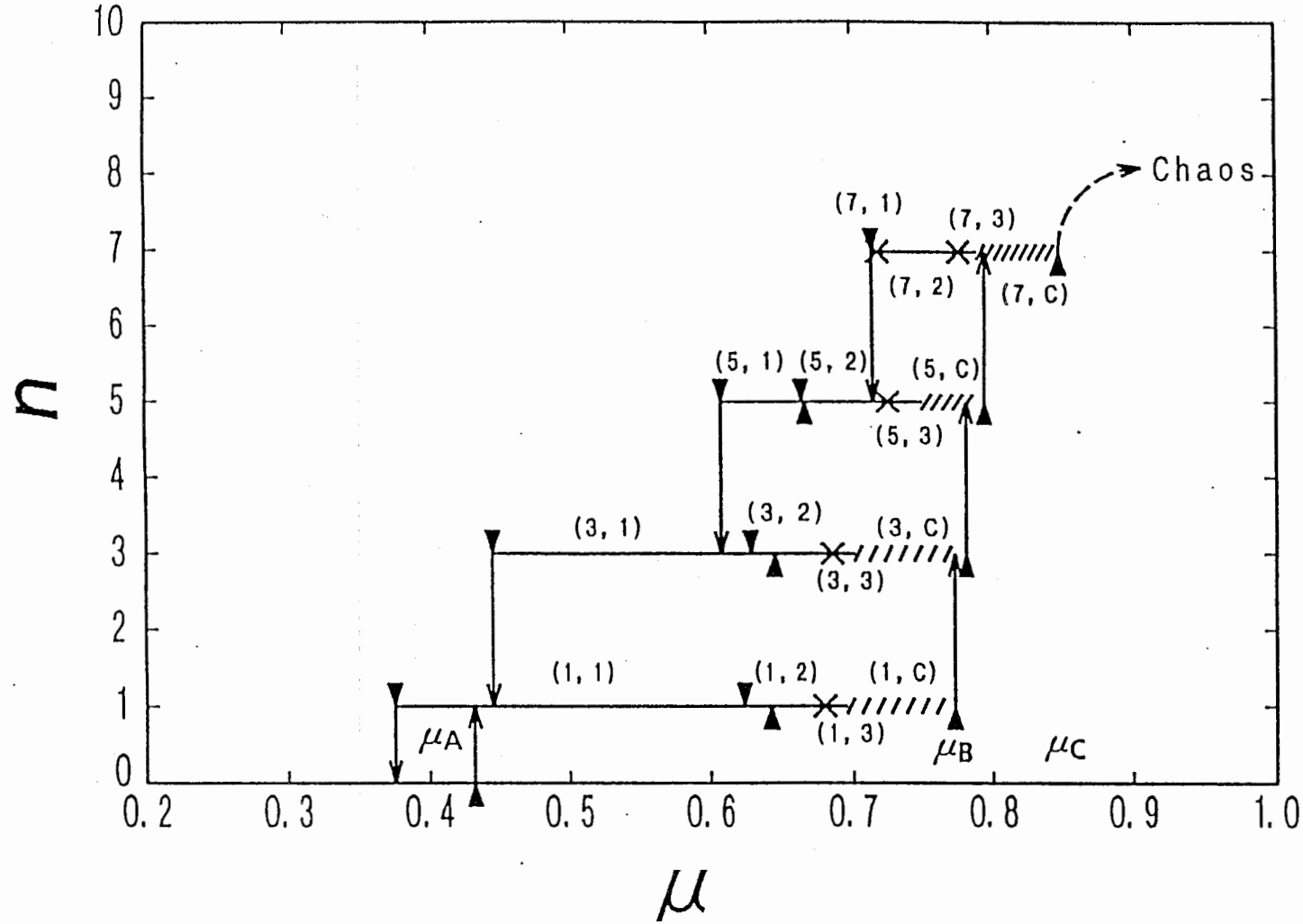

Figure 5: Schematic diagram of the oscillation mode transitions. (1,1), (1,2), (2,1), $\cdots$ denote oscillation mode classified by harmonic number n and bifurcation order m as (n, m). $(n$,C) denotes chaotic oscillation at n-th harmonic branch. Upward and downward triangles indicate bifurcation points for increasing μ and for decreasing μ, respectively. (The name of vertical axis n indicates harmonic number.)

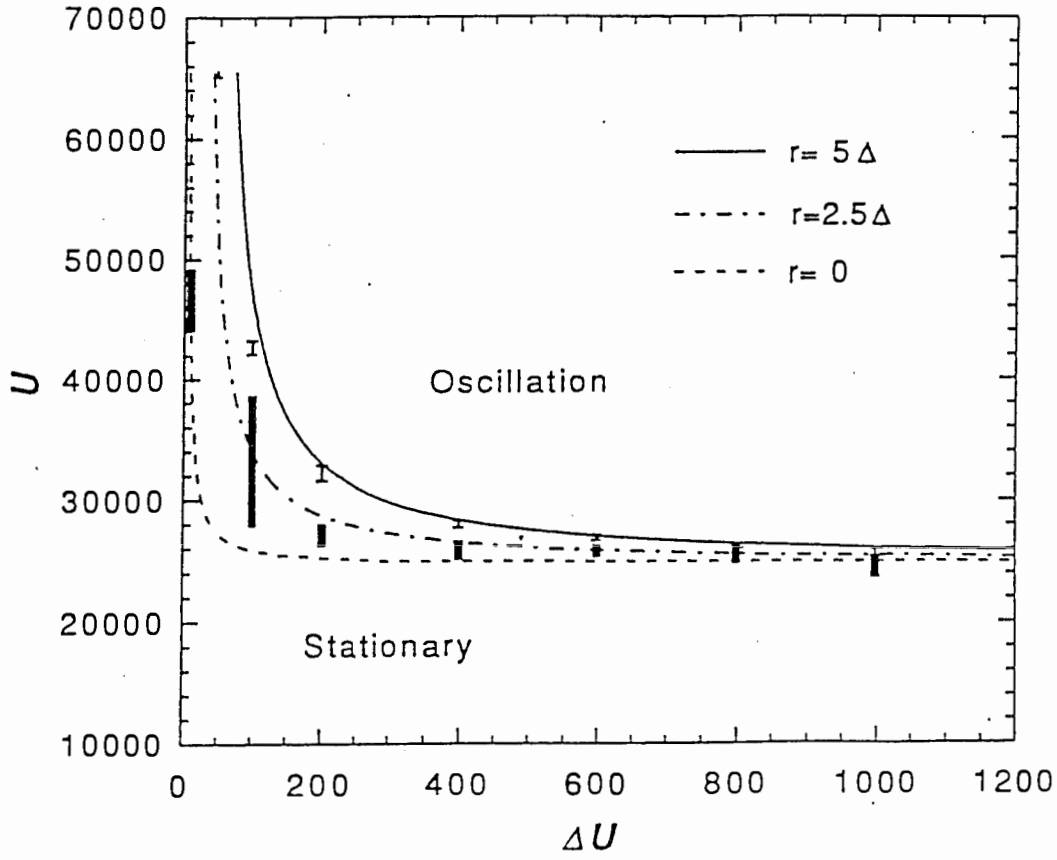

Figure 6: Relation between the increasing parameter step size ΔU ($\equiv \Delta\mu$) and the value of parameter U ($\equiv \mu_i$) where bifurcation (oscillation) occurs. Here $n_{t_m} = 10$ and $n_{t_r} = 400$. Curves calculated from inequality (11) with $r = 5\Delta, 2.5\Delta$ and 0 indicate the predicted upper limits of the shift of the first bifurcation points, where $\Delta = 2^{-16}$. Thick bars and thin bars indicate experimental results for the IIR filters of types (I) and (II), respectively. The value of r for the IIR filters is estimated as $r \approx 5\Delta$.

Acknowledgments

The author expresses appreciation to ex-president Dr. Yoji Furuhama of ATR Optical and Radio Communications Research Laboratories, Drs. Isao Fujimoto and Kikuo Kobayashi of NHK (Japan Broadcasting Corporation) and Mr. Toshihide Watanabe of ATR for encouragement and support.

The author wishes to thank Prof. Kensuke Ikeda and Drs. Shigetoshi Nara, Masakatsu Okada and Kuniharu Takizawa for their helpful suggestions and discussions.

This work is based mainly on the idea of Peter Davis. The auther acknowlegdes Dr. Peter Davis for useful advice and discussions.